Bispectrum and Bicorrelation: a higher order stochastic approach to non-Gaussian Dynamic Wind Loading

University of Liège - Faculty of Applied Sciences

Master's Degree in Civil Engineering

Author:
Michele ESPOSITO MARZINO
s189058

Advisor:
DENOËL, Vincent

Jury:
ANDRIANNE, Thomas
DE MIRANDA, Stefano
DE VILLE DE GOYET, Vincent

Academic Year 2018-2019

"Prendete la vita con leggerezza, che leggerezza non è superficialità, ma planare sulle cose dall'alto, non avere macigni sul cuore."

Italo Calvino

Contents

List of Figures

Abstract

The main objective of this Thesis is to provide a more efficient as precise alternative to classic dynamic analysis. Conventionally, it is performed by means of Fourier Analysis, in which time series of the loading are analysed, then brought into the frequency domain (by Fourier Transform), applied to the specific structure (characterised by its Transfer Function, which depend on structural parameters only) to get response in the frequency domain, then Inverse Fourier Transform is applied to recover response in time domain.

As it can be clearly understood, this process becomes very heavy when dealing with (real) structures having many degrees of freedom - because this double transformation has to be done for each degree of freedom to be able to reconstruct the entire structural response (supposing to perform analysis in the Modal Base, which is almost always the case since with nowadays F.E.M. software, recovering the Modal Matrix is no more time consuming as it could have been some years ago).

Therefore, specially for the pre-design stages of a civil engineering project, an alternative method, faster as well as reliable, able to compute or characterise structural response is needed. In this framework, this Thesis takes its place.

It will be shown and proved, as in other previous works, an alternative dynamic analysis method based on the Background and Resonant responses, under the assumption of stationary Gaussian loading. It is basically based on the decomposition of the response in its two major components, which are by their own computed based on main statistical quantities of the loading (mean value and Power Spectral Density Function or, equally, variance). This way, the previous Double time-frequency transformation is avoided: once loading is known (i.e. measured or simulated), response can be reconstructed by statistical analysis.

However, this decomposition is no more valid when the loading has non-Gaussian distribution. Therefore, the aim of this Thesis is to finally validate an extension of the previous approach to more general cases in which loading is non-Gaussian. Still, the response will be decomposed in its Background and Bi-resonant components in the frequency space, where they will be connected to higher order statistical quantities of the loading.

1 Introduction

1.1 Introduction to wind loading

Wind loading has always played an important role in Structural Analysis. However, since the last decades, it has acquired much more importance after the occurrence of many wind damaging events (ex. Collapse of Tacoma Narrow Bridge, 1938), especially when it comes to structures in which one dimension in much more predominant to the other two (i.e. flexible structures, such as slender structures, suspended-span bridges). Therefore, the field of wind loading on structures has had significant research effort and important scientific literature has been progressively built up.

The design of buildings and structures for wind depends upon:

- Wind environment;
- Aerodynamic effects induced in the structural system by the wind environment;
- Response of structural system;
- Eventually, some safety requirements based on uncertainty analyses and expressed in 'wind load factors' or 'design mean recurrence intervals' of the response.

For structural design purposes, wind environment must be described in terms of:

- Meteorological terms;
- Micro-meteorological terms (i.e., dependence of wind speeds upon averaging time, dependence of wind speeds and turbulent flow fluctuations on surface roughness and height above the surface);
- Extreme wind climatological terms (directional extreme wind speed data at structure's site, probabilistic modelling based on such data).

The description of the wind flow's micro-meteorological features is needed for three main reasons:

(i) They directly affect structure's aerodynamic and dynamic response (e.g., wind speeds increasing with height above the surface means that wind loads are larger at higher elevations than near the ground);

(ii) Turbulent flow fluctuations strongly influence aerodynamic pressures, and produce in flexible structures fluctuating motions that may be amplified by resonance effects;

(iii) Micro-meteorological considerations are required to transform measured or simulated wind speed data at meteorological stations or other reference sites into wind speeds data at the site of interest.

However, micro-meteorological features are explicitly considered in structural analysis if wind pressures or forces acting on the structure are determined by formulas specified by codes for example. However, for design based on wind-tunnel testing (as in This Paper), this is no longer the case. Rather, it is made use of records of non-dimensional aerodynamic pressure data.

To perform a design based on aerodynamic data obtained in wind-tunnel tests, structural engineer needs these three products:

1. Time series of pressure at large number of taps (also called "monitors"), adimensionalised with respect to the wind tunnel mean wind speed at the reference height (commonly, the elevation of the building roof);
2. Matrices of directional mean wind speeds at the site of interest, at the prototype reference height;
3. Estimates of uncertainties in items (1) and (2).

1.2 Wind Nature

Wind, or more correctly the 'motion of air with respect to the surface of the Earth', is fundamentally caused by variable solar heating of the Earth's atmosphere.

It is initiated by differences of pressure between points of equal elevation. The energy required for the occurrence of these phenomena is provided by the sun in the form of radiated heat. More specifically, atmosphere is to a large extent transparent to the solar radiation incident upon the Earth; that portion of the solar radiation that is not reflected or scattered back into space may be therefore assumed to be absorbed entirely by Earth. The Earth, upon being heated, will emit energy in the form of terrestrial radiation (characterised by long wavelengths, order of 10 μ); the atmosphere, which is largely transparent to solar but not to terrestrial radiation, absorbs the heat radiated by the Earth and re-emits some of it toward the ground.

The air motion is determined by different forces:

- The *horizontal pressure gradient force* per unit of mass, due to spatial variation of horizontal pressures. This force is normal to the lines of constant pressure (isobars); it is directed from high-pressure to low-pressure regions;

$$Pressure\ gradient\ force\ per\ unit\ of\ mass = \frac{1}{\rho} * \frac{\partial p}{\partial n} \tag{1.1}$$

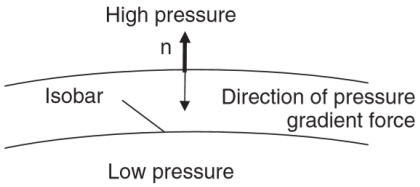

Figure 1.1: Pressure gradient force per unit of mass, see [2].

- The *deviating force due to the Earth's rotation*, also know as *Coriolis Force* or "apparent" force:

$$Coriolis\ Force,\ F_c = mfv$$

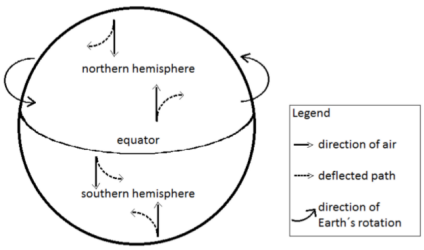

Figure 1.2: Coriolis Force, see [2] .

- The *friction force* that the surface of the Earth exerts on the moving air. It decreases with elevation above the ground, as the imperviousness decreases. It becomes negligible above a height δ known as *gradient height*.
  The atmospheric layer between the Earth's surface and the gradient height is called the *atmospheric boundary layer*.
  The wind velocity speed at height δ is called the *gradient velocity*.
  The atmosphere above the gradient height is called *free atmosphere*.

  The main effect of the friction force is that of retarding the flow. This effect is diffused by turbulent mixing in the atmospheric boundary layer (ABL).

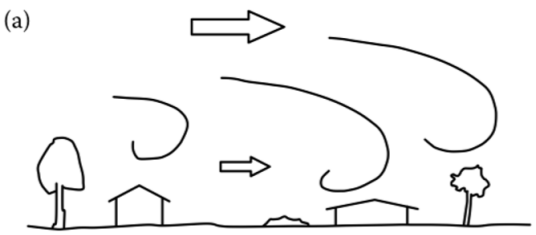

Figure 1.3: Friction force, see [7].

It has to be noted that within the ABL, the mean wind speed varies as a function of elevation.

Also, if flow were laminar, wind speeds would be the same for all the averaging times. However, due to turbulent fluctuations, the definition of wind speeds depends on averaging time.

For example, the *hourly wind speed* is the wind speed averaged over 1 hour. Different would be the *Ten-minute wind speeds*, which are wind speeds averaged over 10 min (used in World Meteorological Organization, WMO).

As it was already stated previously, wind speed varies with varying height above the Earth's surface. Basically, in almost all the case, two are the considered types of variation of mean or time-averaged wind speed:

- *Logarithmic Law*, expressed as

$$\frac{U(z)}{u_*} = \frac{1}{k} \ln \frac{z-d}{z_0} \tag{1.2}$$

  where
  $U(z) =$ mean wind velocity at height z [m] above the surface;
  $u_* =$ friction velocity $[m\ s^{-1}]$;
  $k =$ Von Karman constant (≈ 0.41);
  $z =$ height in meters above the gorund;
  $d =$ zero plane displacement $[m]$;
  $z_0 =$ terrain roughness $[m]$

- *Power Law* which is strictly empirical, expressed as

$$U(z) = U_r * (\frac{z}{z_r})^{\alpha} \tag{1.3}$$

  where
  $U(z) =$ mean wind velocity at height z $[m]$ above the surface;
  $U_r =$ known speed at reference height z_r;
  $z_r =$ reference height $[m]$;
  $\alpha =$ empirical exponent which depends on terrain roughness.

NOTE: for sake of clarity, in the Database which will be presented in the following, it has been used the Power-law wind profile.

Except for wind having very low velocities and under specific temperature conditions, in all other cases wind flow is not laminar (smooth); instead, it is *turbulent*. This means that it *fluctuates* in time and in space. In other words, wind speed is a random variable which depends on time and space independent variables.

Atmospheric flow turbulence characterisation is important for structural engineering applications for many reasons:

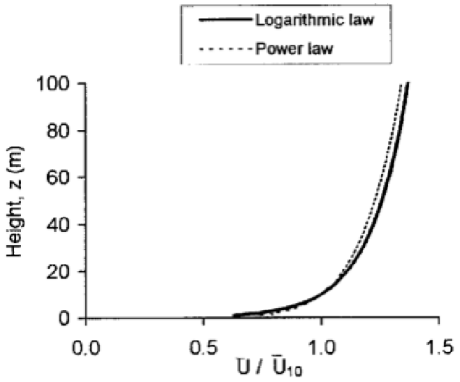

Figure 1.4: plot of both Logarithmic-law and Power-law, see [7].

- Turbulence affects definition of wind speed (which is one of the input data required in engineering computations);
- By transporting particles from flow regions with high momentum into low-speed regions, turbulence can influence significantly the wind flow around a structure and, therefore, the aerodynamic pressures acting on the structure;
- Last, but not least, turbulence produce resonant dynamic effects in flexible structures.

The *"longitudinal turbulence intensity"* at a point with elevation z is defined as:

$$I_u(z) = \frac{\overline{u^2(z,z_0)}^{\frac{1}{2}}}{U(z)} \tag{1.4}$$

where

$$\overline{u^2(z,z_0)}^{\frac{1}{2}} = \sqrt{\beta(z,z_0)} * u_* \tag{1.5}$$

is the r.m.s. of the longitudinal wind speed fluctuations $u(z,t)$, z_0 is the surface roughness,

$$\beta(z,z_0) = \beta(z_0) * \exp\left(-1.5 * \frac{z}{H}\right) \tag{1.6}$$

$\beta(z_0)$ tabulated, H is the ABL depth, u_* is the friction velocity, and finally $U(z)$ is the mean speed at elevation z above the ground.

par

Very roughly it could be said that, the previous three fundamental forces which characterise air movement (i.e. wind) will combine in different ways, generating infinite air flow configurations, for either large-scale circulations to local or exceptional events.

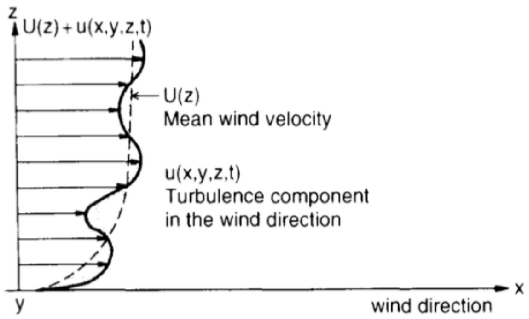

Figure 1.5: Wind speed profile: mean component along with turbulent component illustration, see [7].

Since it is not the scope of this Work, exceptional events will be not treated.

Is then clear that, for civil engineering applications, design wind speed is one of the most critical data needed to perform required analysis.

There are basically two methods to asses the design wind speed [7]:

- Probabilistic assessment, the so-called *"extreme value analysis"*, covered in detail by Gumbel (1954,1958). It consists in fitting historical data with known (or assumed) probability distribution function (Gumbel, ...). The output of a probabilistic assessment is a design wind speed corresponding to a given return period R (expressed in years). However, this method has led in the past to underestimations of mean wind speeds (e.g. Tracy cyclone in Australia);
- Parallel to this now "classical" approach, since last years in the wind engineering field it has significantly increased the availability, on the free Web, of data related to external shape factors and pressure coefficients on low-rise and high-rise buildings, obtained by means of Wind Tunnel Tests . In this context, a crucial role is played by:
  - The National Institute of Standards and Technology (NIST) of the United States which has provided data produced by the University of Western Ontario on 37 different configurations of low-rise gable roof buildings (no eaves);
  - The Wind Engineering Group of the Tokyo Polytechnic University which provides a database on:
    * 116 configuration of low-rise buildings with gable hipped and flat roofs, with or without eaves;
    * 22 configurations of high-rise buildings.

    This Database constitutes the very Source of the whole Work presented in This Document.

Figure 1.6: Example of ABL wind tunnel test.

2 Recall On Dynamics Theory of SDOF systems

In order to fully understand the content of this Document, it is important to have clear in mind the theory of Dynamics.

However, since it is not the major content of this work, it will not be covered extensively. Therefore, the reader is invited to clarify any possible doubts it may rise from literature, which is very wide on this subject.

That being said, we will start by exploiting the dynamic response of a SDOF system (Single Degree Of Freedom) In the following it will be shown how to extend the results to a general MDOF system (Multi Degree Of Freedom), which is the case for quite all civil structures.

2.1 Response to Harmonic Loading

General dynamic equation of a SDOF is given by

$$m\,\ddot{x}(t) + c\,\dot{x}(t) + x(t) = p(t) \tag{2.1}$$

When it comes to Harmonic Loading (assume it sinewave)

$$m\,\ddot{x}(t) + c\,\dot{x}(t) + x(t) = p_0\ \sin\overline{\omega}t \tag{2.2}$$

where $p_0 = amplitude, \overline{\omega} = circular\ frequency\ [\frac{rad}{s}]$.

Dividing everything by the mass m of the system, and considering the exponential form,

$$\ddot{x}(t) + 2\,\xi\,\omega\,\dot{x}(t) + \omega^2\,x(t) = \frac{p_0}{m}\ \exp\left(i\,\overline{\omega}\,t + \phi\right) \tag{2.3}$$

The complementary solution, which is the solution of the previous equation with right-hand side equal to 0 (which means, no load applied), is the well-known *damped free-vibration response* ([1])

$$x_{comp}(t) = \left[A\ \cos\left(\omega_D\,t\right) + B\ \sin\left(\omega_D\,t\right)\right]\ \exp(-\xi\,\omega\,t) \tag{2.4}$$

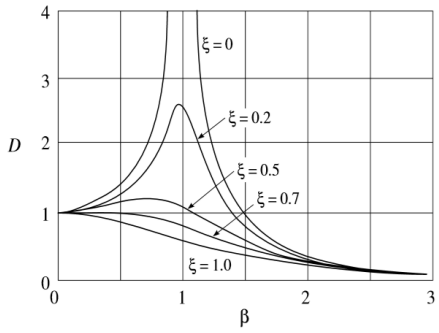

Figure 2.1: Variation of dynamic amplification factor with damping and frequency [1].

where A and B are constants to be defined considering initial conditions.

The particular solution is of the form

$$x_p(t) = \rho \, \sin(\overline{\omega} \, t - \theta) \tag{2.5}$$

where $\rho =$ amplitude

$$\rho = \frac{p_0}{k} \left[\frac{1}{\sqrt{(1-\beta^2)^2 + (2 \, \xi \, \beta)^2}} \right] = \frac{p_0}{k} \, D \tag{2.6}$$

$\theta =$ phase angle

$$\theta = \arctan \left(\frac{2 \, \xi \, \beta}{(1-\beta^2)} \right) \tag{2.7}$$

$D =$ dynamic amplification factor.

NOTE:

$$\beta \equiv \frac{\overline{\omega}}{\omega} \tag{2.8}$$

is the ratio between applied circular frequency and natural circular frequency (of the system).

The total response is finally given by the sum of the two components, the complementary and the particular one.

However, it must be underlined that, between the two components, the one of major interest is the particular solution (which is also called "steady-state harmonic response"), since the complementary solution (also called "transient response") damps out in accordance with $\exp(-\xi \, \omega \, t)$ [1].

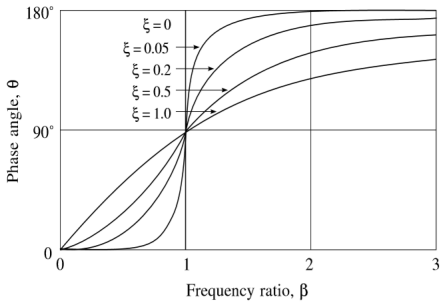

Figure 2.2: Variation of phase angle with damping and frequency [1].

Last but not least, a very important physical effect which needs to be taken into account when performing dynamic analysis is *resonance*. This is because of the intrinsic nature of the resonant effect: basically, it is a physical phenomena which significantly amplifies the amplitude of response, even if amplitude of loading is very low.

This happens when the natural circular frequency of the loading $\overline{\omega}$ becomes very close to the natural circular frequency of the structure ω, which means when the ratio

$$\beta = \frac{\overline{\omega}}{\omega} \rightarrow 1$$

tends to unity.

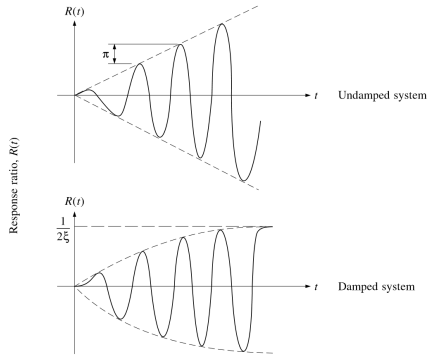

Figure 2.3: Response to resonant loading $\beta = 1$ for "at rest" initial conditions [1].

2.2 Response to Periodic Loading

Any periodic loading can be expressed as a series of harmonic loading terms ([4]). In exponential form it is expressed as

$$p(t) = \sum_{n=-\infty}^{\infty} \mathbf{P_n} \, \exp(i \, \omega_n \, t) \tag{2.9}$$

where $\mathbf{P_n}$ = complex amplitude coefficients

$$\mathbf{P_n} = \frac{1}{T} \int_0^T p(t)\ \exp(-i\,\overline{\omega}\,t)\,dt \qquad n = 0, \pm 1, \pm 2, ... \tag{2.10}$$

NOTE: from previous Eqs. 2.9 and 2.10, it can be noted that $\mathbf{P_n}$ and $\mathbf{P_{-n}}$ are complex conjugate pairs, necessary condition for the imaginary parts to cancel each other.

Therefore, the response of a linear system to this loading may be obtained by simply adding up the responses to the individual harmonic loading, which is exactly what has been presented in Section 2.1.

In the case loading is expressed in terms of individual harmonics of the exponential form, the nth harmonic steady-state response of the viscously damped SDOF system will be ([1])

$$x_n(t) = \mathbf{H_n}\,\mathbf{P_n}\ \exp(i\,\overline{\omega_n}\,t) \tag{2.11}$$

where $\mathbf{P_n}$ is given by Eq. 2.10 and

$$\mathbf{H_n} = \frac{1}{k}\ \left[\frac{1}{(1-\beta_n^2) + i\,(2\,\xi\,\beta_n)}\right] \tag{2.12}$$

is the *"complex frequency response coefficient"*.

2.3 Extension to Generic Loading

The approach is similar to the one mentioned in previous Section 2.2. Both involve expressing the applied loading in terms of harmonic components, and then superposing the harmonic responses to obtain total structural response.

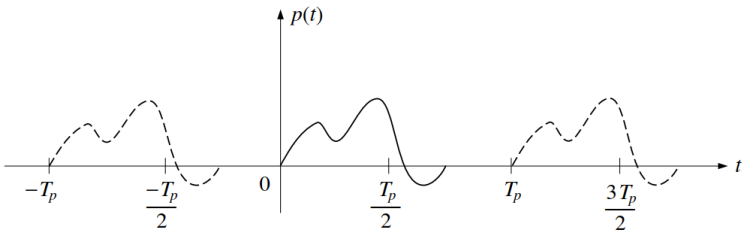

Figure 2.4: Example of a non-periodic loading [1].

The spurious repetitive dashed-line loadings could be eliminated by letting the period of the loading $T_p \rightarrow \infty$. Introducing the notations

$$\frac{1}{T_p} = \frac{\overline{\omega}_1}{2\,\pi} \equiv \frac{\Delta\overline{\omega}}{2\,\pi} \qquad n\overline{\omega}_1 = n\Delta\overline{\omega} \equiv \overline{\omega}_n \qquad \mathbf{P_n}\; T_p \equiv \mathbf{P}(i\overline{\omega}_n) \tag{2.13}$$

the previous Eqs 2.9 and 2.10 become

$$p(t) = \frac{\Delta\overline{\omega}}{2\,\pi} \sum_{n=-\,\infty}^{\infty} \mathbf{P}(i\overline{\omega}_n)\; \exp(i\overline{\omega}_n t) \tag{2.14}$$

$$\mathbf{P}(i\overline{\omega}_n) = \int_{-T_p/2}^{T_p/2} p(t)\; \exp(-i\overline{\omega}_n t)\; dt \tag{2.15}$$

However, if $T_p \;\rightarrow\; \infty$ the frequency increment becomes infinitesimal ($\Delta\overline{\omega} \rightarrow d\overline{\omega}$) and the discrete frequencies $\overline{\omega}_n$ become a continuous function of $\overline{\omega}$. Thus

$$p(t) = \frac{1}{2\,\pi} \int_{-\,\infty}^{\infty} \mathbf{P}(i\overline{\omega})\; \exp(i\overline{\omega}t) \tag{2.16}$$

$$\mathbf{P}(i\overline{\omega}) = \int_{-\infty}^{\infty} p(t)\; \exp(-i\overline{\omega}t)\; dt \tag{2.17}$$

also known as Inverse and Direct Fourier Transform respectively.

Hence, using the direct Fourier Transform, arbitrary loading $p(t)$ can be expressed as an infinite sum of harmonics having known complex amplitude ([1]). The function $\mathbf{P}(i\overline{\omega}$ represents the complex amplitude intensity at frequency $\overline{\omega}$ per unit of $\overline{\omega}$. Then, it is straightforward to notice that for general loading, in accordance to Section 2.2, total response is

$$v(t) = \frac{1}{2\,\pi} \int_{-\,\infty}^{\infty} \mathbf{H}(i\overline{\omega}\; \mathbf{P}(i\overline{\omega})\; \exp(i\overline{\omega}t)\; d\overline{\omega} \tag{2.18}$$

in which

$$\mathbf{H}(i\overline{\omega} = \frac{1}{k}\; \left[\frac{1}{(1-\beta^2) + i\;(2\;\xi\;\beta)}\right] \tag{2.19}$$

$\beta \equiv \frac{\overline{\omega}}{\omega}$.

3 Dynamic Wind Loading Analysis

As a reminder, the very first goal of This Work is that of constituting a very powerful Pre-design Tool to asses dynamic response of Tall Structures subjected to the dynamic action of Wind Loading.

3.1 Description of the Database: loading information

Everything is based on an Aerodynamic Database constructed by Tokyo Polytechnic University as on part of the Wind Effects on Buildings and Urban Environment the 21^{st} Century Centre of Excellence Program, funded by the Japanese Government [8]. In the following, it will be only done reference to the high-rise building part of the aforementioned Database.

Its object is to provide structural design engineers with wind tunnel test data of wind loads on high-rise buildings. These data can be used to calculate local wind pressures, area averaged wind pressure coefficients on wall surfaces, and even wind induced dynamic responses of high-rise buildings.

13 models of high-rise buildings have been tested (with a length scale of 1/400), 9 of which for two different exposure factors[1] ($\alpha = 1/4$ and $\alpha = 1/6$), for a total of 22 configurations.

	Model scale			Real scale		
Name	Breadth	Depth	Height	Breadth	Depth	Height
T111	0.1	0.1	0.1	40	40	40
T112	0.1	0.1	0.2	40	40	80
T113	0.1	0.1	0.3	40	40	120
T114	0.1	0.1	0.4	40	40	160
T115	0.1	0.1	0.5	40	40	200
T212	0.2	0.1	0.2	80	40	80
T213	0.2	0.1	0.3	80	40	120
T214	0.2	0.1	0.4	80	40	160
T215	0.2	0.1	0.5	80	40	200
T312	0.3	0.1	0.2	120	40	80
T313	0.3	0.1	0.3	120	40	120
T314	0.3	0.1	0.4	120	40	160
T315	0.3	0.1	0.5	120	40	200

Figure 3.1: 13 models. In yellow, the ones tested for both exposure factors.

Sample frequency f is given in the data, equal to

$$f_{sampling} = 1000\ Hz = 1\ kHz.$$

[1] In this Work, only samples with $\alpha = 1/4$ have been used.

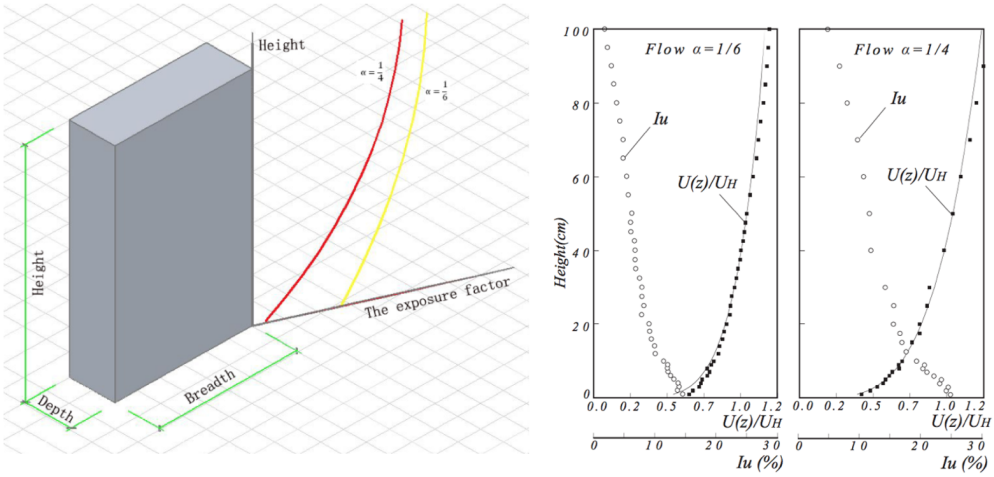

Figure 3.2: High-rise building configuration (left); wind speed profiles used (right). (source: www.wind.arch.t-kougei.ac.jp)

Also, the considered mean wind speed at the model reference height (40 cm) used to define the velocity profile is equal to

$$U_{ref} = 11.017 \frac{m}{s}$$

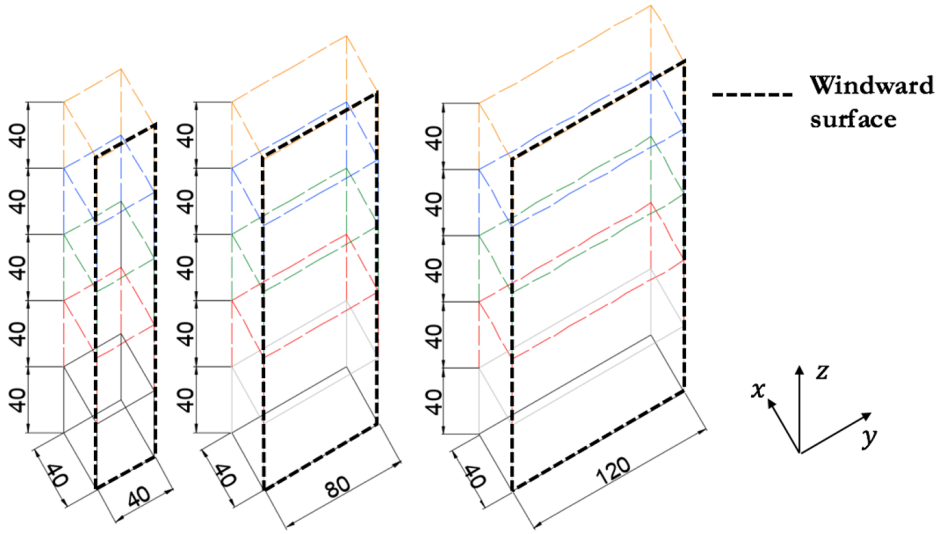

Figure 3.3: Illustration of different building samples.

NOTE: contrarily as shown in Figure 3.3, x and y axis are inverted! **y-axis is normal to Windward surface!**

After having inserted all the required parameters of the desired sample to be analysed, Figure 3.5 shows a sketch of the interface that appears.

From it, user can enter all the information and data available for the specified configuration selected.

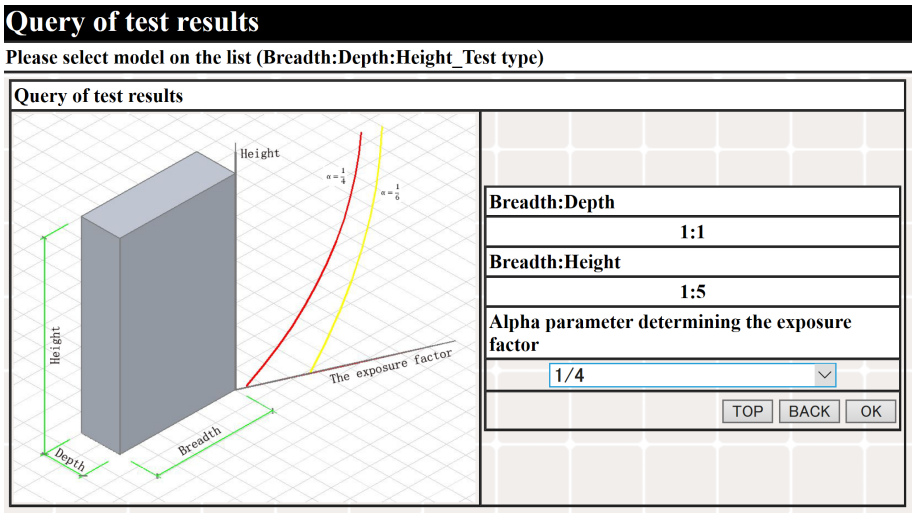

Figure 3.4: Window from which choosing desired sample data. (source: www.wind.arch.t-kougei.ac.jp)

The most important section, where all measurements are stored, is the bottom one. It can be noticed that, for a better understanding of the dynamic behaviour, each sample model has been tested for wind flows at different angle of attack between wind flow and normal to the Windward surface.

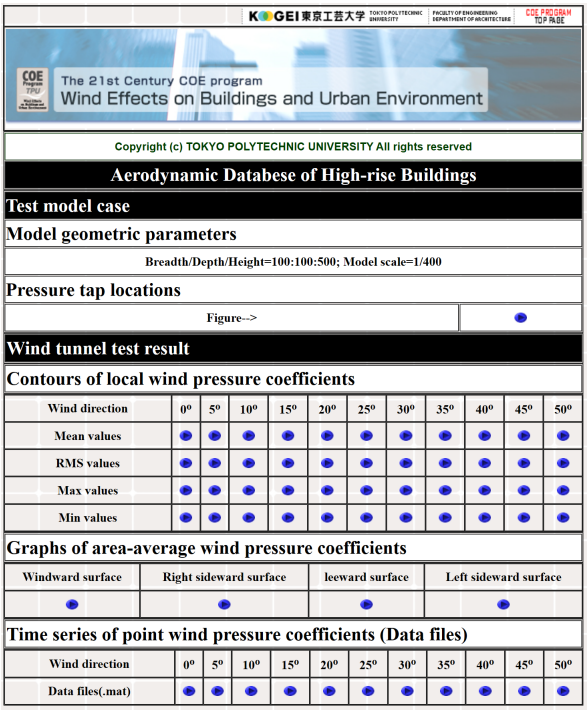

Figure 3.5: Figure of the interface from which accessing to all data referring to the specified configuration. (source: www.wind.arch.t-kougei.ac.jp)

To clarify this aspect, 0 attack angle means wind flow parallel to the normal to Windward surface (i.e. perpendicular to it). Then increasing Angle of Attack follow counterclockwise rotations, meaning that flow is rotating towards being perpendicular to Right-Sideward surface at 90 degrees. Figures 3.7 and 3.6 confirms last statements.

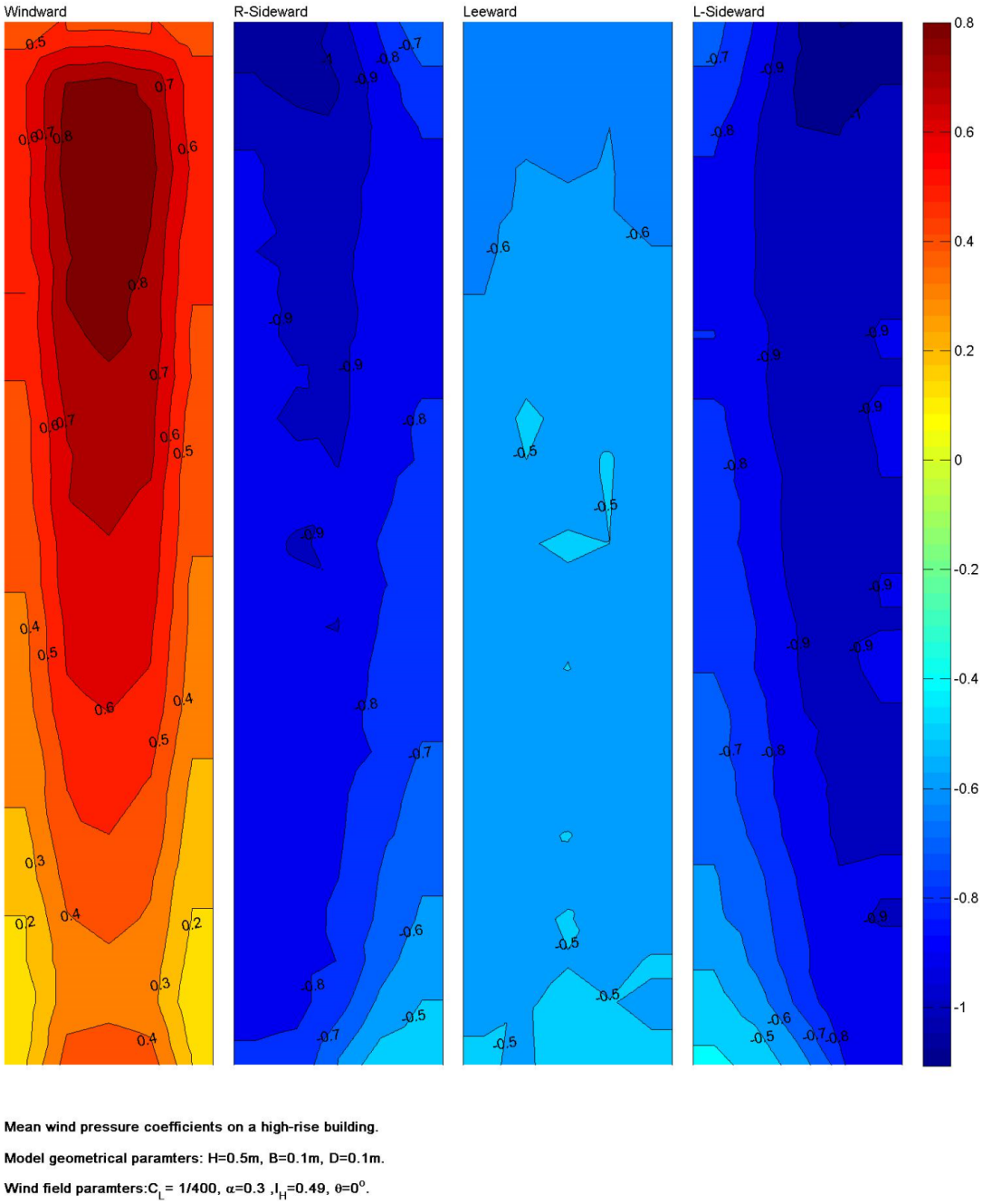

Figure 3.6: Example of local wind pressure coefficients, case T115, 0° angle of attack. (source: www.wind.arch.t-kougei.ac.jp)

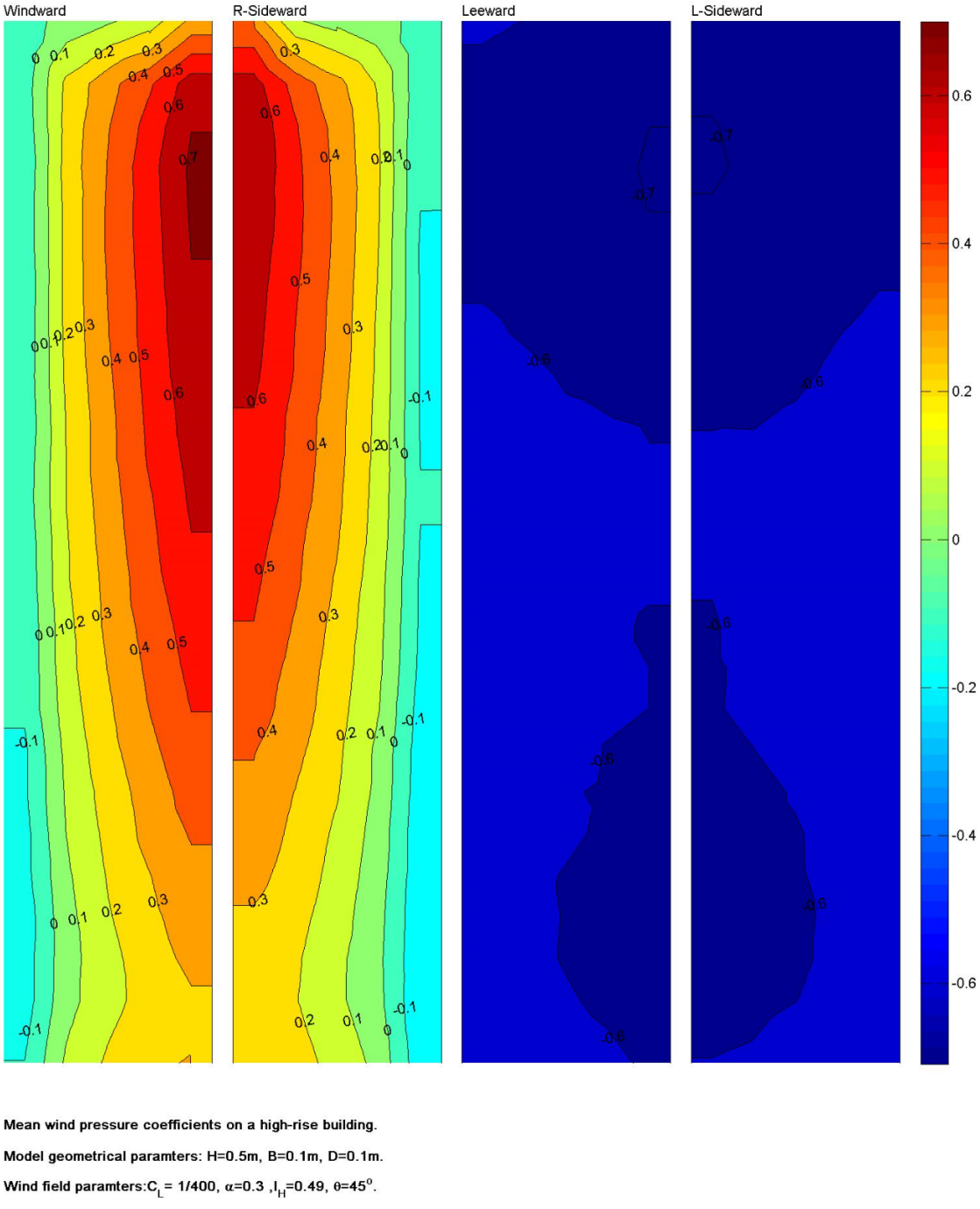

Figure 3.7: Example of local wind pressure coefficients, case T115, 45° angle of attack. (source: www.wind.arch.t-kougei.ac.jp)

NOTE: this implies that, for increasing value of the angle of attack, the structure will exbit negative displacements along x direction (referring to Mode 2), due to the LRS choice, as illustrated in Figure 3.11.

As it can be noticed from Figure 3.8, in the Database, the four Windward, Right-Sideward, Leeward, Left-Sideward surfaces are opened up in the same plane.

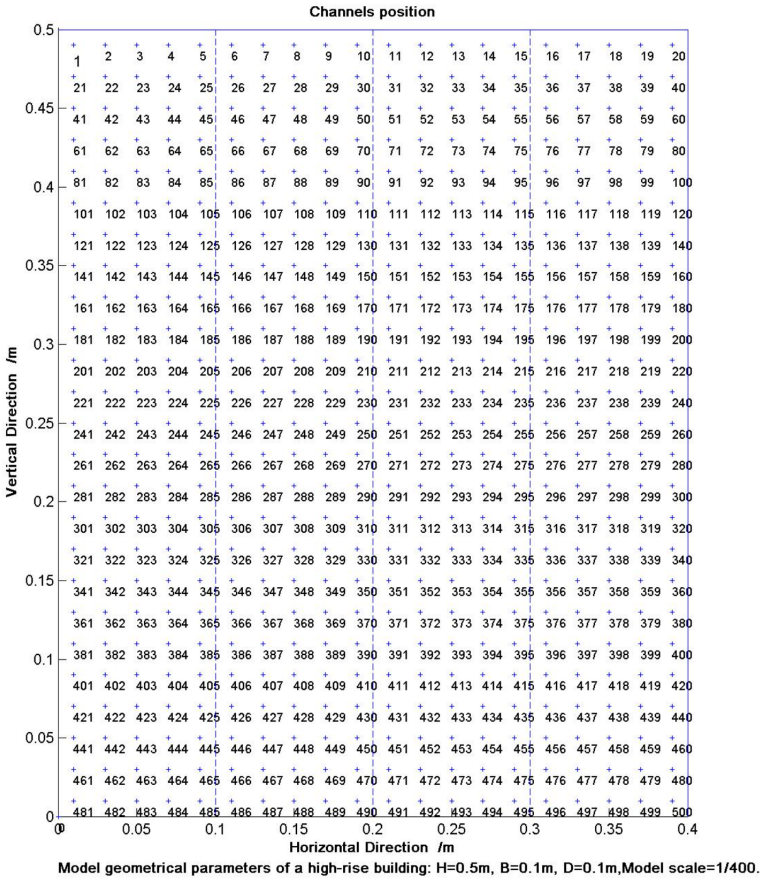

Figure 3.8: Example of figure showing monitor positioning during test (case T115). (source: www.wind.arch.t-kougei.ac.jp)

But clearly in reality they build up a closed rectangular prism. Hence, an operation to bring them in the exact configuration was needed in order to have the exact *(x,y,z)* coordinates for each monitor.

An example of the result of this step can be seen in Figure 3.9 and Figure 3.10 for Windward and Right-Sideward surfaces respectively. The last three lines are referring to x, y and z coordinate respectively.

	1	2	3	4	5	6	7	8	9	10	11	12
1	1	2	3	4	5	21	22	23	24	25	41	42
2	-0.0400	-0.0200	7.4506e-10	0.0200	0.0400	-0.0400	-0.0200	7.4506e-10	0.0200	0.0400	-0.0400	-0.0200
3	-0.0500	-0.0500	-0.0500	-0.0500	-0.0500	-0.0500	-0.0500	-0.0500	-0.0500	-0.0500	-0.0500	-0.0500
4	0.4900	0.4900	0.4900	0.4900	0.4900	0.4700	0.4700	0.4700	0.4700	0.4700	0.4500	0.4500

Figure 3.9: Example of Windward surface node ordering.

It is straightforward to notice that in the case of the Windward surface (this holds for Leeward surface also), y coordinate remains constant at a value of -0.05 m (with respect

	1	2	3	4	5	6	7	8	9	10	11	12
1	6	7	8	9	10	26	27	28	29	30	46	47
2	0.0500	0.0500	0.0500	0.0500	0.0500	0.0500	0.0500	0.0500	0.0500	0.0500	0.0500	0.0500
3	-0.0400	-0.0200	5.9605e-09	0.0200	0.0400	-0.0400	-0.0200	5.9605e-09	0.0200	0.0400	-0.0400	-0.0200
4	0.4900	0.4900	0.4900	0.4900	0.4900	0.4700	0.4700	0.4700	0.4700	0.4700	0.4500	0.4500

Figure 3.10: Example of Right-Sideward surface node ordering.

to LRS, see Figure 3.11) for all the monitors. This is of course true since Windward surface lay on x-z plane (for which y coordinate is fixed).

On the other hand, for the Right-Sideward surface (and therefore Left-Sideward one) it is the opposite. The x coordinate remains constant, since it lays on the x-y plane.

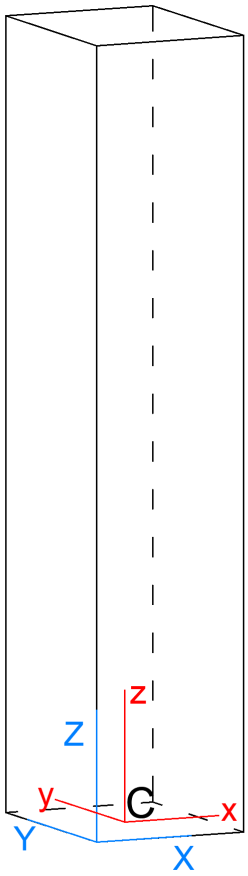

Figure 3.11: Figure showing GRS (in blue) and LRS (red).

Figures 3.9 and 3.10 show the ordering of the monitors belonging to the same surface. They have been piled into a row vector, which has then as many columns as the number of nodes for each surface. The first row contains the progressive monitors number (for each surface as said) in descending order from left to right – as check, see Figure 3.8 and start counting from up-left monitor, toward the right and the going downward; you should find the same order in both cases (this for each of the four surfaces).

3.2 Fourier Numerical Analysis

3.2.1 Computing Forces (model scale)

In Section 3.1 a general overview of the Database upon which this Work is based has been presented.

Among all, the most important info used to initialise the analysis have been the recording of the adimensionalised (with respect to reference height, which in model scale was set to $40cm$) pressure coefficients at each monitor (for each of the four surfaces). The Database furnishes these values in matrix form

$$\begin{bmatrix} C_{p_1}(t_0) & \cdots & C_{p_j}(t_0) & \cdots & C_{p_n}(t_0) \\ \cdots & \ddots & \cdots & \cdots & \cdots \\ C_{p_1}(t_i) & \cdots & C_{p_j}(t_i) & \ddots & C_{p_n}(t_i) \\ C_{p_1}(t_f) & \cdots & C_{p_j}(t_f) & \cdots & C_{p_n}(t_f) \end{bmatrix}$$

where
$C_{p_j}(t_i) =$ pressure coefficient at node$j$ at i^{th} time step;
$n =$ number of monitors (hence, number of columns);
$t_f =$ sampled period $(32.768\ s$ in model scale$)$.

NOTE: number of rows is given by

$$Sample\ period\ \times Sample\ frequency = 32.768 \times 1000 = 32768.$$

However, the goal, as it will be well explained in the following, is to compute modal forces, hence it is needed to convert pressures into force. To do so, an area relative to each monitor pressure needs to be defined.

There are basically two way of defining a reference area:

- Influence area of each node;
- Area of surface's element delimited by four nodes.

In this specific case, the second approach has been adopted. This way, the average pressure on the element's geometric centre will be given by the average of the pressure on the four delimiting nodes:

$$p_{elem} = \frac{p_{node_1} + p_{node_2} + p_{node_3} + p_{node_4}}{4} \tag{3.1}$$

Then, having area and relative pressure acting on each surface's element, force can be computed simply by

$$force = pressure \times area.$$

3.2.2 MDOF systems Dynamic Analysis: solving in modal base

In Section 2 a brief introduction to Dynamic Theory of SDOF systems has been drafted.

However, in quite all the real structural engineering applications, real buildings are characterised by many degrees of freedom, hence they are MDOF (Multi Degree Of Freedom) systems.

Therefore, SDOF theory has to be extended to MDOFs systems. Still, and fortunately enough, this extension is quite straightforward [2].

The general dynamic relation of a damped MDOF system is nothing but the one related to an SDOF system in which structural properties are expressed in matrix form:

$$\mathbf{M}\,\ddot{\mathbf{x}}(t) + \mathbf{C}\,\dot{\mathbf{x}}(t) + \mathbf{K}\,\mathbf{x}(t) = \mathbf{p}(t) \tag{3.2}$$

where **m**, **c** and **k** are *mass*, *damping* and *stiffness* matrix respectively.

In theory, there are basically two ways of solving that system of *N* differential equations in the *N* x_n unknown:

- Direct solving of the N coupled equation;
- Solving the uncoupled problem, by means of a Modal Analysis.

As it can be imagined, the second approach is much faster in computation, since it is based on the solving of N uncoupled equations, which can then be treated as single equations belonging to a SDOF system.

Specifically

$$\mathbf{x}(t) = \mathbf{\Phi} \ * \ \mathbf{q}(t) \tag{3.3}$$

where
$\mathbf{x}(t) =$ displacement vector (unknown) ;
$\mathbf{q}(t) =$ vector of $modal\ amplitudes$ (or $''generalised\ coordinates''$).
$\mathbf{\Phi} =$ Modal Matrix

$$\mathbf{\Phi} = [\phi_1,\ \ldots,\ \phi_i,\ \ldots,\ \phi_n] \tag{3.4}$$

$\phi_i =$ ith column of $\mathbf{\Phi}$, ith modal shape vector;

[2] In most of the cases.

$$\mathbf{\Phi} = \begin{pmatrix} \phi_{11,x} & \cdots & \phi_{1i,x} & \cdots & \phi_{1n,x} \\ \phi_{11,y} & \cdots & \phi_{1i,y} & \cdots & \phi_{1n,y} \\ \vdots & & \vdots & & \vdots \\ \phi_{k1,x} & \cdots & \phi_{ki,x} & \cdots & \phi_{kn,x} \\ \phi_{k1,y} & \cdots & \phi_{ki,y} & \cdots & \phi_{kn,y} \\ \vdots & & \vdots & & \vdots \\ \phi_{N1,x} & \cdots & \phi_{Ni,x} & \cdots & \phi_{Nn,x} \\ \phi_{N1,y} & \cdots & \phi_{Ni,y} & \cdots & \phi_{Nn,y} \end{pmatrix} \tag{3.5}$$

in which $\phi_{ki,x}$ ($\phi_{ki,y}$) are "displacement along *x* (*y*) direction of *k*th node in *i*th mode shape (respectively)".

NOTE: since Mode-shape matrix $\mathbf{\Phi}$ consists of N independent modal vectors, it is *non-singular* and it can be inverted.

Inserting Eq. 3.3 inside Eq. 3.2 and doing some maths, we end up having (for each mode)

$$m_i^* \ \ddot{q}_i(t) + c_i^* \ \dot{q}_i(t) + k_i^* \ q(t) = p_i^*(t) \tag{3.6}$$

where:

$$m_i^* = \mathbf{\Phi_i^T \ M \ \Phi_i}; \tag{3.7}$$

$$c_i^* = \mathbf{\Phi_i^T \ C \ \Phi_i}; \tag{3.8}$$

$$k_i^* = \mathbf{\Phi_i^T \ K \ \Phi_i}; \tag{3.9}$$

are respectively *generalised modal mass*, *damping*[3] and *stiffness* (referring to ith mode).

Dividing by the generalised mass m_i^* we end up with:

$$\ddot{q}_i(t) + 2 \ \xi \ \omega_i \ \dot{q}_i(t) + \omega_i^2 \ q(t) = \frac{p_i^*(t)}{m_i^*} \tag{3.10}$$

where

$$\xi_i = \frac{c_i^*}{2 \ \omega_i \ m_i^*} = \text{modal viscous damping ratio}$$

which solved gives the modal amplitude $q_i(t)$ for mode i.

Regarding the Modal Matrix $\mathbf{\Phi}$, it could be computed analytically by considering some structural characteristics. However, since it is not the scope of This work, three basic

[3] In reality, this is an assumption made to simplify the problem, since theoretically it would be very difficult to precisely evaluate the damping matrix **c** of a MDOF system.

structural mode shapes will be assumed so to be able to perform dynamic modal analysis. This avoids the solving of the classical eigenvalues problem involving mass and stiffness characteristics of the structure. Therefore, in detail, the three assumed mode shapes are:

- Unitary roof displacement along y direction (Mode 1)
- Unitary roof displacement along x direction (Mode 2)
- Unitary roof rotation[4] in the $x - y$ plane (Mode 3)

Following some figures showing some examples.

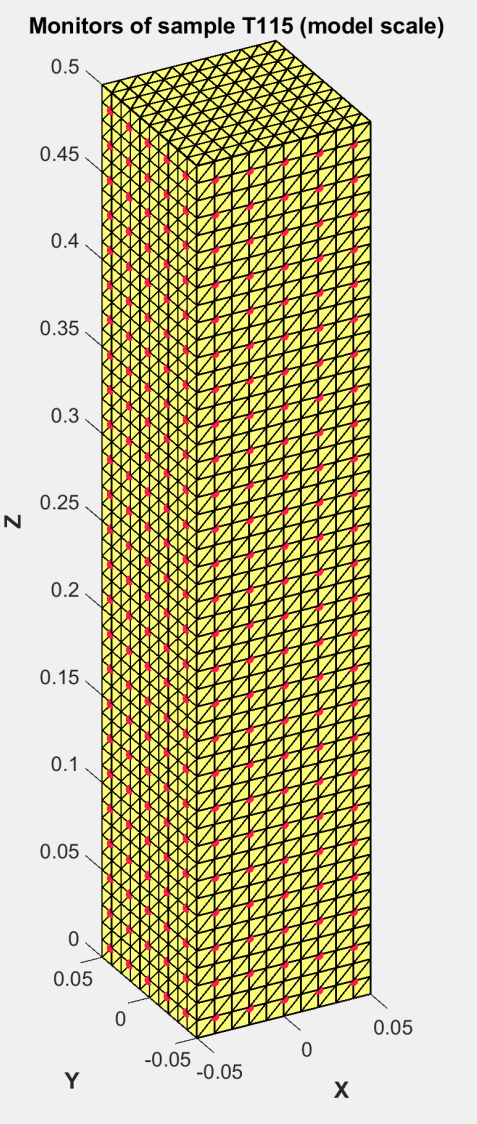

Figure 3.12: Sample T115 (model scale).

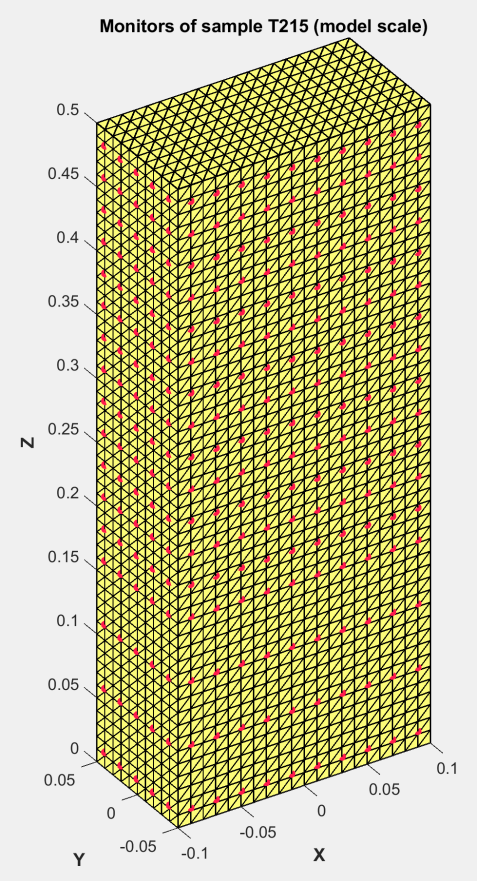

Figure 3.13: Sample T215 (model scale).

[4]With respect to Origin of LRS, see Fig 3.11.

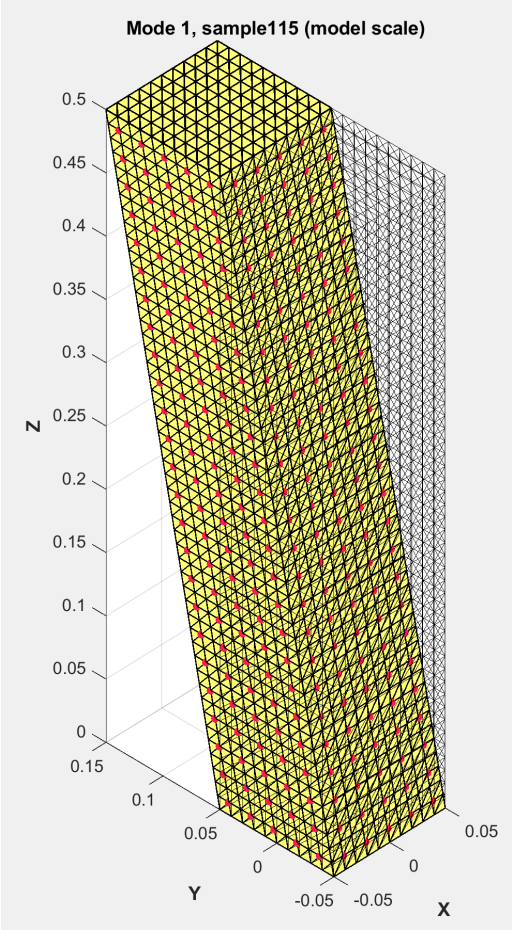

Figure 3.14: Mode 1, sample T115 (model scale).

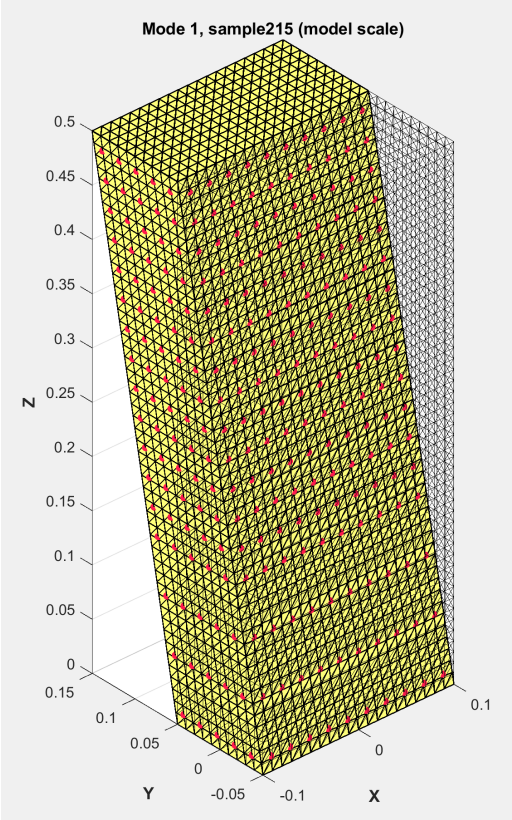

Figure 3.15: Mode 1, sample T215 (model scale).

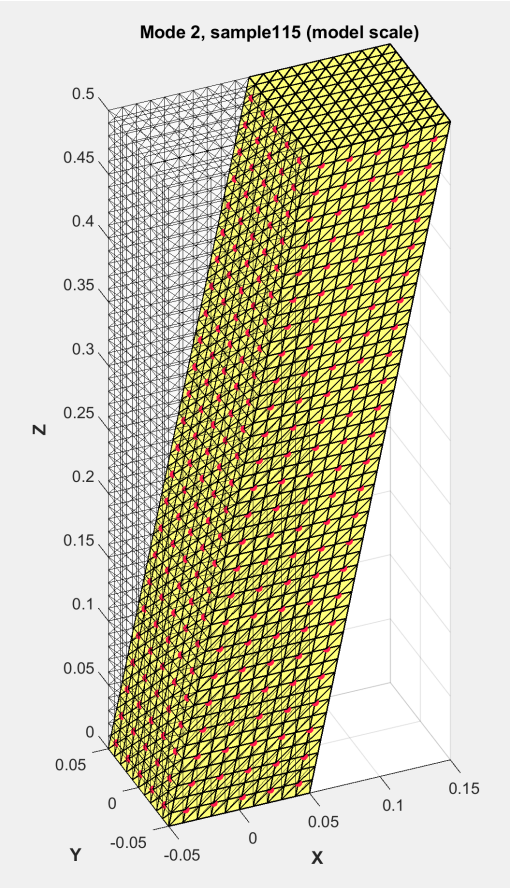

Figure 3.16: Mode 2, sample T115 (model scale).

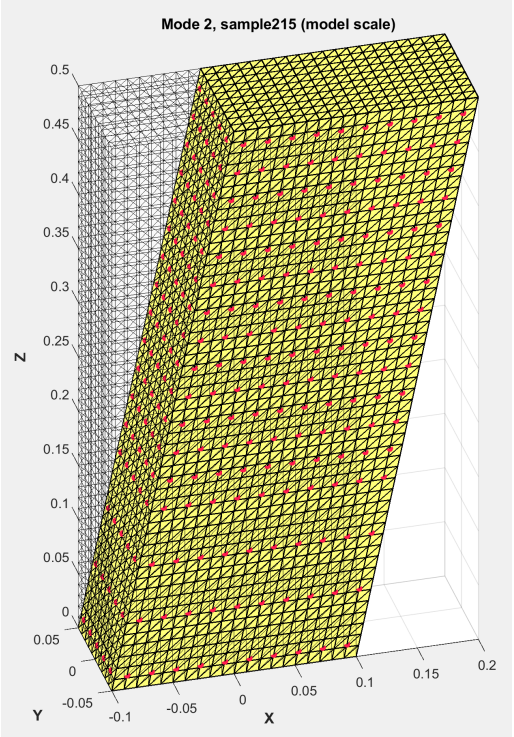

Figure 3.17: Mode 2, sample T215 (model scale).

Figure 3.18: Mode 3, sample T115 (model scale).

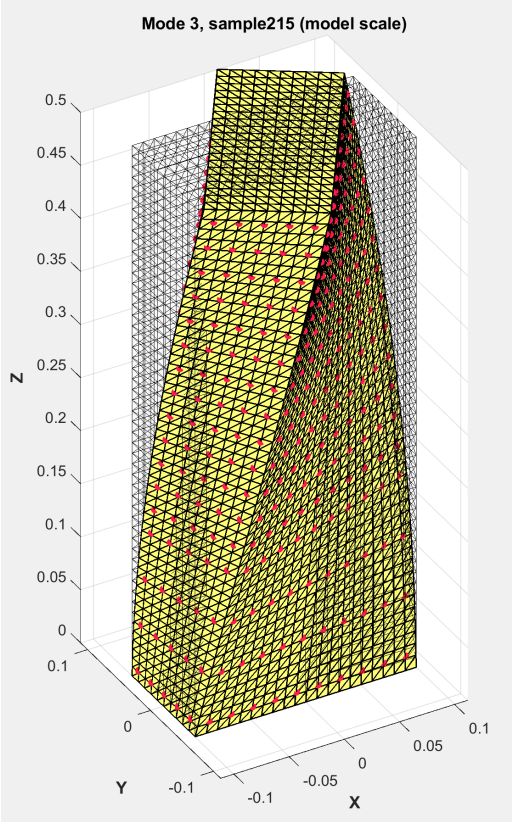

Figure 3.19: Mode 3, sample T215 (model scale).

3.2.3 Computation of Modal Masses

Definition of *Modal* or *Generalised Masses* of the structure is a fundamental step needed to be able to solve the uncoupled equations of motion.

In this Work some assumptions have been made to ease their computation, since their exact estimation is not the scope of this work[5].

Therefore, structures are thought to be framed, with lumped mass model and shear type behaviour.

Floors are supposed $4m$ height, with Table 3.1 defining the parameters needed to define their respective mass.

Building parameters	
Slab Thickness t_{slab}	$0.30\ m$
Concrete density ρ_c	$2500\ \frac{kg}{m^3}$

Table 3.1: Floor building parameters.

Therefore, mass of each floor is given by

$$m_{floor} = t_{slab}\ B\ D\ \rho_c\ \ [\text{kg}] \tag{3.11}$$

Then, matrix of generalised masses can be easily computed as

$$\mathbf{M^*} = \mathbf{\Phi_{floor}^T}\ \mathbf{M}\ \mathbf{\Phi_{floor}} \tag{3.12}$$

where the mass matrix $\mathbf{M}$ is diagonal and has dimension $3\ f\ \times\ 3\ f$, with $f\ =$ number of floors. The elements m_i and J_i are mass and intertia of ith floor respectively.

[5] Also considering that modal masses, although structural properties, constitute somehow only a scaling in the solving of the modal equations of motion.

$$\mathbf{M} = \begin{pmatrix} m_f & & & & & & & & & & & \\ & \ddots & & & & & & & & & & \\ & & m_i & & & & & & & & & \\ & & & \ddots & & & & & & & & \\ & & & & m_1 & & & & & & & \\ & & & & & m_f & & & & & & \\ & & & & & & \ddots & & & 0 & & \\ & & & & & & & m_i & & & & \\ & & & & 0 & & & & \ddots & & & \\ & & & & & & & & & m_1 & & \\ & & & & & & & & & & m_f & \\ & & & & & & & & & & & \ddots \\ & & & & & & & & & & & & m_i \\ & & & & & & & & & & & & & \ddots \\ & & & & & & & & & & & & & & m_1 \end{pmatrix} \tag{3.13}$$

The modal shape matrix is obtained the same way as stated before in Section 3.2.2, Eq 3.5. In this specific case, it will take the following shape:

$$\mathbf{\Phi_{floor}} = \begin{pmatrix} \frac{v_{top}}{H} * z_f & 0 & 0 \\ \vdots & \vdots & \vdots \\ \frac{v_{top}}{H} * z_i & 0 & 0 \\ \vdots & \vdots & \vdots \\ \frac{v_{top}}{H} * z_1 & 0 & 0 \\ \vdots & \vdots & \vdots \\ 0 & \frac{u_{top}}{H} * z_f & 0 \\ \vdots & \vdots & \vdots \\ 0 & \frac{u_{top}}{H} * z_i & 0 \\ \vdots & \vdots & \vdots \\ 0 & \frac{u_{top}}{H} * z_1 & 0 \\ \vdots & \vdots & \vdots \\ 0 & 0 & \frac{r_{top}}{H} * z_f \\ \vdots & \vdots & \vdots \\ 0 & 0 & \frac{r_{top}}{H} * z_i \\ \vdots & \vdots & \vdots \\ 0 & 0 & \frac{r_{top}}{H} * z_1 \end{pmatrix} \tag{3.14}$$

3.2.4 Computation of Modal Forces: projection in real scale

Once Modal Matrix $\mathbf{\Phi}$ has been defined, computing modal forces is quite straightforward:

$$\mathbf{p}^*(t) = \mathbf{\Phi^T} * \mathbf{p}(t) \tag{3.15}$$

In previous section, in Eq 3.5 each column of $\mathbf{\Phi}$ ϕ_i was defined as the vector of the ith modal shape, which dimension is $2 * number_{nodes} \times 1$: this because each node was counted for its x and y displacement, hence twice. Because of this, for dimension congruence making the matrix product in Eq 3.15 possible, $\mathbf{p}(t)$ has to have first dimension equal to first dimension $\mathbf{\Phi}$: this implies that also $\mathbf{p}(t)$ has to count twice for each node. This is done by simply considering the relative pressure along x and y direction respectively for each node. Of course, this is just a tricky operation to make the product possible: it is obvious that, depending on the considered surface, either pressures along x or y direction will be equal to 0[6].

However, up to now, everything was based on model scale, which parameters (reference wind speed at the reference height) were introduced in Section 3.1.

To bring everything in real scale, a scaling operation is needed. Scaling is based on the conservation of the Strouhal Number, which is defined as

$$St = \frac{f\ L}{v} \tag{3.16}$$

where
$f =$ frequency of $vortex\ shedding$;
$L =$ characteristic length;
$v =$ flow velocity.

Conservation if the Strouhal Number implies that

$$St_{model} = \frac{f_{model}\ L_{model}}{v_{model}} = \frac{f_{real}\ L_{real}}{v_{real}} = St_{real} \tag{3.17}$$

Solving for the ratio of vortex shedding frequencies, we end up having:

$$\frac{f_{model}}{f_{real}} = \frac{L_{real}}{L_{model}}\ \frac{v_{model}}{v_{real}} \tag{3.18}$$

[6]This is simply due to the fact that pressure taps used in Wind Tunnel Test are able to measure only pressure perpendicular to the relative surface.

Setting as reference mean wind speed in real scale[7][8] to

$$v_{m,real} = 30\ \frac{m}{s}$$

and noting that

$$T = \frac{1}{f} = \text{period [s]} \tag{3.19}$$

we finally have as time scale[9]

$$T_{real} = T_{model}\ *\ \frac{L_{real}}{L_{model}}\ \frac{v_{model}}{v_{real}} = T_{model}\ *\ \frac{400}{1}\ *\ \frac{11.016}{30}\ \ [s] \tag{3.20}$$

Surface elements' forces in real scale are related to the reference pressure in real scale

$$p_{h_{real}} = \frac{1}{2}\ \rho_{air}\ v_{m,real} \tag{3.21}$$

by the relation

$$F_{real}(t) = F_{model}(t)\ \times p_{h_{real}}\ \times lengthscale^2 \tag{3.22}$$

Thus finally, modal forces in real scale (in time) are recovered by simply premultiplying Eq 3.22 by $\mathbf{\Phi^T}$

$$\mathbf{p}^*(t) = \mathbf{\Phi^T}\ *\ F_{real}(t) \tag{3.23}$$

At the end of the section, Figures 3.20, 3.21, 3.22, 3.23 and 3.24 show some example of time history of modal forces for different configurations and angle of attack.

3.2.5 Solving the equation of motion: Fourier Analysis

Having computed the modal forces, it is then possible to solve the three[10] uncoupled equations of motion as Eq 3.6 (or 3.10 in its adimensionalised form).

[7] **NOTE**: this is an assumption: however, it has to be performed carefully, since then pressures depend on the square of the reference wind speed, as it will stated in the following.

[8] 30 $\frac{m}{s}$ is a quite high value of mean wind speed. However, it has been kept to be on the safe side, since this will lead to light overestimation of response.

[9] Important is to note that a shift in time axis, hence a different time scaling (which depends on the assumed value of wind speed at real scale), may modify the frequency content of the Fourier Transform of the modal forces, which will be detailed in the following.

[10] Following the assumption on the modal shapes.

It can be done either in time domain (Duhamel Integral) or in frequency domain (Fourier Analysis). The second approach will be followed, since it exploits the frequency content of the input signal (i.e. the dynamic wind loading, under the form of modal forces) and puts it in relation with the frequency content of the output signal (modal responses), and it can also be applied in case of non linear systems.

Therefore, for sake of clarity we recall the equation of motion in the time domain:

$$m_i^* \ \ddot{q}_i(t) + c_i^* \ \dot{q}_i(t) + k_i^* \ q(t) = p_i^*(t) \tag{3.24}$$

which can be solved once natural modal circular frequencies ω_i and damping ratio coefficients ξ_i are known (or estimated).

Multiplying both members on the right by $\exp(-i\,\overline{\omega}\,t)$ and taking the integral between $-\infty$ and $+\infty$ in time, we have

$$\begin{aligned} &\int_{-\infty}^{\infty} (m_i^* \ \ddot{q}_i(t) + 2\ \xi\ \omega_i\ m_i^*\ \dot{q}_i(t) + \omega_i^2\ m_i^*\ q(t))\ \exp(-i\,\overline{\omega}\,t)\ dt = \\ &= \int_{-\infty}^{\infty} p_i^*(t)\ \exp(-i\,\overline{\omega}\,t)\ dt \quad \text{(i = 1,2,3)} \end{aligned} \tag{3.25}$$

which can be rewritten as[11]

$$-\ m_i^*\ \Omega^2\ Q_i(\Omega) + 2\ i\ \xi_i\ \omega_i\ m_i^*\ \Omega\ Q_i(\Omega) + \omega_i^2\ m_i^*\ Q_i(\Omega) = P_i^*(\Omega) \tag{3.26}$$

where

$$Q_i(\Omega) = \int_{-\infty}^{\infty} q_i\ \exp(-i\,\overline{\omega}\,t)\ dt \tag{3.27}$$

$$P_i^*(\Omega) = \int_{-\infty}^{\infty} p_i^*(t)\ \exp(-i\,\overline{\omega}\,t)\ dt \tag{3.28}$$

are Fourier Transforms of the modal coordinate q_i and modal force $p_i^*(t)$ respectively.

Eq 3.26 can be rewritten as

$$Q_i(\Omega) = \frac{1}{k_i^*} \frac{1}{-\Omega^2 + 2\ i\ \xi_i\ \omega_i\ \Omega + \omega_i^2}\ P_i^*(\Omega) \tag{3.29}$$

Calling

$$H_i(\Omega) = \frac{1}{k_i^*} \frac{1}{-\Omega^2 + 2\ i\ \xi_i\ \omega_i\ \Omega + \omega_i^2} \tag{3.30}$$

[11] Including integration by parts.

where $H_i(\Omega)$ is the *"complex frequency response function"* or *"Transfer Function"*, which only depends on structural characteristics (hence, it does not depend on external loading), we end up with

$$Q_i(\Omega) = H_i(\Omega) \;\; P_i^*(\Omega) \tag{3.31}$$

NOTE: Ω denotes the frequency of the input signal (dynamic wind loading), also called *"forcing frequency"*, which is different from the natural modal circular frequencies of the structure ω_i.

Solving Eq 3.31 will lead in the determination of the complex modal amplitudes $Q_i(\Omega)$ in the frequency domain (i.e. their frequency content).

To step back into the time domain, the Inverse Fourier Transform is applied to the complex modal amplitudes in the frequency domain, hence obtaining the time history of the modal amplitudes

$$q_i(t) = \int_{-\infty}^{\infty} Q_i(\Omega) \;\; \exp(i \, \varpi \, t) \; d\Omega \tag{3.32}$$

or in its discrete form (which is the case in the actual computation)

$$q_i(t) = \sum_{f=1}^{N_f} real(Q_i(\Omega) \;\; \exp(i \, \varpi \, t) \;) \tag{3.33}$$

Then, having time history of modal amplitudes, by means of modal recomposition, it is possible to compute time history of displacements, as given in Eq 3.3.

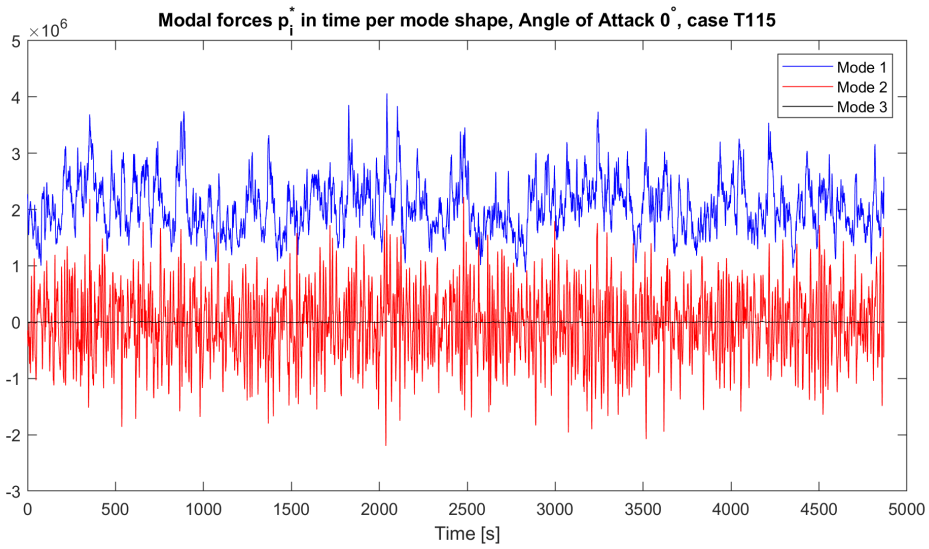

Figure 3.20: Time history of Modal Forces, case T115, angle of attack 0°.

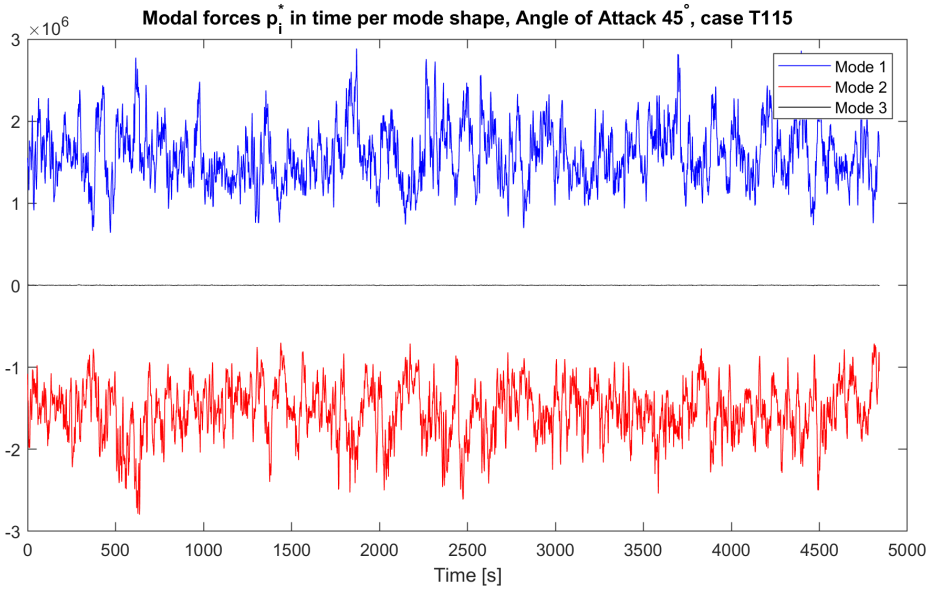

Figure 3.21: Time history of Modal Forces, case T115, angle of attack 45°.

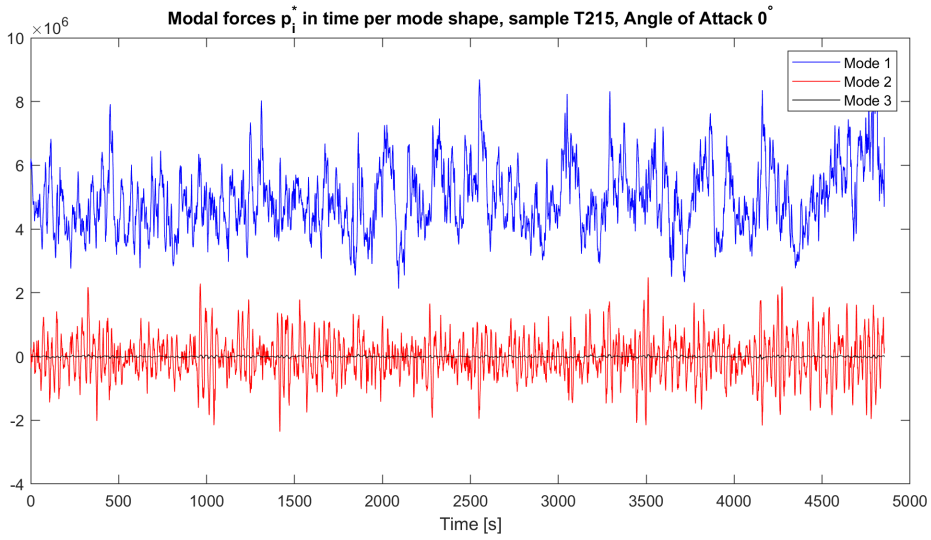

Figure 3.22: Time history of Modal Forces, case T215, angle of attack 0°.

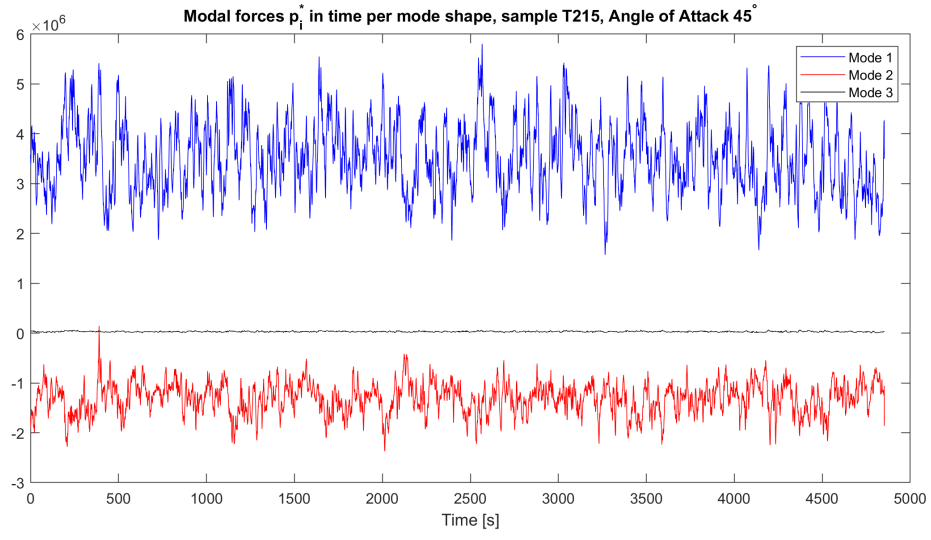

Figure 3.23: Time history of Modal Forces, case T215, angle of attack 45°.

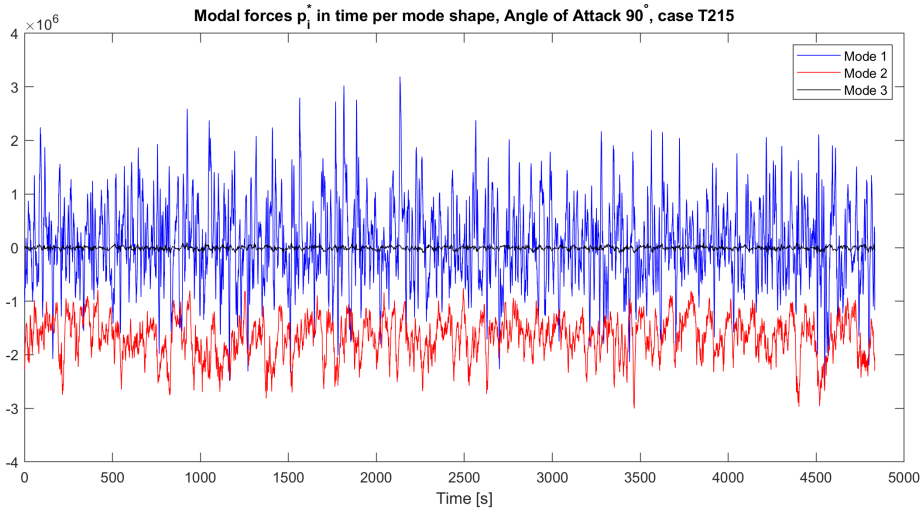

Figure 3.24: Time history of Modal Forces, case T215, angle of attack 90°.

Next they will be shown some results of the Fourier Analysis regarding the most relevant cases that have been studied.

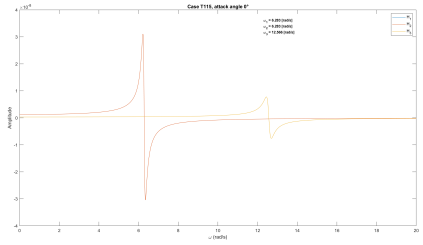

Figure 3.25: Transfer Functions, sample T115, case 1.

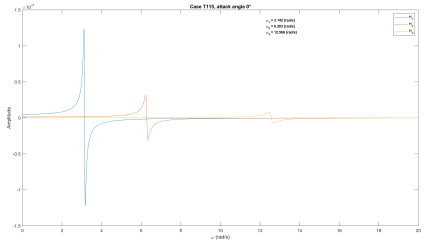

Figure 3.26: Transfer Functions, sample T115, case 2.

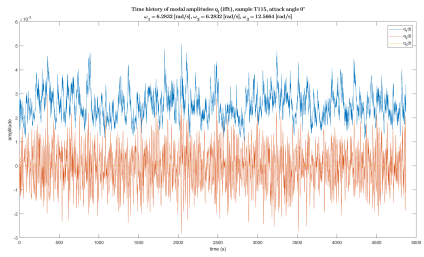

Figure 3.27: Modal amplitudes, sample T115, attack angle 0°, case 1.

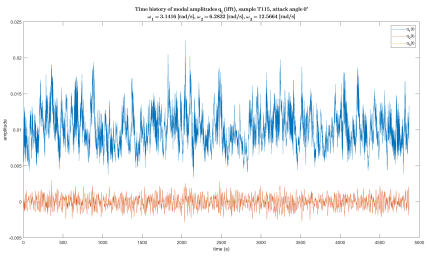

Figure 3.28: Modal amplitudes, sample T115, attack angle 0°, case 2.

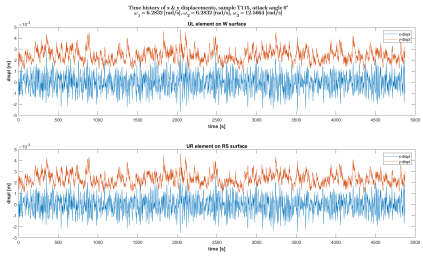

Figure 3.29: Displacements, sample T115, attack angle 0°, case 1.

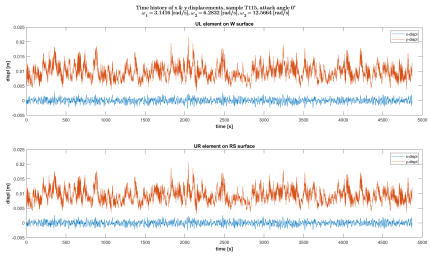

Figure 3.30: Displacements, sample T115, attack angle 0°, case 2.

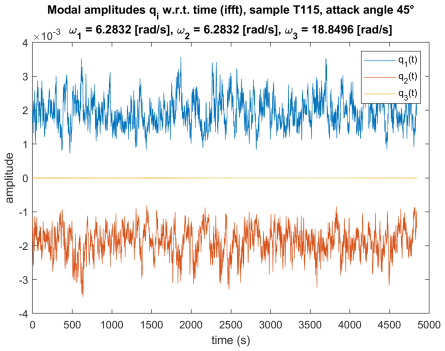

Figure 3.31: Modal amplitudes, sample T115, attack angle 45°, case 1.

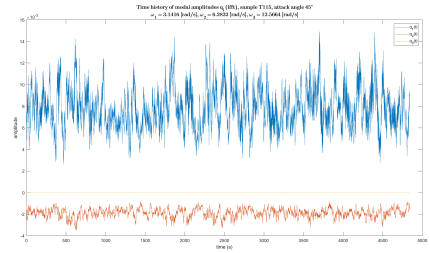

Figure 3.32: Modal amplitudes, sample T115, attack angle 45°, case 2.

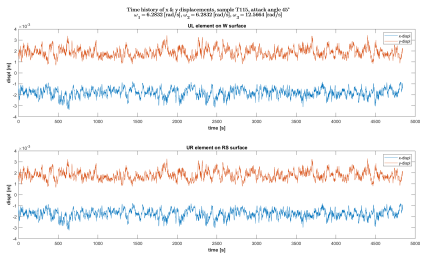

Figure 3.33: Displacements, sample T115, attack angle 45°, case 1.

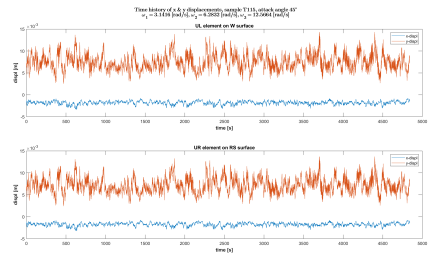

Figure 3.34: Displacements, sample T115, attack angle 45°, case 2.

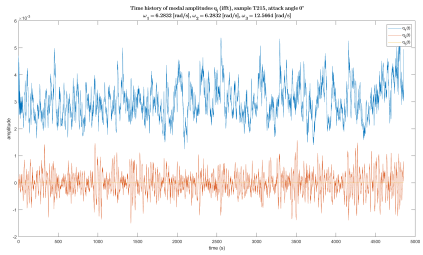

Figure 3.35: Modal amplitudes, sample T215, attack angle 0°, case 1.

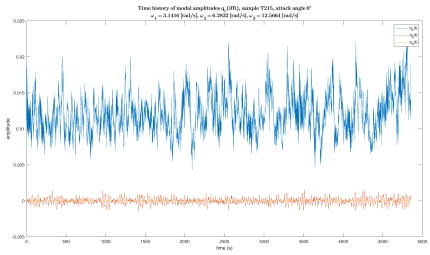

Figure 3.36: Modal amplitudes, sample T215, attack angle 0°, case 2.

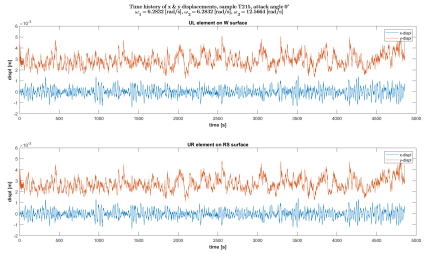

Figure 3.37: Displacements, sample T215, attack angle 0°, case 1.

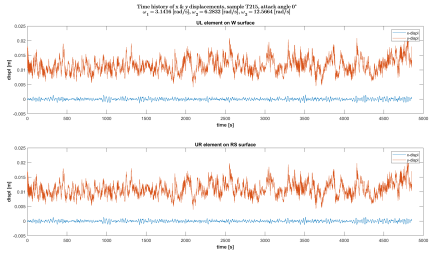

Figure 3.38: Displacements, sample T215, attack angle 0°, case 2.

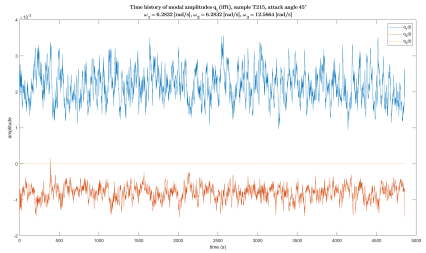

Figure 3.39: Modal amplitudes, sample T215, attack angle 45°, case 1.

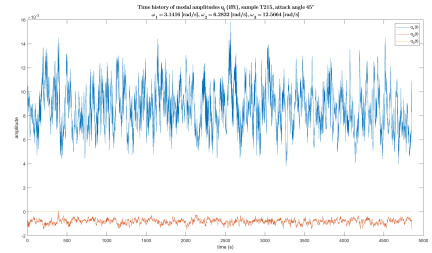

Figure 3.40: Modal amplitudes, sample T215, attack angle 45°, case 2.

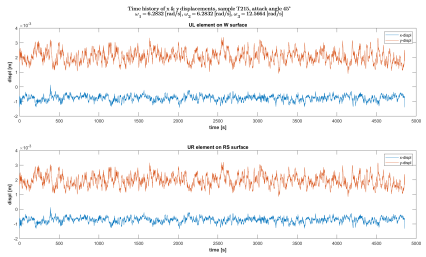

Figure 3.41: Displacements, sample T215, attack angle 45°, case 1.

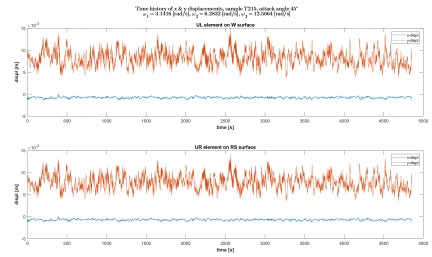

Figure 3.42: Displacements, sample T215, attack angle 45°, case 2.

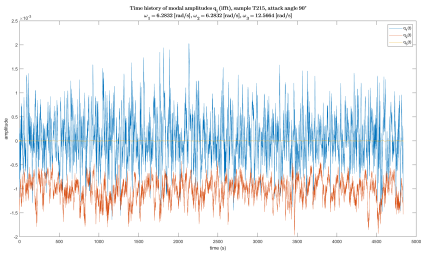

Figure 3.43: Modal amplitudes, sample T215, attack angle 90°, case 1.

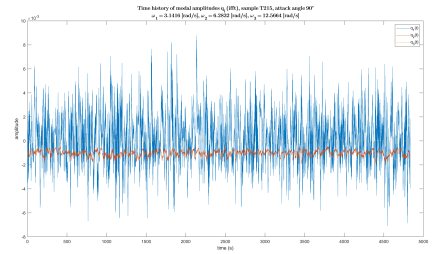

Figure 3.44: Modal amplitudes, sample T215, attack angle 90°, case 2.

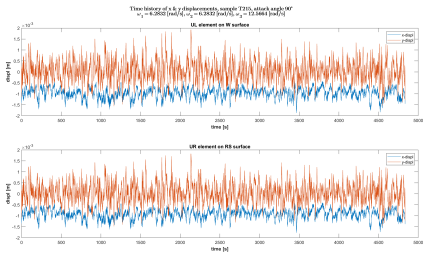

Figure 3.45: Displacements, sample T215, attack angle 90°, case 1.

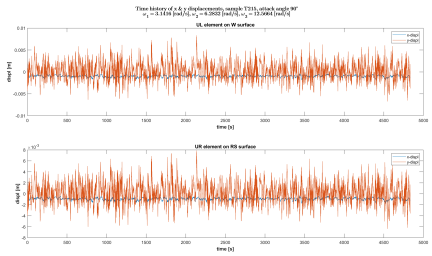

Figure 3.46: Displacements, sample T215, attack angle 90°, case 2.

4 Background and Resonant (B&R) response

In this section, a stochastic approach to the problem will be presented and detailed, with the objective of confirming the validity of it when applied to Dynamic Wind Loading Analysis.

Firstly, a theoretical background on the topic will be presented, such that the reader can have a better understanding of the key concepts that it is intended to confirm by numerical analysis.

Then, results will be presented.

4.1 Random Processes: Autocorrelation and Power Spectral Density Functions

A *random process* p is defined as a "*family (or* 'ensemble'*) of* N *random variables* p_n *related to a similar phenomenon which might be function of one or more independent variables*[1]". [1]

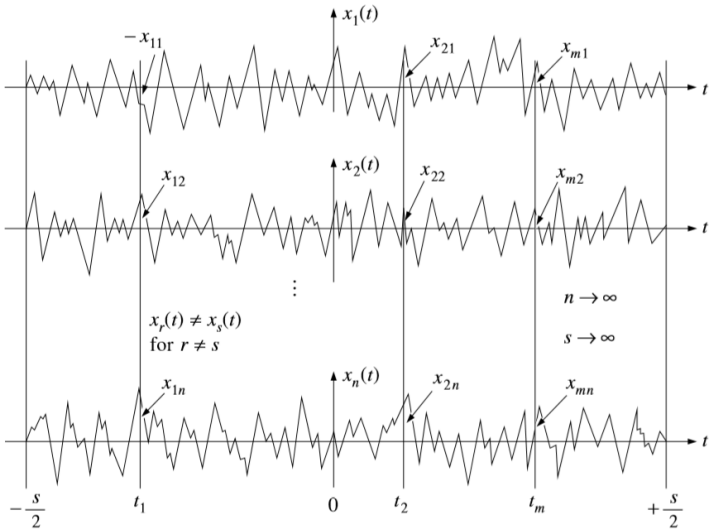

Figure 4.1: Example of a random process, depending on the sole variable time *t*, [1].

This is the case of quite all natural (and non) phenomena which surround us every day.

[1] i.e., time, space, etc.

Consider, for example, the throw of a dice[2], the difference in temperature (°C) between Liège and Bologna the Christmas day, as well as the dynamic response of a point of a structure, the evolution of the roughness along a road, the ground acceleration during an earthquake, etc.

One of the main features of random process is that, a measurement of it (which represents a random variable, one of the N constituting the ensemble) is unique and cannot be reproduced.

Of course, in this category falls also the time evolution of the wind speed in a given point in space. When someone, for example, measures the wind speed in a point in a time interval of 10 minutes, which is an aleatory process, it has nothing but that single measurement.

However, there exist some general features of that measurement such that, repeating an high number of times the same aleatory process (i.e. 10 minutes wind speed measurement at the same point in space), it is possible to obtain a *statistical* estimation of the *probabilistic* quantity used, then, to model the process [3].

As a matter of fact, since it can be considered for the majority of the real phenomena, only *stationary* processes will be considered in this discussion. A process is defined stationary if all ensemble averages of the process (mean, mean square values, variance, covariance, correlation coefficient, among the most important) do not depend on time t.

If additionally, for the process, any average obtained with respect to time t along any member r of the ensemble is exactly equal to the corresponding average across the ensemble at an arbitrary time t, the process is also said to be *ergodic*.

Therefore, considering, for sake of simplicity, a random process[3] depending on a single variable, which may be time t (as the one shown in Figure 4.1), the *autocovariance function*[4]

$$E[p^*(t)\, p^*(t+\tau)] \tag{4.1}$$

will be independent of time t (for the stationary property) and therefore will be only function of the time lag τ [1].

Consequently, this function of τ only will be referred as *"autocorrelation function*[5]*"* and is defined as

$$R_{p^*}(\tau) = E\left[p^*(t)\, p^*(t+\tau)\right] \tag{4.2}$$

[2]This case is monodimensional.

[3]**NOTE**: In the following, random process will refer to the modal forces p_i^*.

[4]Which is an ensemble average of order 2.

[5]The autocorrelation function $R_p^*(\tau)$ computes namely the correlation, "inside" the same process (this is why "auto"), of the values assumed by the random process $p^*(t)$ at time t and$t+\tau$. However, being it independent of t, it then only depends on the "distance" in time for which computing the autocorrelation function of the random process. The longer the time lag (i.e. the greater τ), the lower the correlation between the values assumed by the random process.

Autocorrelation function has some important properties:

$$R_{p^*}(0) = \sigma^2_{p^*} \ \text{(variance of } p^*(t)) \tag{4.3}$$

$$R_{p^*}(-\tau) = R^*_p(\tau) \tag{4.4}$$

$$|R_{p^*}(\tau)| < R_{p^*}(0) \tag{4.5}$$

Thus, considering *stationary* processes, the *autocovariance function* (which is the *centered autocorrelation function*) is given by

$$R_{p^*p^*}(\tau) = \lim_{T \to \infty} \frac{1}{T} \int_{-T/2}^{T/2} p^*(t)\, p^*(t+\tau)\, d\tau \tag{4.6}$$

NOTE: the *Theorem of Ergodicity* shows that also for stationary non-ergodic random processes the Autocorrelation Function of the random process (made by many random variable, e.g. wind speed measurements) does not change whether it is computed across the whole process (i.e. across the ensemble) or along one single random variable (i.e. a single measurement). This allows to fully characterise the process by simply characterising a single random variable.

As it has been said in Section 2.2, any random variable $p^*_r(t)$ of a real stationary random process $p^*(t)$ (i.e. wind speed) can be separated into its frequency components by means of Fourier Analysis.

Considering the same time interval $-s/2 < t < s/2$, it can be expressed as

$$p^*_r(t) = \sum_{n=-\infty}^{\infty} C_{nr}\ \exp(i\, n\, \overline{\omega}_0\, t) \tag{4.7}$$

in which

$$C_{nr} = \frac{1}{s} \int_{-s/2}^{s/2} p^*_r(t)^2\ \exp(-i\, n\, \overline{\omega}_0\, t)\, dt \tag{4.8}$$

are the complex coefficients, $\overline{\omega}_0 = \frac{2\,\pi}{s}$.

In most cases, the quantity of most interest when analysing stationary random processes is the *mean square value* of each of the r random variables constituting the random process $p^*(t)$, over the interval $-s/2 < t < s/2$

$$\langle p^*_r(t)^2 \rangle = \frac{1}{s} \int_{-s/2}^{s/2} p^*_r(t)^2\, dt \tag{4.9}$$

Merging Eqs 4.7, 4.8 and 4.9 we obtain

$$\langle p_r^*(t)^2 \rangle = \sum_{n=-\infty}^{\infty} \frac{|\int_{-s/2}^{s/2} p_r^*(t)^2 \ \exp(-i\ n\ \overline{\omega}_0\ t)\ dt|^2}{2\ \pi\ s} \tag{4.10}$$

Letting $s \ \rightarrow \ \infty$, $\Delta\overline{\omega} \rightarrow d\overline{\omega}$ and $n\ \omega_0 \rightarrow \overline{\omega}$ the summation becomes an integral

$$\langle p_r^*(t)^2 \rangle = \int_{-\infty}^{\infty} \mathbf{S}_{p_r^*}(\overline{\omega})\ d\overline{\omega} \tag{4.11}$$

where

$$\mathbf{S}_{p_r^*}(\overline{\omega}) \equiv \lim_{s \rightarrow\ \infty} \frac{|\int_{-s/2}^{s/2} p_r^*(t)^2 \ \exp(-i\ n\ \overline{\omega}_0\ t)\ dt|^2}{2\ \pi\ s} \tag{4.12}$$

is defined as the *"Power Spectral Density Funtion"* of the random variable $p_r^*(t)$[6].

It is then straightforward to affirm that the power spectral density function for the entire stationary random process $p^*(t)$ is given by averaging the power spectral density functions for individual members across the ensemble ([1])

$$\mathbf{S}_{p^*}(\overline{\omega}) = \lim_{n\ \rightarrow\ \infty}\ \frac{1}{n}\ \sum_{r=1}^{N}\ \mathbf{S}_{p_r^*}(\overline{\omega}) \tag{4.13}$$

Thus

$$\langle p_r^*(t)^2 \rangle = \int_{-\infty}^{\infty} \mathbf{S}_{p^*}(\overline{\omega})\ d\overline{\omega} \tag{4.14}$$

Very interesting is the correlation, for stationary random process p(t), between Autocorrelation $R_{p^*}(\tau)$ and Power Spectral Density functions $\mathbf{S}_{p^*}(\overline{\omega})$.

It can be demonstrated that the Power Spectral Density function is nothing but $1/2\ \pi$ times the Fourier Transform of the Autocorrelation function, that is ([4])

$$\mathbf{S}_{p^*}(\overline{\omega}) = \frac{1}{2\ \pi}\ \int_{-\infty}^{\infty} R_{p^*}(\tau)\ \exp(-i\ \overline{\omega}\ t)\ d\tau \tag{4.15}$$

and consequently

$$R_{p^*}(\tau) = \int_{-\infty}^{\infty} \mathbf{S}_{p^*}(\overline{\omega})\ \exp(i\ \overline{\omega}\ t)\ d\overline{\omega} \tag{4.16}$$

[6]Where we remember that random variable $p_r^*(t)$ is the rth sample of the random process $p^*(t)$.

Remembering the first property of the Autocorrelation function $R_p(\tau)$ given in Eq 4.3

$$R_{p^*}(0) = \int_{-\infty}^{\infty} \mathbf{S}_{p^*}(\overline{\omega})\, d\overline{\omega} = \sigma_{p^*}^2 \tag{4.17}$$

which states that the "integral of the Power Spectral Density Function across the frequency domain equals the variance of the considered random process" ([1]). It then represents the *frequency distribution* of the energy (i.e. the variance) contained in the random process ([6]).

However, of major interest is the link that exists between Power Spectral Density Function (or Autocorrelation Function) of input process $p^*(t)$ and the output process $q(t)$ (modal structural responses).

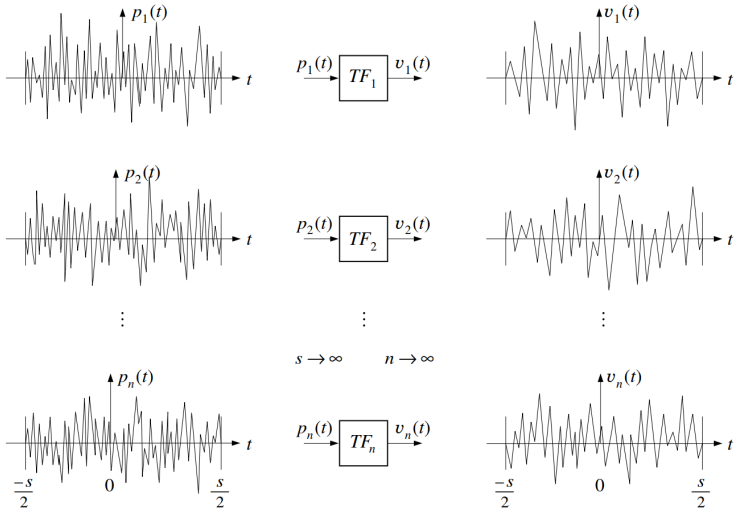

Figure 4.2: Input and output processes of a stable linear SDOF system,

As already stated for the input signal, relation between Power Spectral Density and Autocorrelation Functions are also valid for output signal, that is

$$S_q(\overline{\omega}) = \frac{1}{2\,\pi} \int_{-\infty}^{\infty} R_q(\tau)\ \exp(-i\,\overline{\omega}\,\tau)\, d\tau \tag{4.18}$$

Substituting Eq 4.16 into Eq 4.18 and doing some math, we can finally ascertain that Power Spectral Density Function of output system is linked to the Power Spectral Density Function of the input process by the relation ([1])

$$S_q(\overline{\omega}) = \mathbf{H}(-i\,\overline{\omega})\ \mathbf{H}(i\,\overline{\omega})\ S_{p^*}(\overline{\omega}) \tag{4.19}$$

in which $\mathbf{H}(i\overline{\omega})$ is the "*frequency-domain complex transfer function* between loading and response".

Extending to MDOFs systems is quite straightforward.

Recalling Section 3.2.5 in which was stated that dynamic response of a linear MDOF system can be determined by the solving of the modal equations of motion as expressed by Eq 3.24. Then, total response is given by superposition of modal responses by means of modal shapes,

$$x(t) = \sum_{n=1}^{3} \phi_n \, q_n(t) \tag{4.20}$$

If random excitations (dynamic wind loading) are assumed to be stationary (which is the quite always the case), the response will also be stationary, which allows to affirm that, based on what has been stated in this section at page 44, Eq 4.2, autocorrelation function of response, given by

$$R_x(\tau) = E\left[x(t)\; x(t+\tau)\right] \tag{4.21}$$

is independent of variable time t, hence only dependent on time shift τ.

After doing some maths, it can be demonstrated that

$$R_x(\tau) = \sum_{m} \sum_{n} R_{x_m x_n}(\tau) \qquad m, n = 1, 2, 3 \tag{4.22}$$

where

$$R_{x_m \, x_n}(\tau) = \int_0^\infty \int_0^\infty \phi_m \, \phi_n \, R_{p_m p_n}(\tau \; - u_2 + u_1) \, h_m(u_1) \, h_n(u_2) \, du_1 \, du_2 \tag{4.23}$$

$R_{p_m p_n}(\tau)$ is the *covariance funtion* of random variables $p_m(t)$ and $p_n(t+\tau)$, $R_{x_m \, x_n}(\tau)$ is the *covariance function of modal responses* $x_m(t)$ and $x_n(t+\tau)$ [1].

However, for systems with very low damping (i.e. for $\xi_i \ll 1$) and well-separated modal frequencies[7], response process $x_m(t)$ produced by mode m is almost statistically independent of response $x_n(t)$ produced by mode n. This means that cross terms in Eq 4.22 are almost equal to zero. Therefore, autocorrelation function of total response can be approximated by the relation

$$R_x(\tau) \doteq \sum_{m} R_{x_m x_m}(\tau) \tag{4.24}$$

where

$$R_{x_m x_m}(\tau)$$

[7] As is usually the case in Structural Engineering.

is the *Autocorrelation Function* for process $x_m(t)$. When τ is equal to 0, recalling the first property of the Autocorrelation Function given by Eq 4.3, Eq 4.24 can be expressed in terms of standard deviations, that is ([1])

$$\sigma_x = \left(\sigma_{x_1}^2 \ + \sigma_{x_2}^2 \ + \sigma_{x_3}^2\right)^{1/2} \tag{4.25}$$

which supports the common square-root-of-the-sum-of-squares (SRSS) method of weighting the maximum normal mode responses when estimating maximum total response[8].

Then, Power Spectral Density Function of the response is $1/2\pi$ the Fourier Transform of the Autocorrelation Function (of the response) [1].

$$S_x(\overline{\omega}) = \frac{1}{2\pi} \int_{-\infty}^{\infty} R_x(\tau) \ \exp(-i\overline{\omega}\tau) \ d\tau \tag{4.26}$$

Substituting Eq 4.23 into Eq 4.22 and then 4.22 into Eq 4.26, after doing some maths, it is possible to demonstrate that

$$S_x(\overline{\omega}) = \sum_m \sum_n \ S_{x_m x_n}(\overline{\omega}) \tag{4.27}$$

in which

$$S_{x_m x_n}(\overline{\omega}) = \phi_m \ \phi_n \ \mathbf{H}_m(-i\overline{\omega}) \ \mathbf{H}(i\overline{\omega}) \ \mathbf{S}_{p_m p_n}(\overline{\omega}) \tag{4.28}$$

is the *cross-spectral density function for modal responses* $x_m(t)$ and $x_n(t)$, $\mathbf{S}_{p_m p_n}(\overline{\omega})$ is the *cross-spectral density function* for processes $p_m(t)$ and $p_n(t)$, and

$$\mathbf{H}_m(-i\overline{\omega}) = \frac{1}{k_m^* \ [1 - 2i\xi_m(\overline{\omega}/\omega_m) - (\overline{\omega}/\omega_m)^2]} \tag{4.29}$$

$$\mathbf{H}_n(i\overline{\omega}) = \frac{1}{k_n^* \ [1 + 2i\xi_n(\overline{\omega}/\omega_n) - (\overline{\omega}/\omega_n)^2]} \tag{4.30}$$

Again, for lightly damped systems with well-separated modal frequencies Eq 4.27 can be approximated by

$$S_x(\overline{\omega}) \doteq \sum_m \ S_{x_m x_m}(\overline{\omega}) \tag{4.31}$$

[8]Instead of complete-quadratic-combination (CQC) method.

where

$$S_{x_m x_m}(\overline{\omega}) = \phi_m^2 \left|\mathbf{H}_m(i\overline{\omega})\right|^2 \; S_{p_m p_m}(\overline{\omega}) \tag{4.32}$$

$$\left|\mathbf{H}_m(i\overline{\omega})\right|^2 = \frac{1}{k_n^{*2}\left[1 + (4\xi_m^2 - 2)(\overline{\omega}/\omega)^2 + (\overline{\omega}/\omega)^4\right]} \tag{4.33}$$

and $\mathbf{S}_{p_m p_n}(\overline{\omega})$ is the Power Spectral Density Function for process $p_m(t)$.

4.2 FFT vs. B&R (Background and Resonant) responses: numerical comparison

This section is aimed at presenting results which were obtained by performing numerical analysis on some selected samples[9] (from the Database) under different wind configurations.

In previous Section it has been shown the relationship between the PSDs of input and output signal, which was given by Eq 4.19.

However, there exist a strict correlation between the frequency content of the loading and the intrinsic characteristics of the structural system, particularly in the name of its natural modal frequencies.

That is, the more the forcing frequency is close to the natural modal frequency, the higher the modal response will be. This is because loading and response get in phase, and if structure is not damped (i.e. energy dissipation), response would increase tending to infinity with elapsing of time (resonant response, see Fig 2.3).

This is at the base of the B&R decomposition of the response. The idea is that response is mainly expressed by the Background component, which highlights the quasi-static response of the structure, expressed as

$$q_B(t) = \frac{p^*(t)}{k^*} \tag{4.34}$$

or in the frequency domain

$$Q_B(\overline{\omega}) = \frac{P^*(\overline{\omega})}{k^*} \tag{4.35}$$

that in terms of Power Spectral Density function, recalling the relationship that exists between PSDs of input and output signal, gets

[9] The most relevant ones.

$$S_q^B(\overline{\omega}) = \frac{S_{p^*}(\overline{\omega})}{k^{*2}} \tag{4.36}$$

and the Resonant component, given by

$$S_q^R(\overline{\omega}) = \mathbf{H}(i\overline{\omega})\ \mathbf{H}(-i\overline{\omega})\ S_{P^*}(\omega_0) \tag{4.37}$$

where this case $S_{P^*}(\omega_0)$ is the Power Spectral Density of $P^*(\overline{\omega})$ computed at the natural modal frequency ω_0.

Hence finally, the actual PSD of the response which is analytically given by Eq 4.19 can be approximated by the sum the two components, that is

$$S_q^{BR}(\overline{\omega}) = S_q^B(\overline{\omega}) + S_q^R(\overline{\omega}) \tag{4.38}$$

They will be presented result for two main configurations, namely T115 0° attack angle and T115 45° attack angle.

In Appendix A results for other relevant cases can be found.

4.2.1 Sample T115, 0° attack angle

As said in previous Section, the objective of the Background and Resonant decomposition of the response is that of characterising the latter having info only on the loading function, thus avoiding the classical Fourier Analysis.

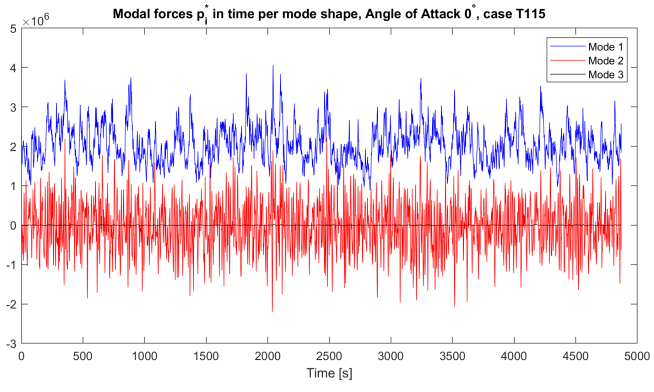

Figure 4.3: Plot of time history of Modal Forces, sample T115, 0° attack angle.

Hence, the most important quantity is the input signal, namely the time history of the modal forces, discussed in Section 3.2.4. We therefore recall their plot for sake of clarity in Fig 4.3.

The first step of the B&R analysis is then that of computing the Power Spectral Density Function of the modal forces with respect to frequencies.

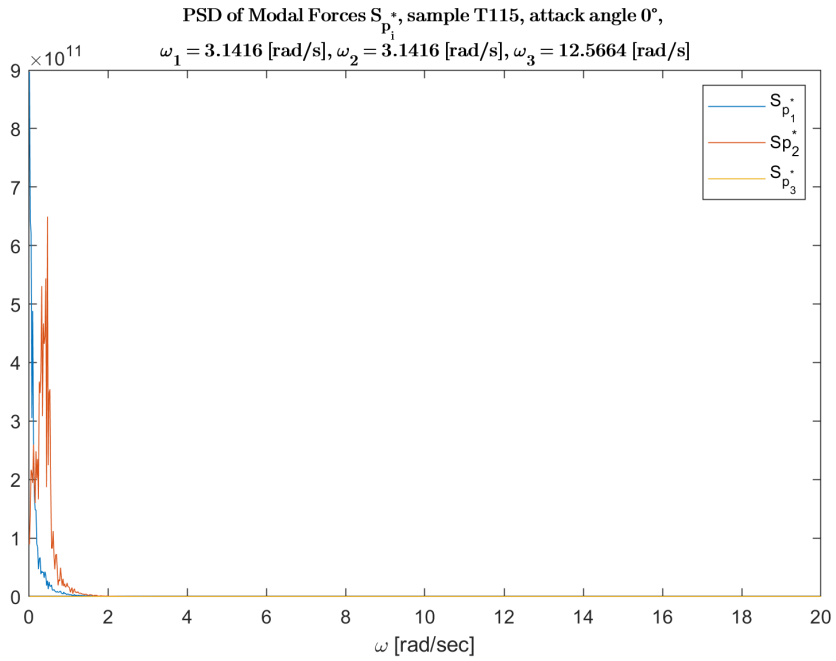

Figure 4.4: Plot of PSD of Modal Forces, sample T115, 0° attack angle.

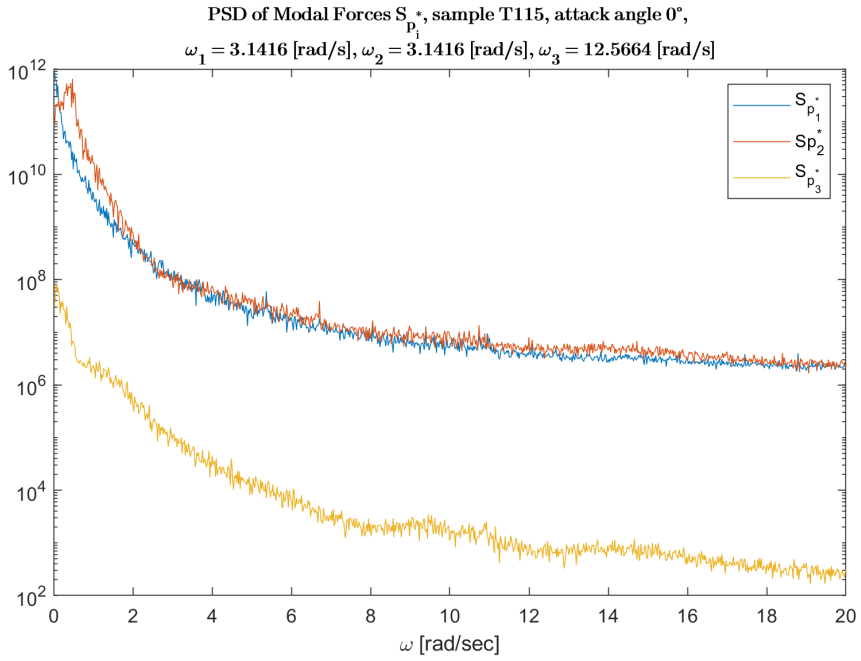

Figure 4.5: Plot of PSD of Modal Forces, sample T115, 0° attack angle (log scale).

Then, following the plots of the PSDs modal amplitudes and an arbitrary monitoring displacement (Up-Right element of Windward surface in this case) from Fourier Analysis:

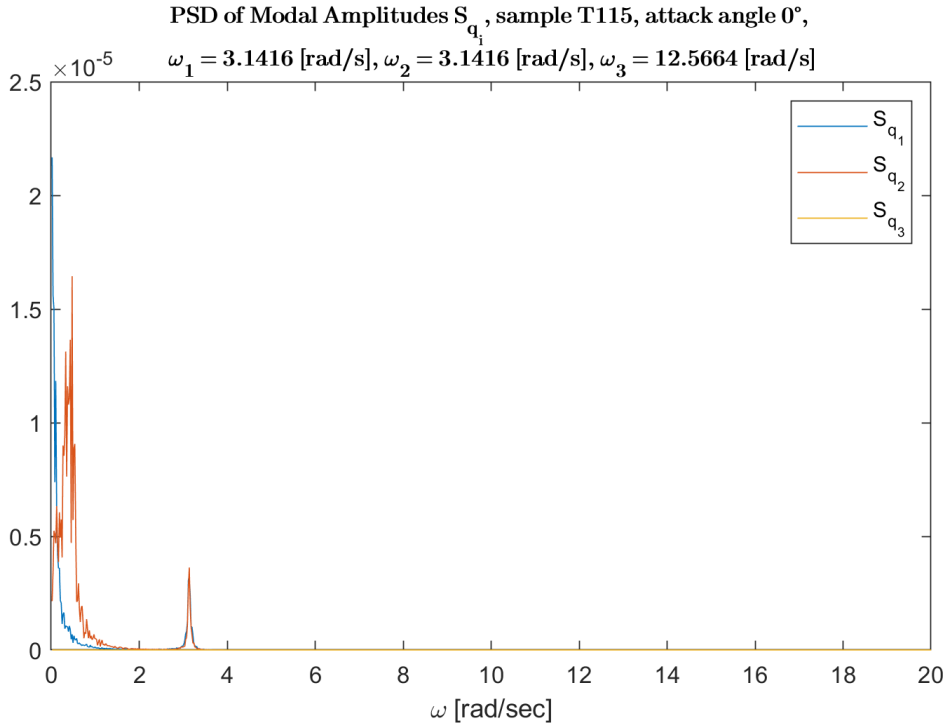

Figure 4.6: Plot of PSD of Modal Amplitudes, sample T115, 0° attack angle.

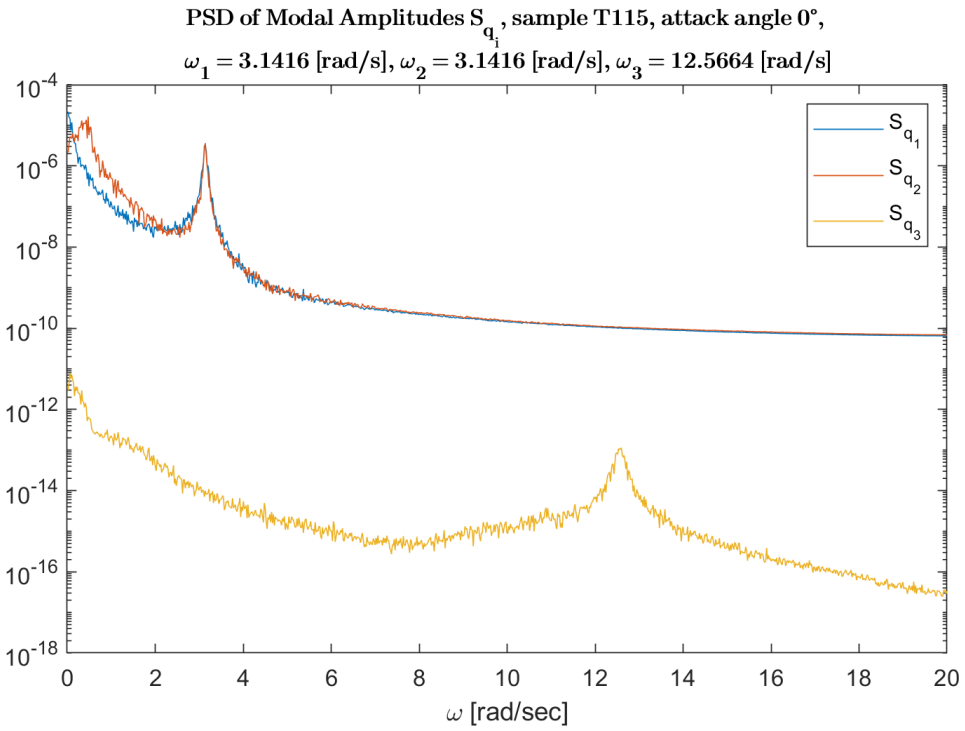

Figure 4.7: Plot of PSD of Modal Amplitudes, sample T115, 0° attack angle (log scale).

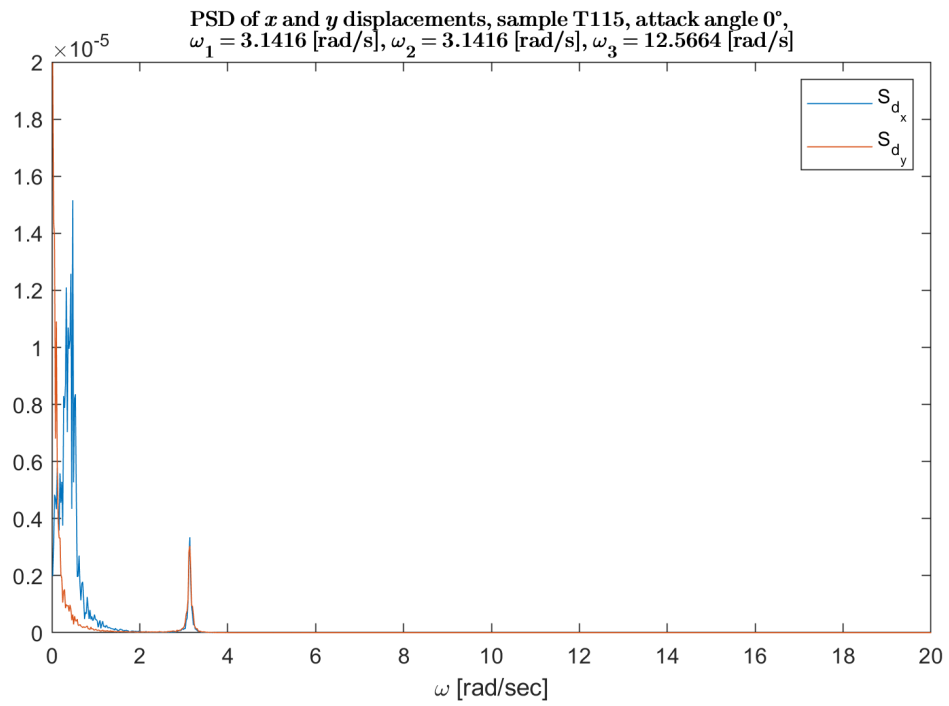

Figure 4.8: Plot of PSD of x and y displacements of UL elements on W surface, sample T115, 0° attack angle.

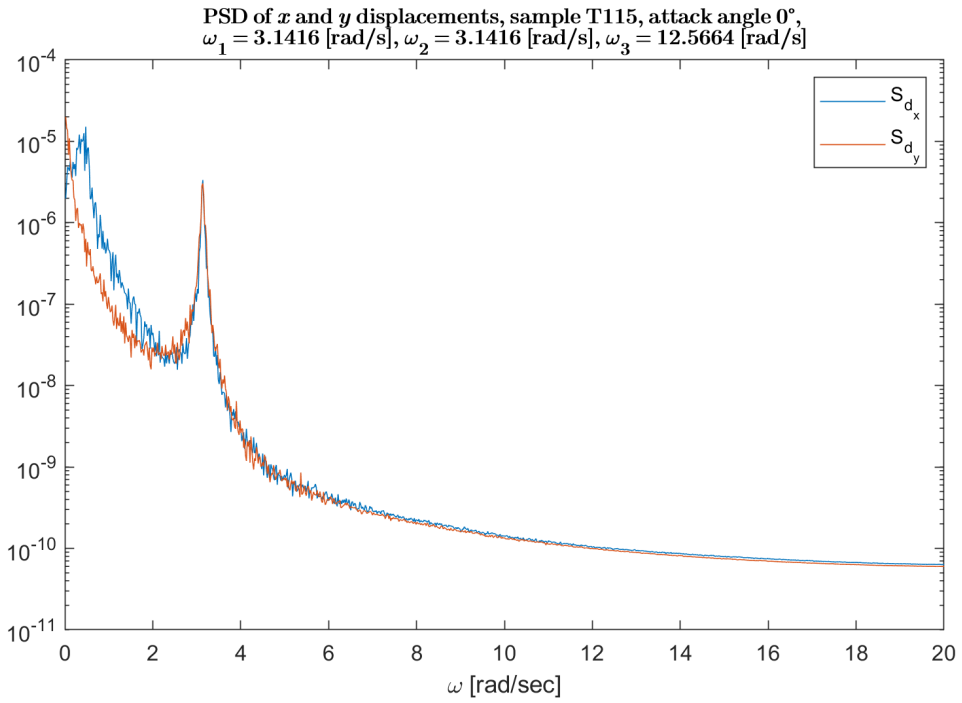

Figure 4.9: Plot of PSD of x and y displacements of UL element on W surface, sample T115, 0° attack angle (log scale).

Finally, the plots which show the comparison between PSDs of modal amplitudes computed with classical Fourier Analysis and the Background and Resonant B&R decomposition of the response.

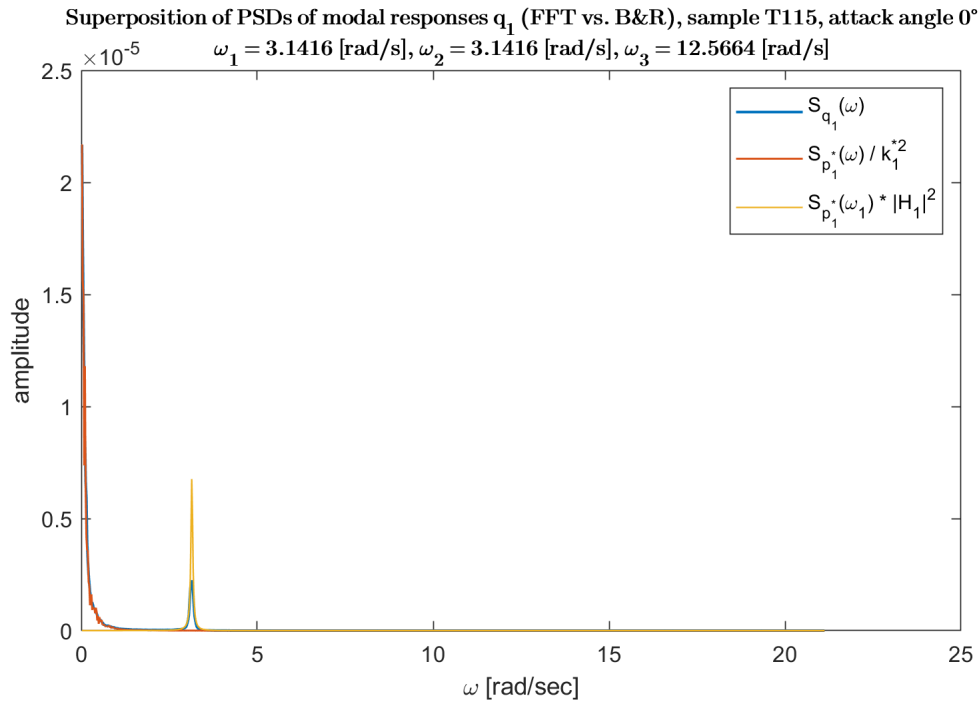

Figure 4.10: Superposition of FFT and B&R modal responses for Mode 1, sample T115, 0° attack angle.

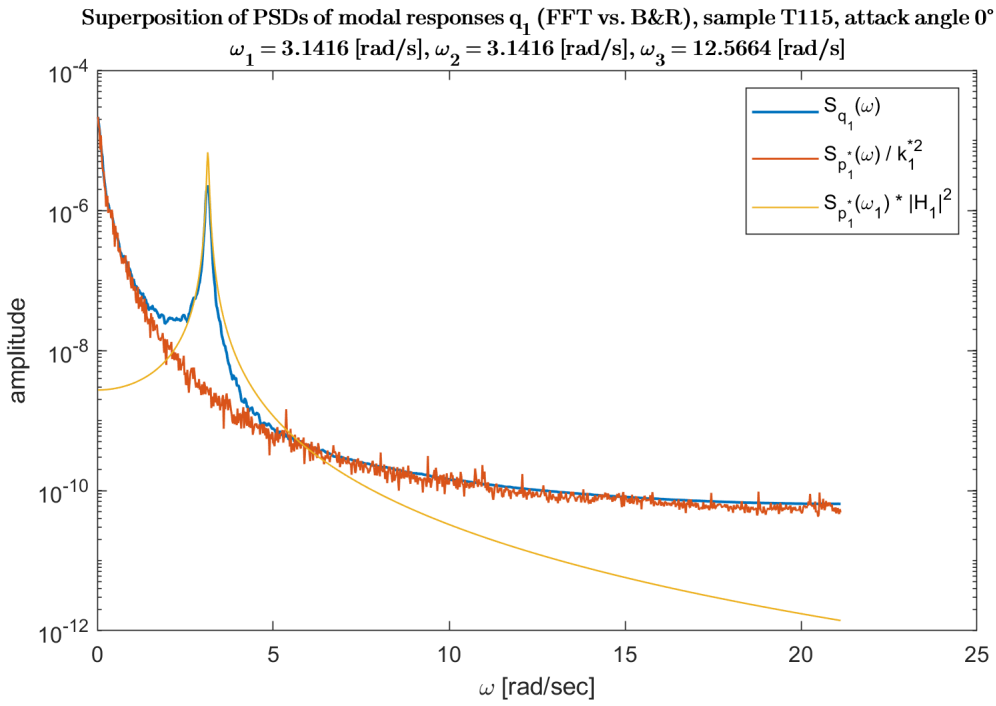

Figure 4.11: Superposition of FFT and B&R modal responses for Mode 1, sample T115, 0° attack angle (log scale).

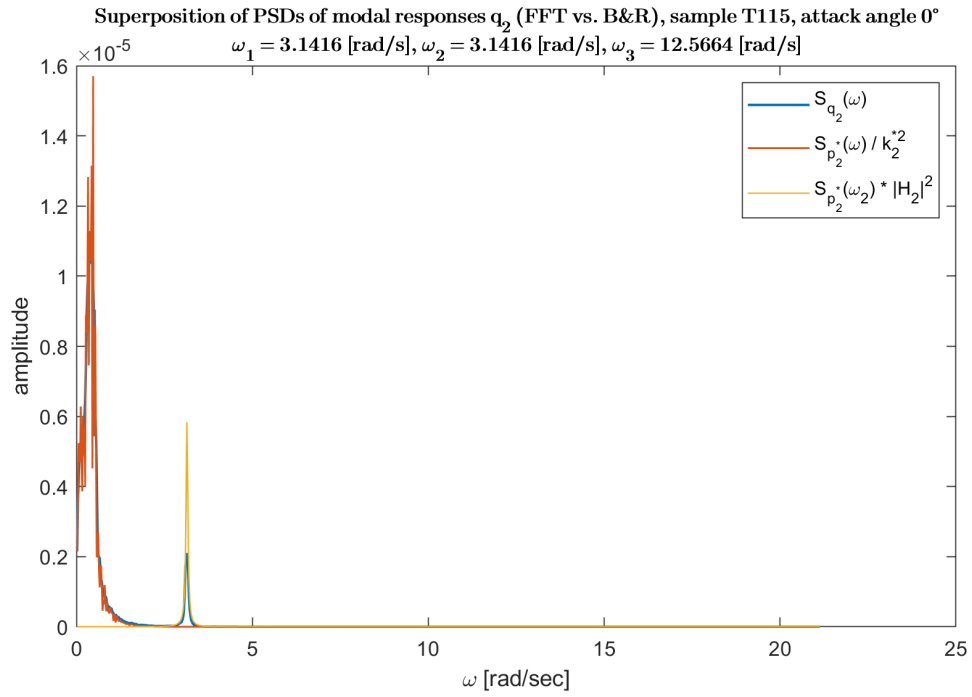

Figure 4.12: Superposition of FFT and B&R modal responses for Mode 2, sample T115, 0° attack angle.

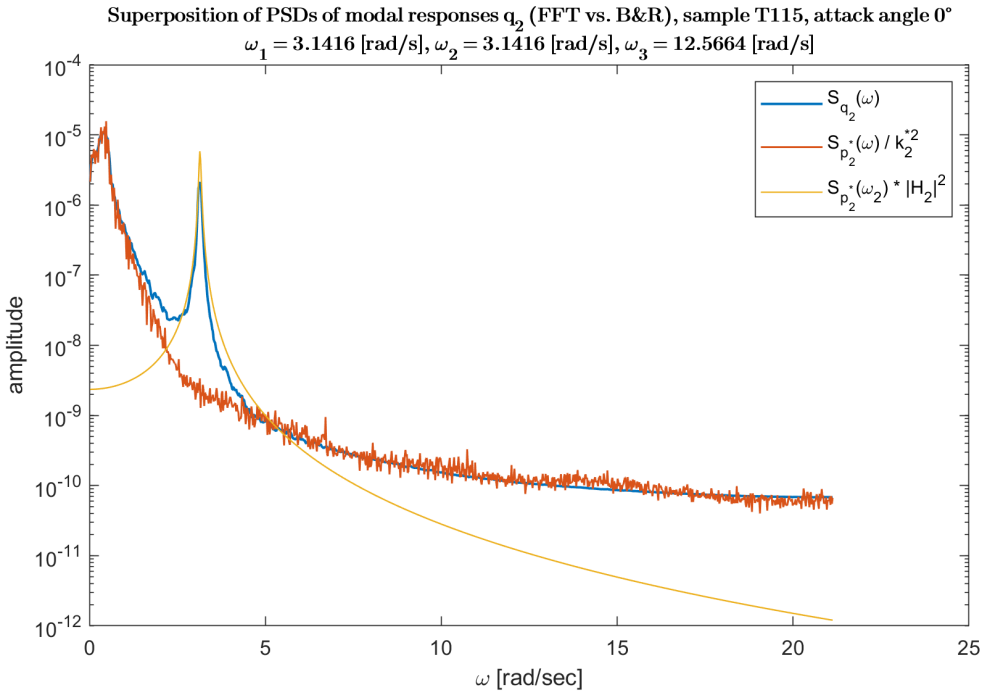

Figure 4.13: Superposition of FFT and B&R modal responses for Mode 2, sample T115, 0° attack angle (log scale).

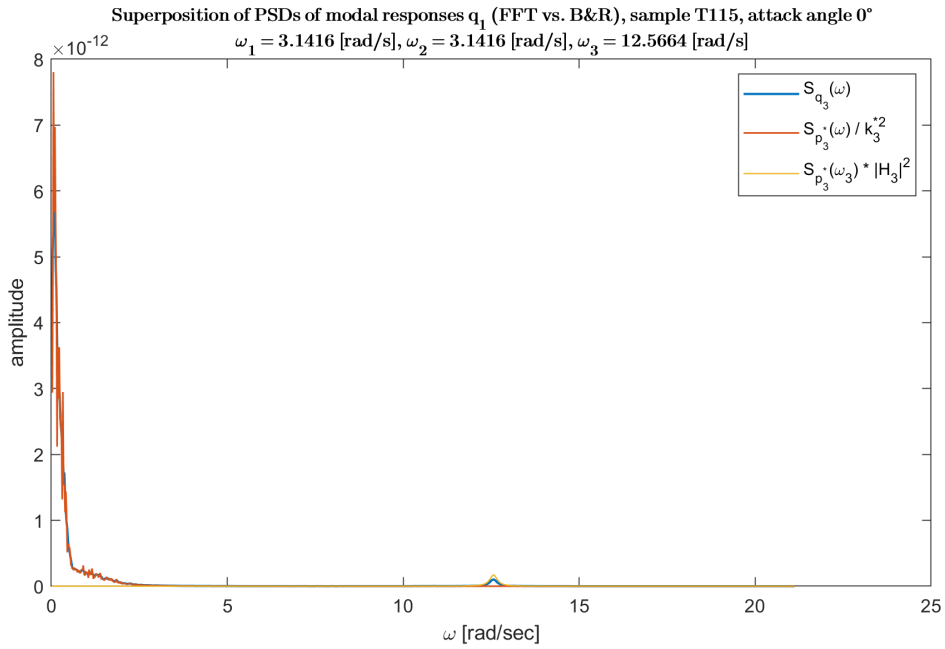

Figure 4.14: Superposition of FFT and B&R modal responses for Mode 3, sample T115, 0° attack angle.

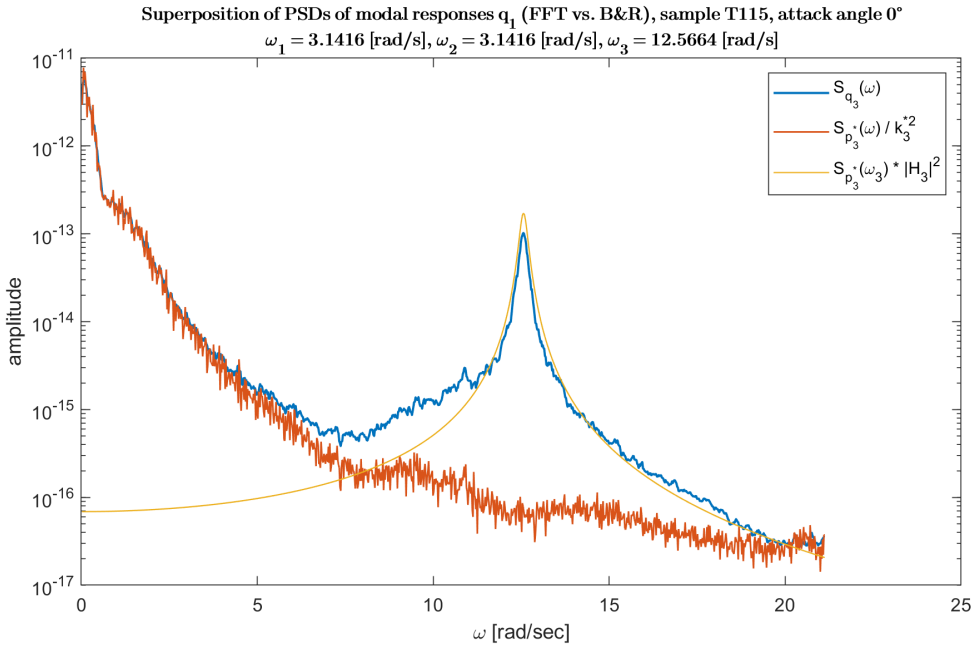

Figure 4.15: Superposition of FFT and B&R modal responses for Mode 3, sample T115, 0° attack angle (log scale).

It can be clearly seen that two methods match quite well. Modal Response is well reproduced by the B&R decomposition.

One could argue that, looking at Figs 4.10 4.12 and 4.14, the resonant component (coloured in yellow) has an higher peak with respect to the one coming from the Fourier Analysis (blue line). However, this is only due to local approximation. In Eq 4.36 it has been shown how the resonant component is computed: it depends on the value of the power spectral density function of the modal force at the natural modal frequency $S_{P^*}(\omega_0)$. Therefore, a change in its value would produce a change in the final values of the resonant component. Clearly, the plot of the PSD of the modal forces in Fig 4.4 (4.5 in log scale) are not smoothed; in 4.16 a zoom can be appreciated. This is the source of the not exact computation of $S_{P^*}(\omega_0)$; however, variability is low enough such to produce negligible relative errors.

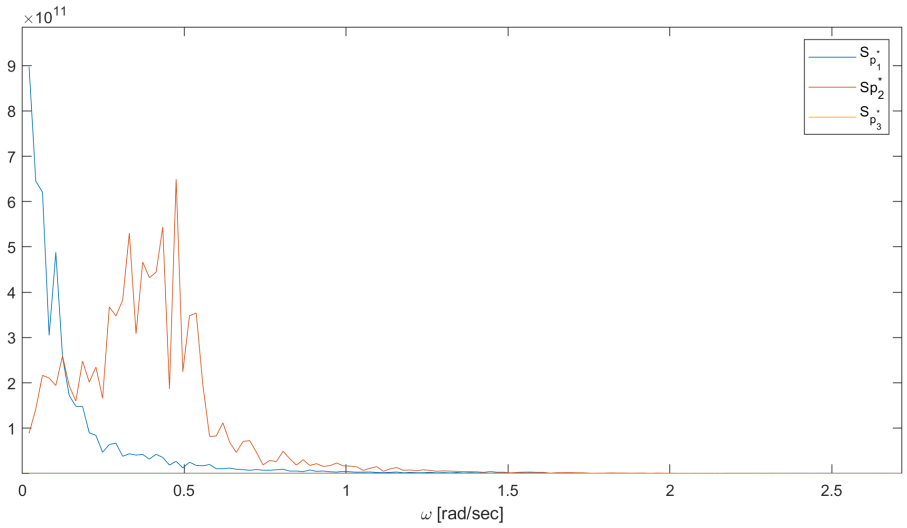

Figure 4.16: Zoom on the graph of modal amplitudes, sample T115, 0° attack angle.

4.2.2 Sample T115, 45° attack angle

This section, additionally to present results on B&R decomposition applied to this configuration, has also, and more importantly the purpose of showing that it is valid independently to any possible influencing parameter, such among the most important the natural modal frequencies.

Hence, in analysing this configuration, modal frequencies will be varied with respect to previous case, in which they were equal to

$$\omega_1 = 0.5\ Hz$$

$$\omega_2 = 0.5\ Hz$$

$$\omega_3 = 2\ Hz$$

.

In this case, we will set them, arbitrarily, to $0.1\ Hz$, $0.2\ Hz$[10] and $1\ Hz$.

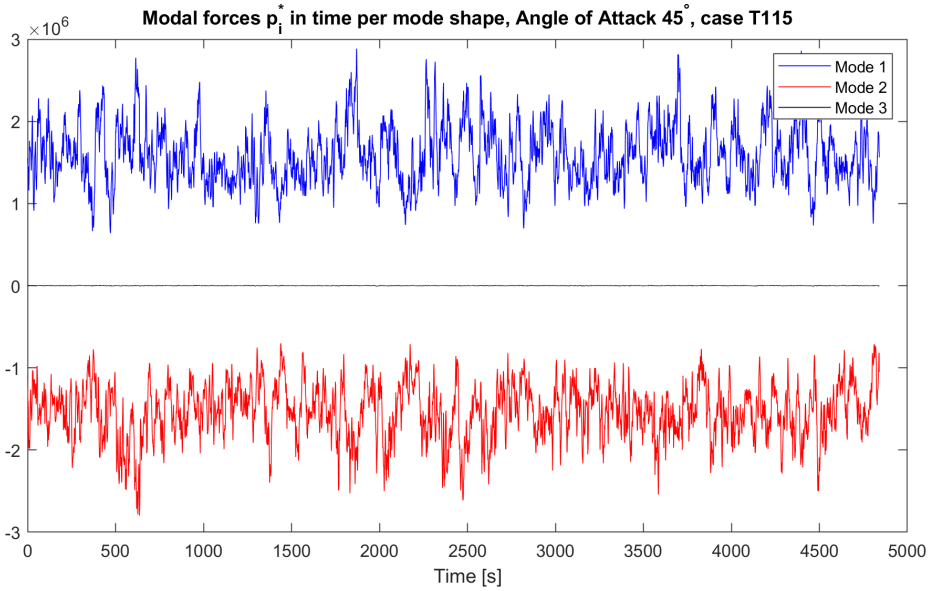

Figure 4.17: Plot of time history of Modal Forces, sample T115, 45° attack angle.

[10]In reality, considering the symmetry of the structure, mode 1 and mode 2 should have same natural modal frequency since they are basically defined the same. However, this differentiation is only with the scope of showing the consistency of the method with respect to natural modal frequencies.

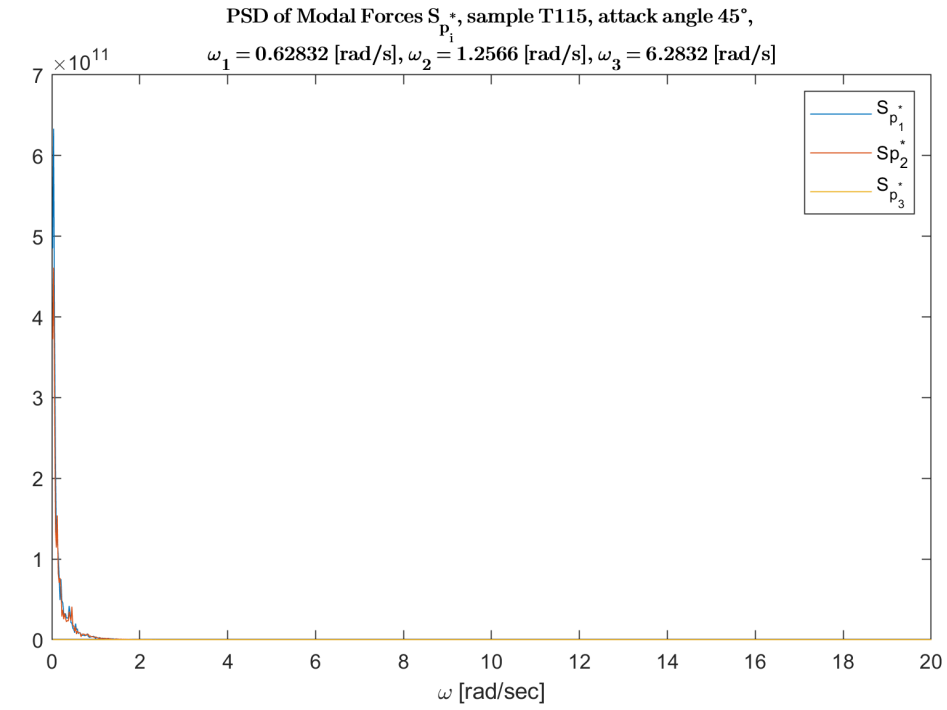

Figure 4.18: Plot of PSD of Modal Forces, sample T115, 45° attack angle.

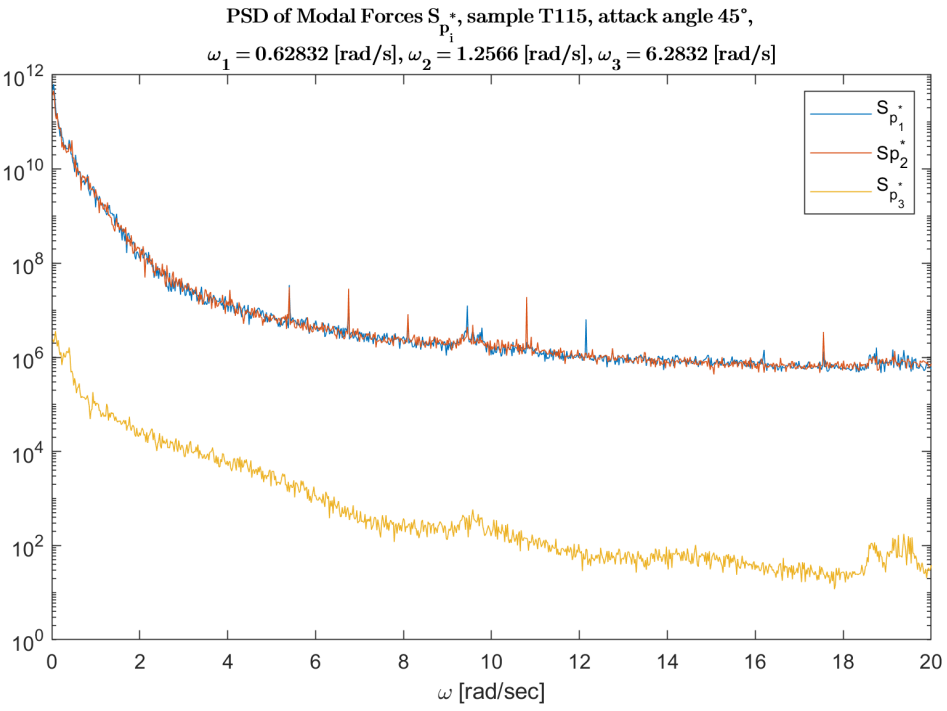

Figure 4.19: Plot of PSD of Modal Forces, sample T115, 45° attack angle (log scale).

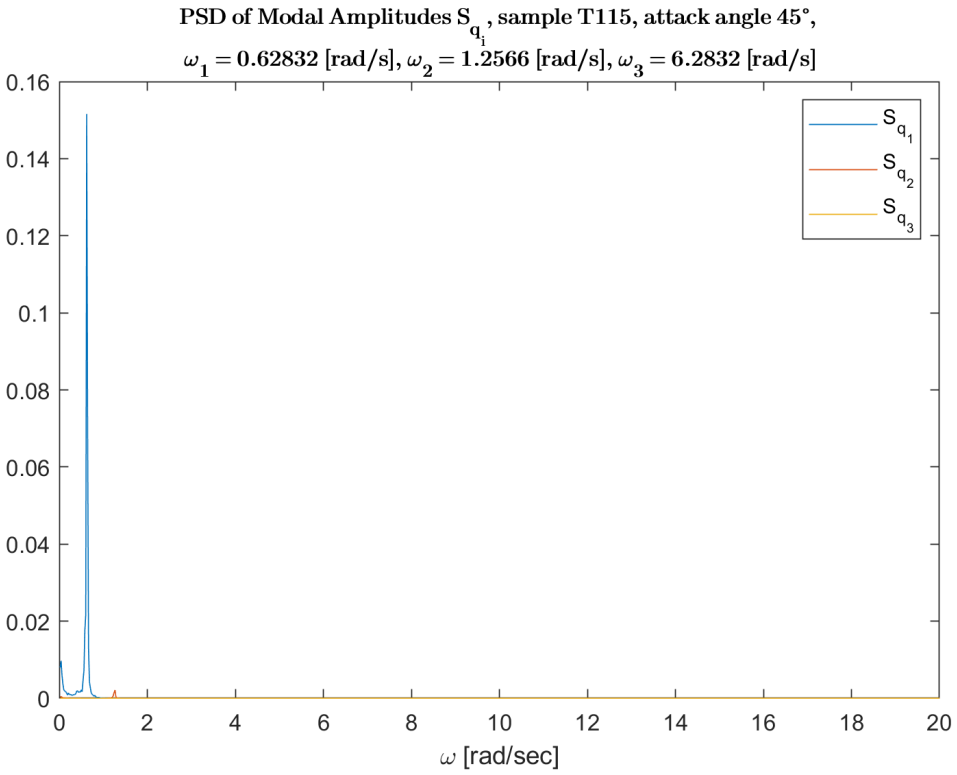

Figure 4.20: Plot of PSD of Modal Amplitudes, sample T115, 45° attack angle.

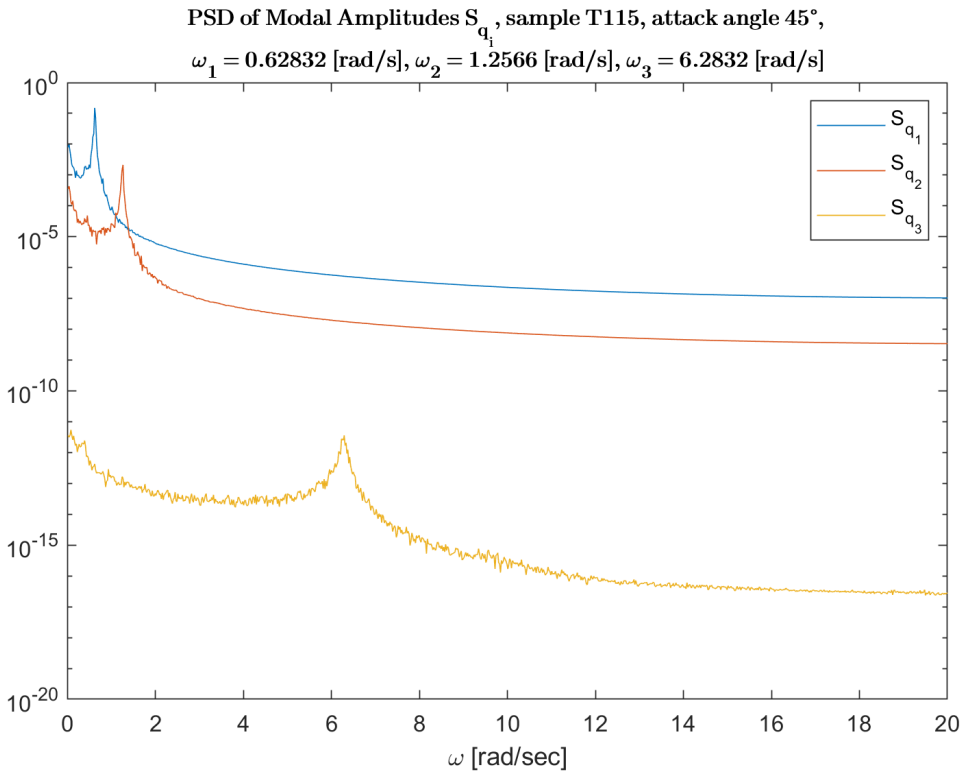

Figure 4.21: Plot of PSD of Modal Amplitudes, sample T115, 45° attack angle (log scale).

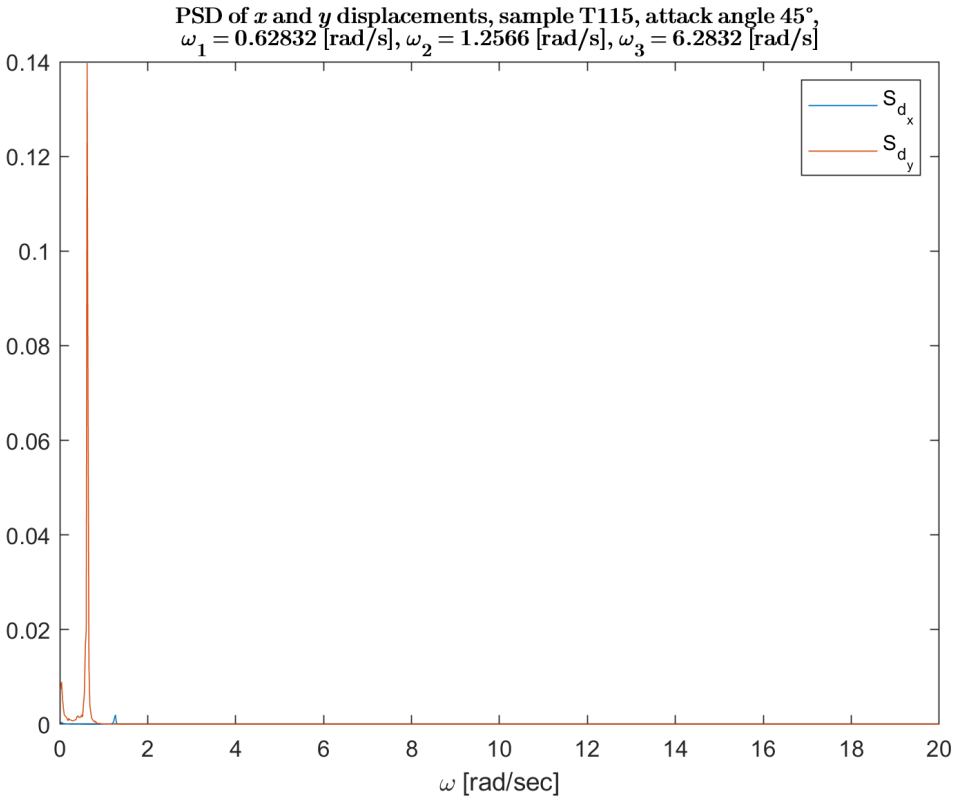

Figure 4.22: Plot of PSD of x and y displacements of UL element on W surface, sample T115, 45° attack angle.

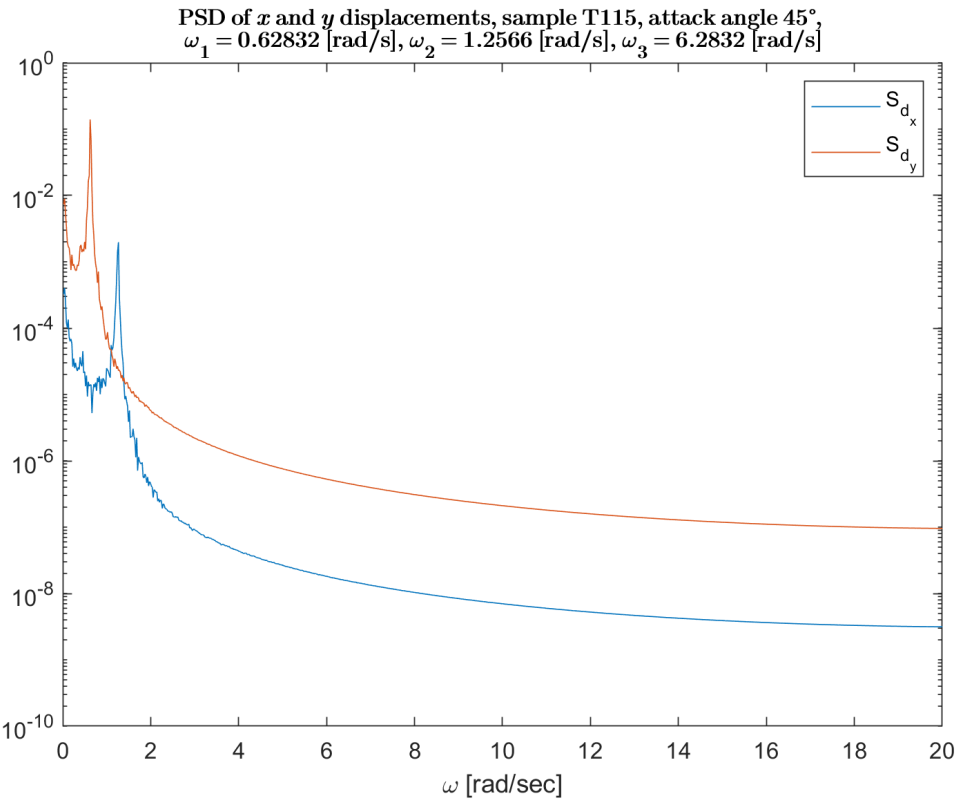

Figure 4.23: Plot of PSD of x and y displacements of UL elements on W surface, sample T115, 45° attack angle (log scale).

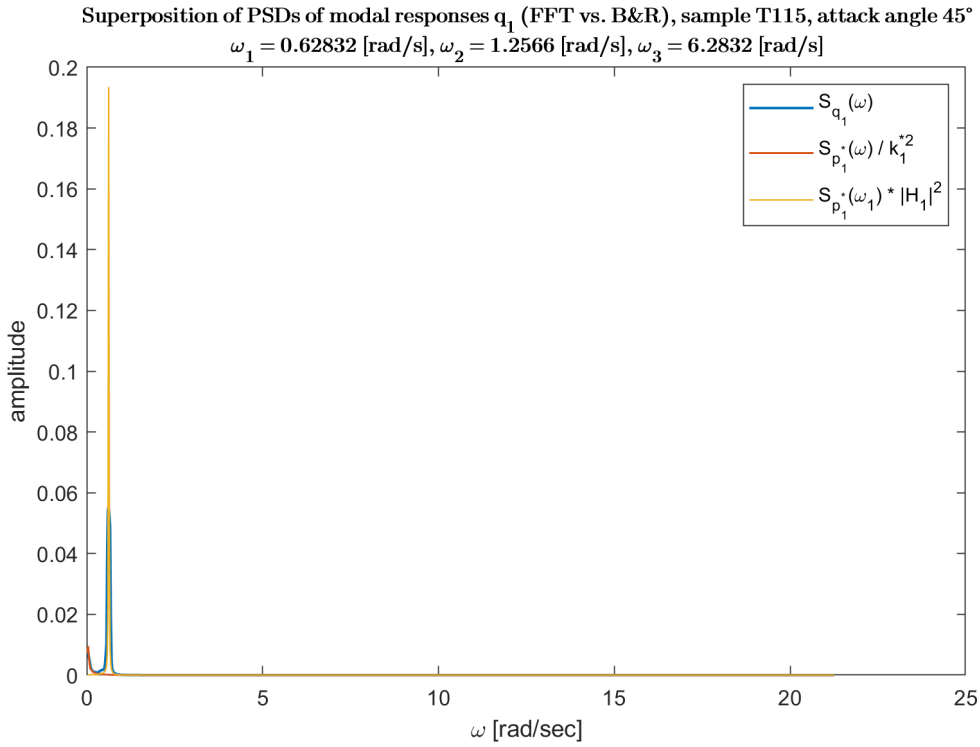

Figure 4.24: Superposition of FFT and B&R modal responses for Mode 1, sample T115, 45° attack angle.

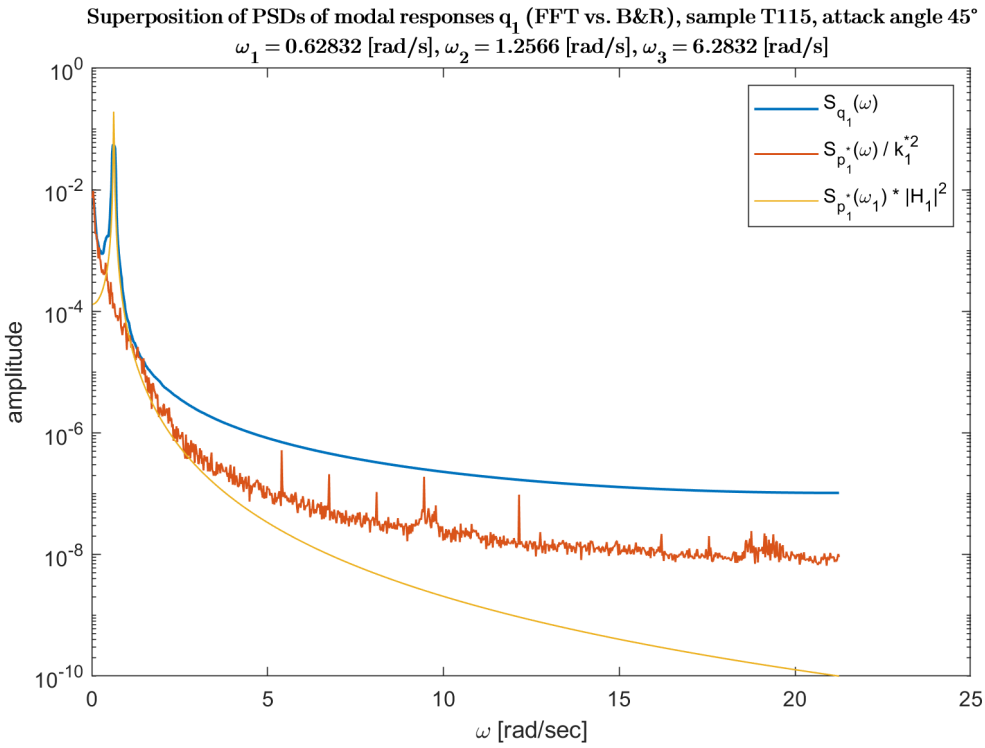

Figure 4.25: Superposition of FFT and B&R modal responses for Mode 1, sample T115, 45° attack angle (log scale).

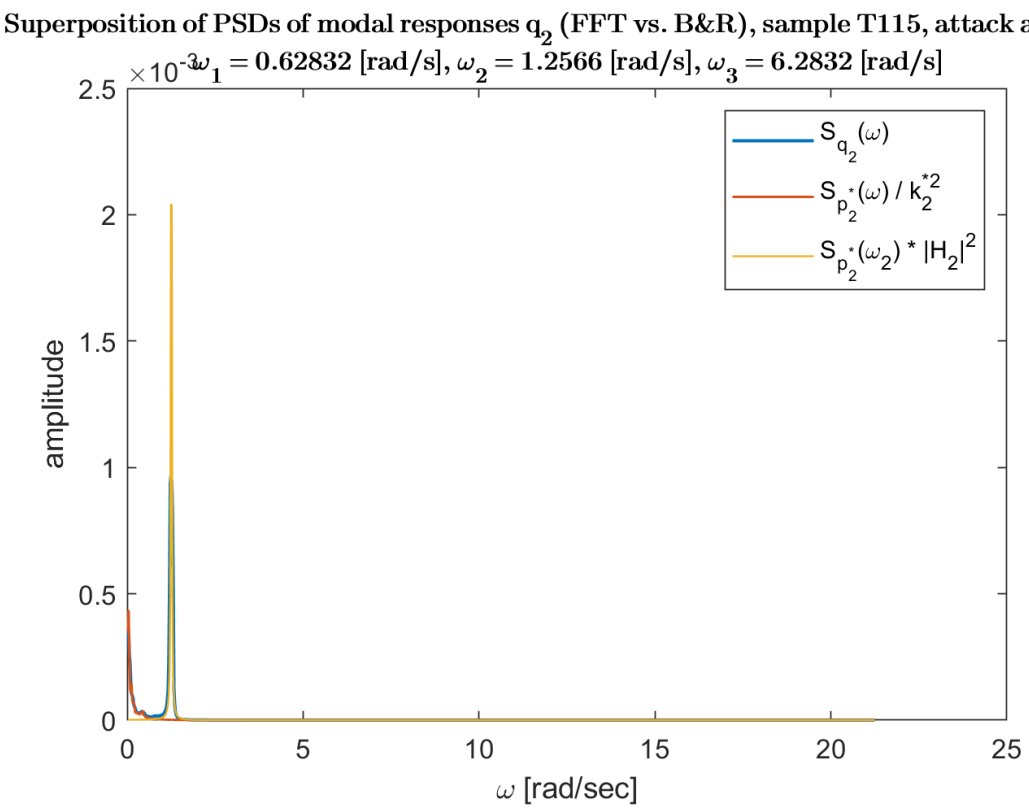

Figure 4.26: Superposition of FFT and B&R modal responses for Mode 2, sample T115, 45° attack angle.

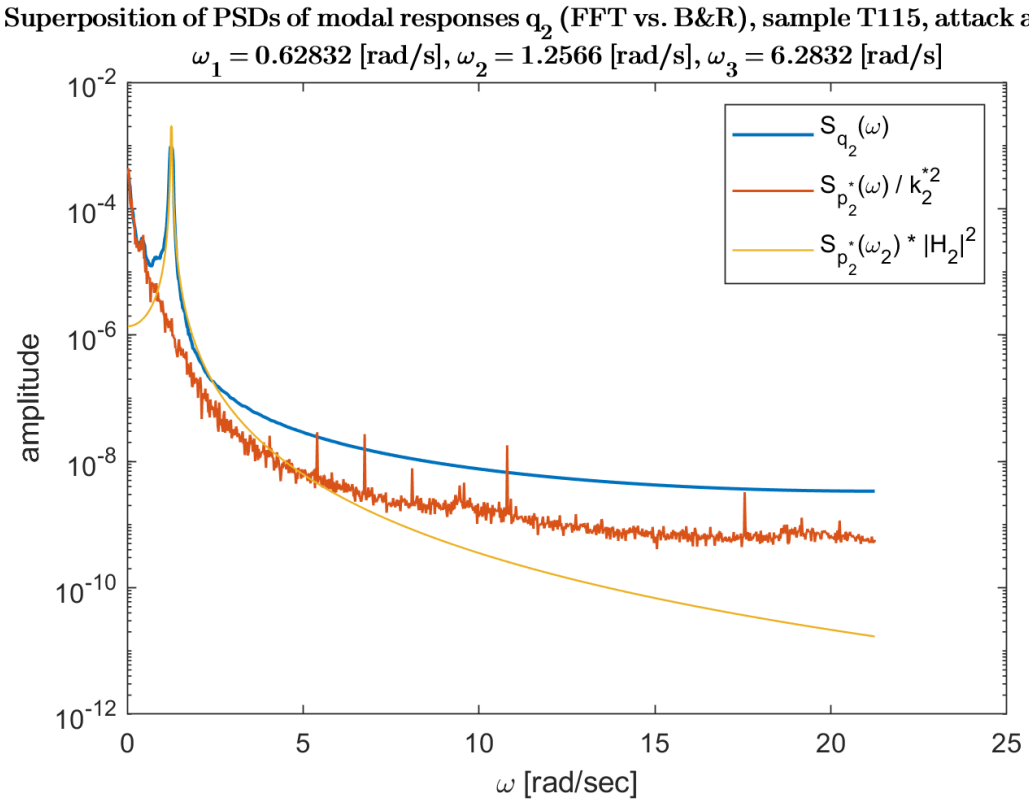

Figure 4.27: Superposition of FFT and B&R modal responses for Mode 2, sample T115, 45° attack angle (log scale).

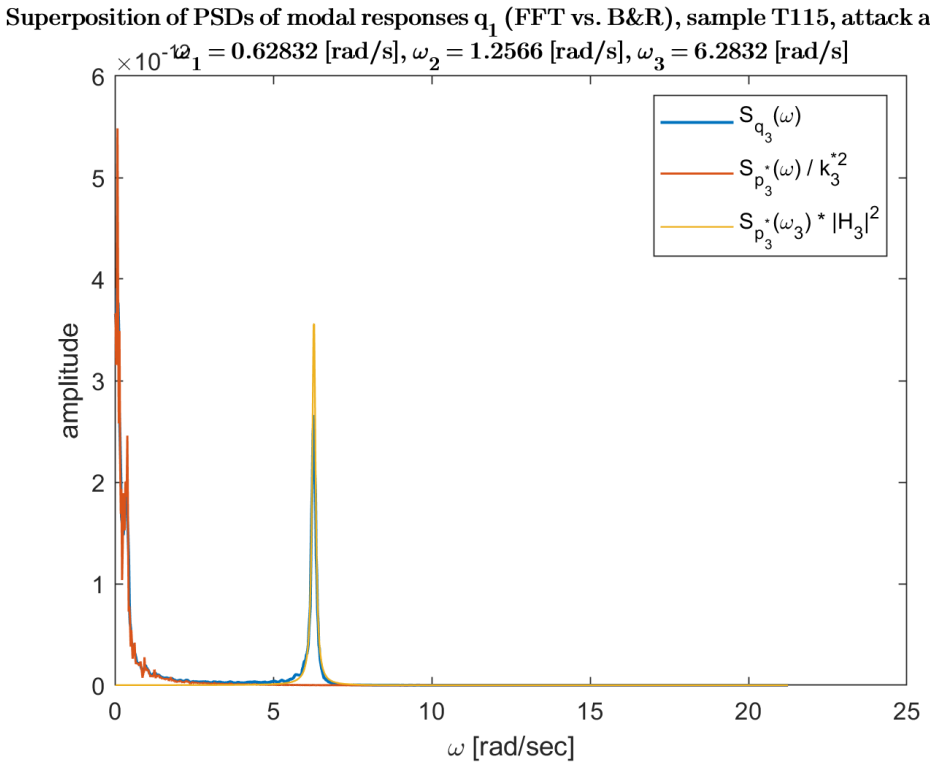

Figure 4.28: Superposition of FFT and B&R modal responses for Mode 3, sample T115, 45° attack angle.

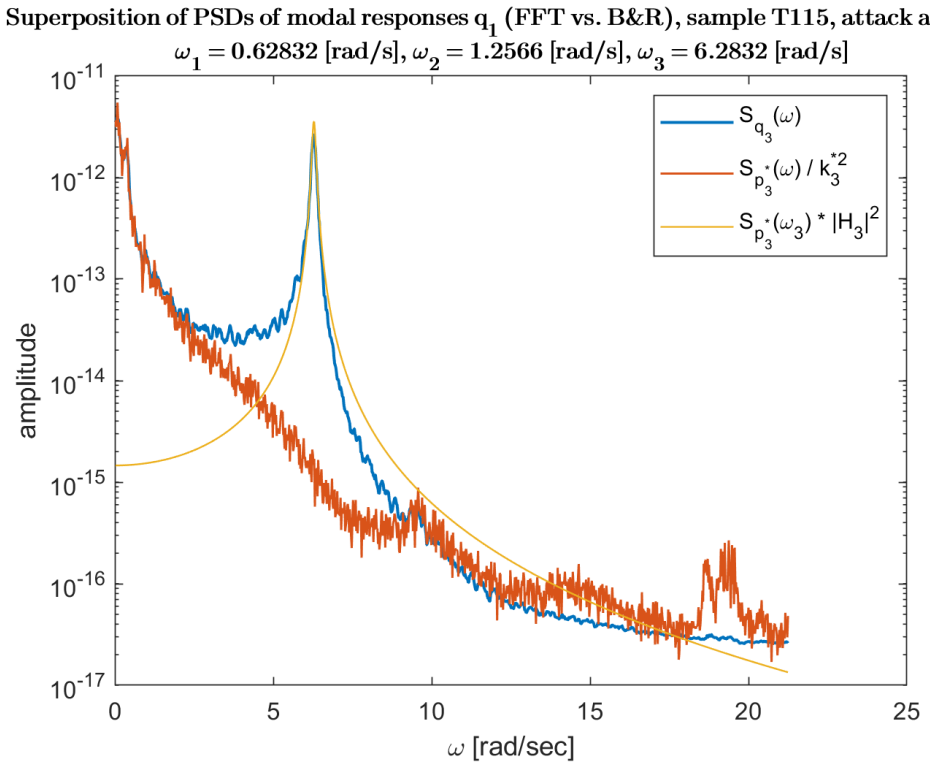

Figure 4.29: Superposition of FFT and B&R modal responses for Mode 3, sample T115, 45° attack angle (log scale).

4.3 Validation: integration in the frequency domain

This section is an extension of the previous two ones, in which we have demonstrated as the B&R decomposition of the response well reproduced the actual behaviour of the modal responses got from classical Fourier Analysis.

Still, those two examples cannot be taken as general validation of the method, since they rely on two set of fixed values of natural modal frequencies.

Therefore, a general and definitive validation will be performed, by letting the first two natural modal frequencies (keeping the third fixed, as it is of minor interest in this case) varying in a range from $0.05\ Hz$ to $2\ Hz$. Just to mention that, in reality these are very low natural frequencies (normal civil structures have as for the first mode a natural frequency of 1 Hz, then higher modes have higher frequencies, which means lower periods): still, it has been chosen this range so to empathise resonant response, since generally the frequency content of the input signal (i.e. the dynamic wind loading) is characterised by high content in the very low range of frequencies, which means high periods. Figures 4.30 and 4.31 clearly shows this statement.

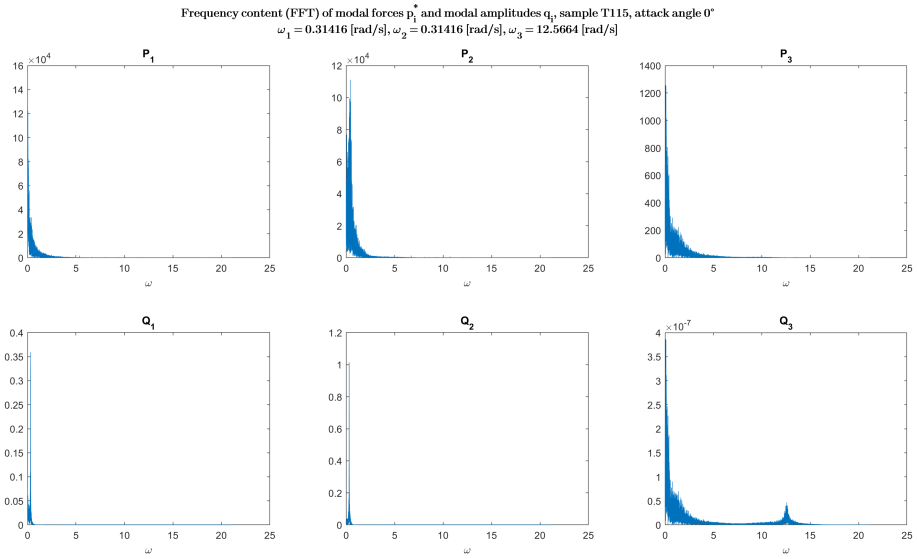

Figure 4.30: Low natural modal frequencies, amplification of resonance response.

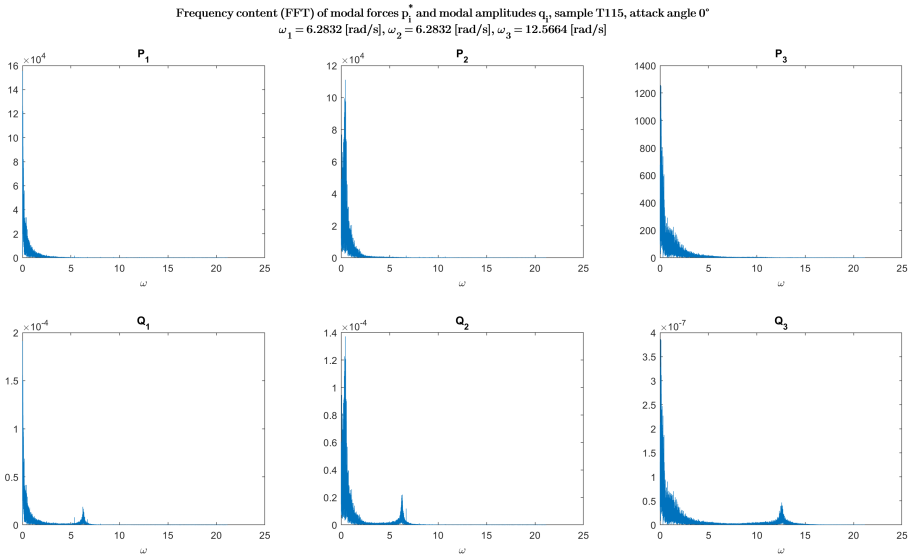

Figure 4.31: High natural modal frequencies, tendency to quasi-static response.

Clearly, looking at the bottom graphs, depicting the modal response in the frequency domain, amplitudes are way higher in values in the first case (resonance) with respect to the second one (quasi-static).

That being said, we will now report the results of the validation. As stated in the title of this section, it will be done in terms of integrating in the frequency domain. For this purpose, we briefly recall Eq 4.17, in which it was shown how the integral of the power spectral density function in the frequency domain was equal to the variance of the random process considered.

This means that, integrating the PSD functions introduced in previous section in the frequency domain, we can compute the variance of the modal responses from the B&R decomposition as

$$\sigma_q^{2^{BR}} = m_{2,q,BR} = \int_{-\infty}^{\infty} S_q^{BR}(\overline{\omega})\, d\overline{\omega} \tag{4.39}$$

which split in the two components becomes

$$\begin{aligned} m_{2,q,BR} &= \int_{-\infty}^{\infty} \left(S_q^B(\overline{\omega}) + S_q^R(\overline{\omega})\right)\, d\overline{\omega} = \int_{-\infty}^{\infty} S_q^B(\overline{\omega})\, d\overline{\omega} + \int_{-\infty}^{\infty} S_q^R(\overline{\omega})\, d\overline{\omega} \\ &= m_{2,q,B} + m_{2,q,R} \end{aligned} \tag{4.40}$$

in which $m_{2,q,B}$ is the *second central moment* (i.e. variance) of the background component of the response

$$m_{2,q,B} = \frac{m_{2,p^*}}{k^{*2}} \tag{4.41}$$

and $m_{2,q,R}$ is the second central moment of the resonant component

$$m_{2,q,R} = \int_{-\infty}^{\infty} S_q^R(\overline{\omega})\, d\overline{\omega} = \int_{-\infty}^{\infty} \mathbf{H}(i\overline{\omega})\, \mathbf{H}(-i\overline{\omega})\, S_{P^*}(\omega_0)\, d\overline{\omega} \tag{4.42}$$

and remembering that $S_{P^*}(\omega_0)$ is a constant, thus taken out from the integration,

$$m_{2,q,R} = S_{P^*}(\omega_0) \ * \int_{-\infty}^{\infty} \mathbf{H}(i\overline{\omega})\, \mathbf{H}(-i\overline{\omega})\, d\overline{\omega} = S_{P^*}(\omega_0) \ * \int_{-\infty}^{\infty} \left|\mathbf{H}(i\overline{\omega})\right|^2 \, d\overline{\omega}$$

$$m_{2,q,R} = \frac{\pi\omega_i}{2\xi_i k_i^{*2}}\, S_{P^*}(\omega_0) \tag{4.43}$$

On the other hand, it is possible to compute the second central moment of the modal responses computed by means of Fourier Analysis, which in MATLAB[11] can be easily done by recalling the function **var**, that is

$$m_{2,q,FFT} = \mathbf{var}(q(t))$$

.

Then, last step of validation is to compare the second central moments got from the two different approach, with varying natural modal frequencies. Following they will be reported results for the sample T115, at 0° attack angle.

[11]The sofware which has been used to write the code.

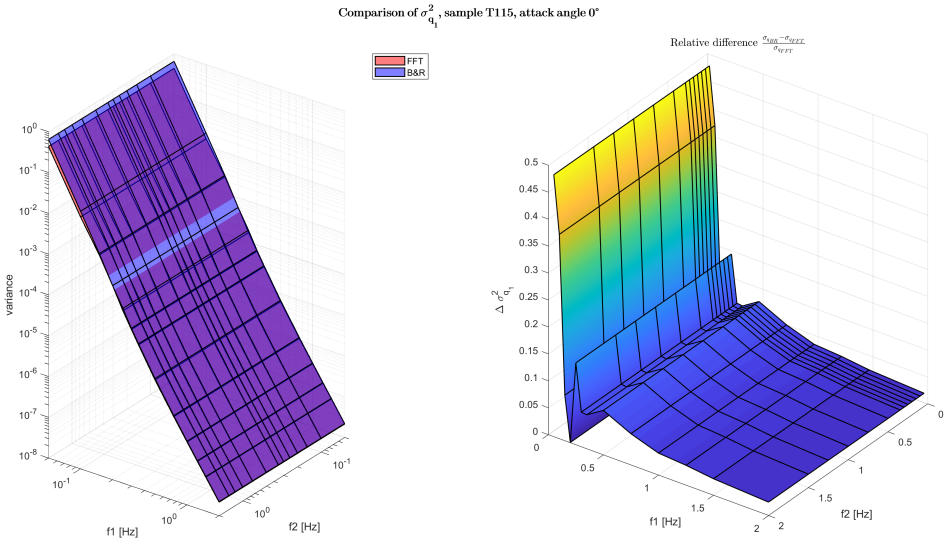

Figure 4.32: Variance of q_1 (FFT vs. B&R) in the frequency space.

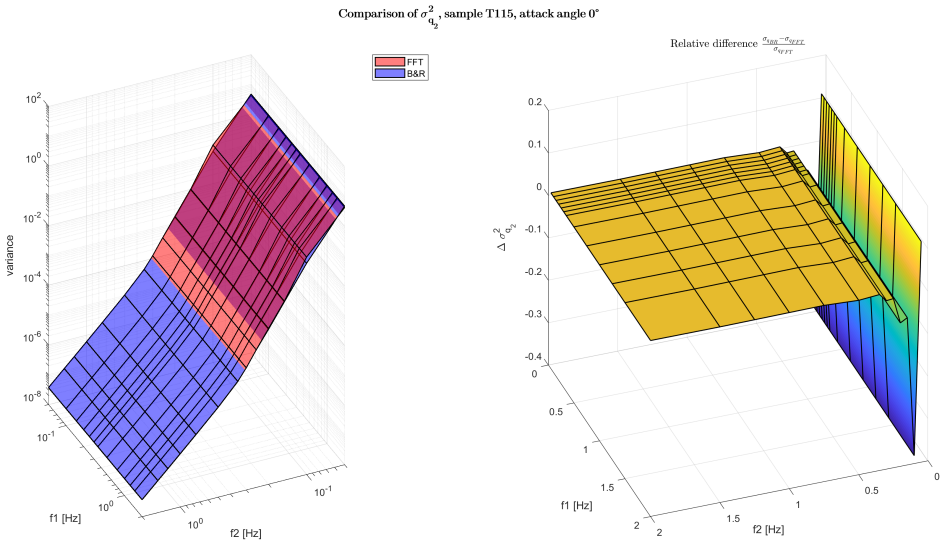

Figure 4.33: Variance of q_2 (FFT vs. B&R) in the frequency space.

As it can be noticed, either q_1 and q_2 vary only with respect to ω_1 and ω_2 respectively. This makes sense under the assumption of fully independent modal shapes, that we discussed in Section 3.2.2. On the other hand, the second central moment of q_3 referring to the third mode (fig 4.34) does not vary in the frequency space since it has been assumed a constant and fixed value[12].

Yet, in both cases, we notice that the two methods compute almost identical values of the variance when modal frequencies increases, while relative difference (sketched in the right graphs) increases with natural frequencies approaching zero, for which also variance, in both cases, increases. Of course this makes sense, since the lower the natural

[12]Because higher modes have minor effects on total response with respect to first main ones, therefore allowing skipping, in this context, the analysis with respect to variation of their natural modal frequencies.

modal frequency, the higher the possibility of occurrence of resonant effect, which makes response much more sensible and unstable (i.e. more variable with respect to mean value).

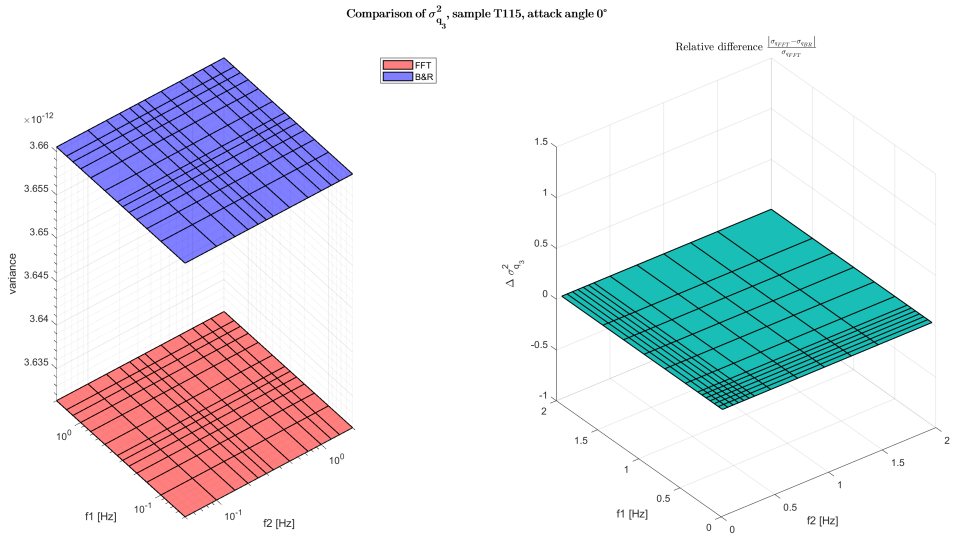

Figure 4.34: Variance of q_3 (FFT vs. B&R) in the frequency space.

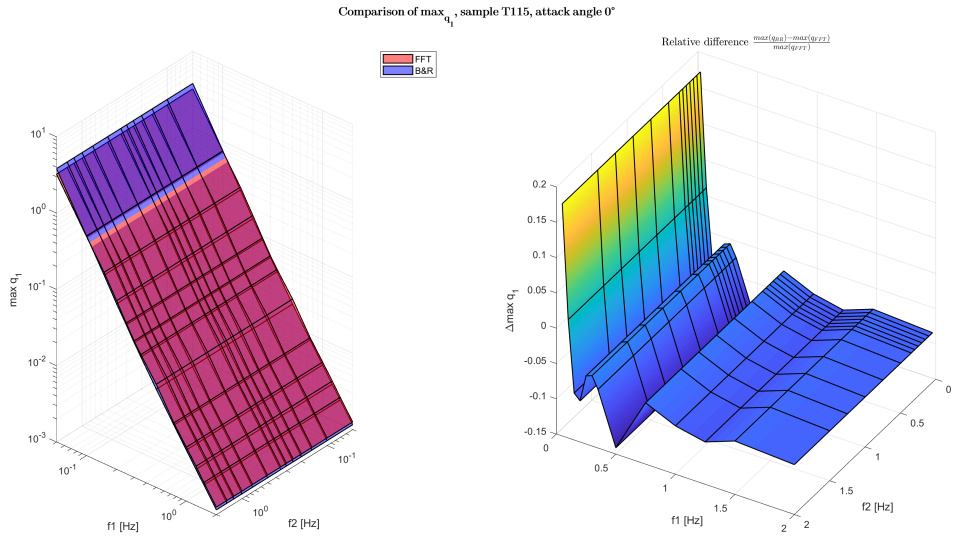

Figure 4.35: $\max(q_1)$ (FFT vs. B&R) in the frequency space.

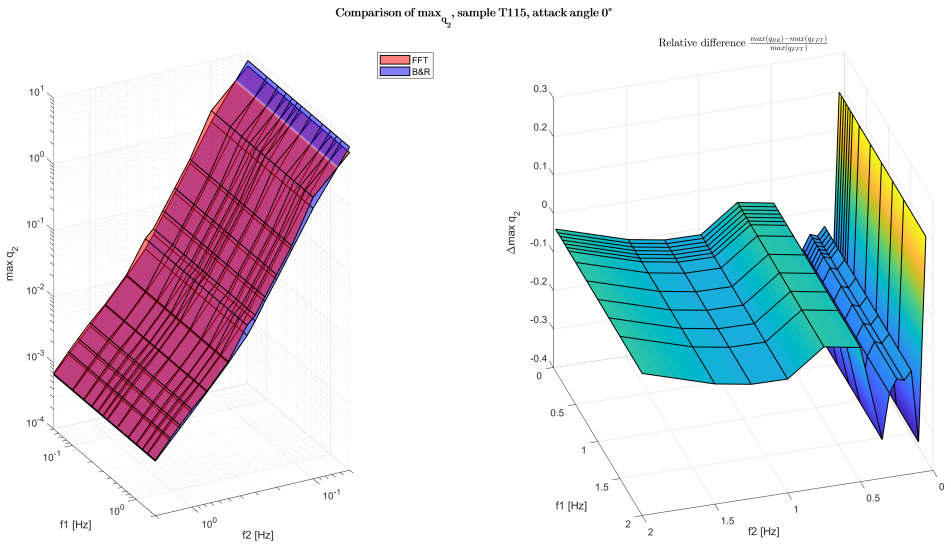

Figure 4.36: max(q_2) (FFT vs. B&R) in the frequency space.

Figures 4.35, 4.36 and 4.37 refer to the maximum values of the modal responses, and clearly they show the same trend as in Figs 4.32, 4.33 and 4.34. For the FFT method, it has been simply computed using the MATLAB function **max**, that is

$$\max_{q,FFT} = \mathbf{max}(q(t))$$

.

For the B&R decomposition, maximum value of the variance has been computed as

$$q_{i,max,BR} = \overline{q_i} + g\,\sqrt{m_{2,q_i,BR}} \tag{4.44}$$

in which $\overline{q_i}$ is the mean value of ith modal response (of B&R method), given by

$$\overline{q_i} = \frac{\overline{p_i^*}}{k_i^*} \tag{4.45}$$

$\overline{p_i^*}$ mean value of the ith modal force, k_i^* ith modal stiffness,

$$\sqrt{m_{2,q_i,BR}} = \sigma_{q_i} = \frac{1}{k_i^*}\sqrt{m_{2,p^*} + S_{p_i^*}(\omega_i)\,\frac{\pi\omega_i}{2\xi_i}} \tag{4.46}$$

is the standard deviation of the ith modal amplitude (by means of B&R method), g is defined as *peak factor*, and it generally varies between 3.5 and 4. In this case, a value of 3.5 has been selected.

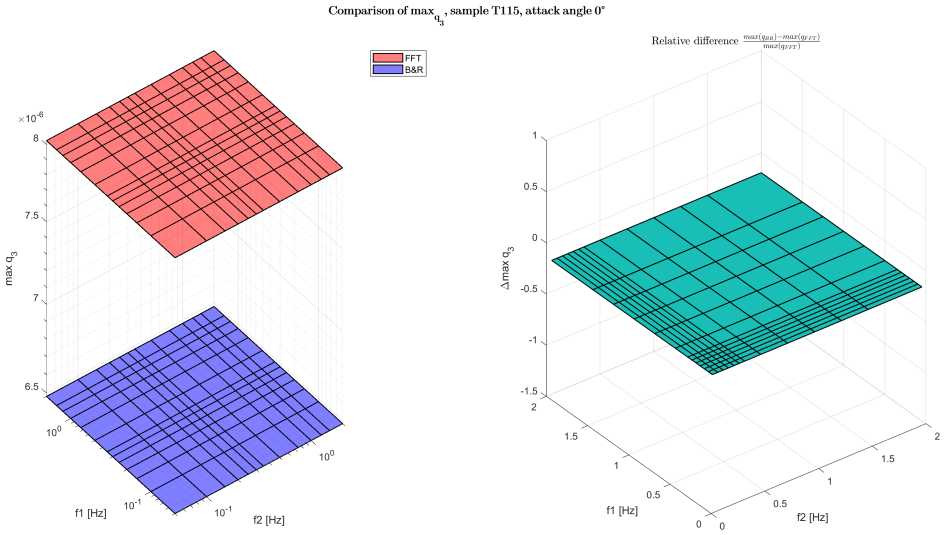

Figure 4.37: max(q_3) (FFT vs. B&R) in the frequency space.

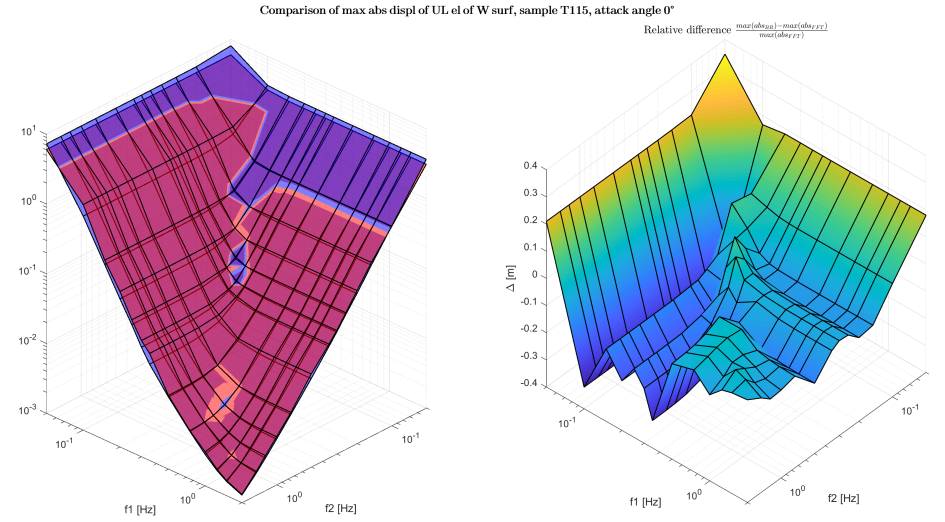

Figure 4.38: Max absolute displacement (FFT vs. B&R) of UR element on W surface in the frequency space.

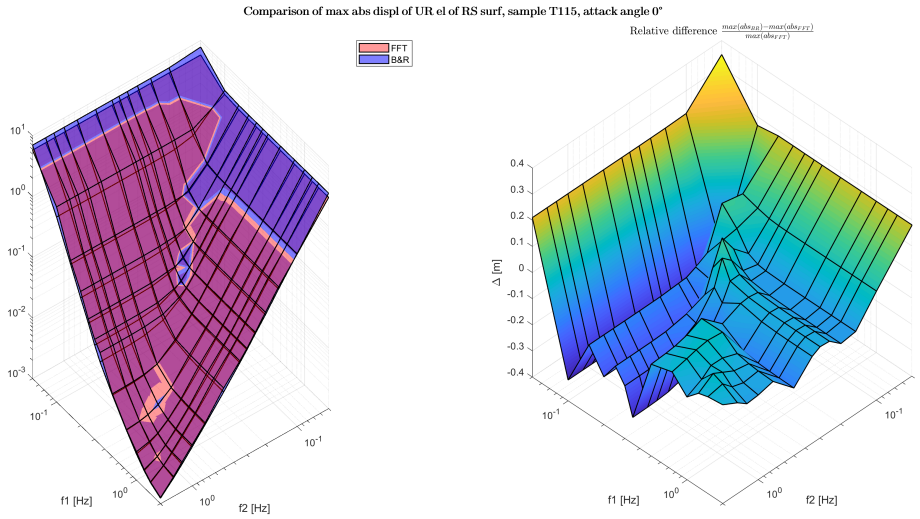

Figure 4.39: Max absolute displacement (FFT vs. B&R) of UR element on RS surface in the frequency space.

Same approach has been adopted for the computation of maximum values of the absolute displacements. For the FFT method, maximum absolute displacement has been computed by means of the MATLAB function **max** applied to the absolute displacement (of some selected elements, ex. Up-Left element of Windward surface) got as the square root of the sum of the square of the x and y displacements of the same element, that is

$$\max_{d,FFT} = \mathbf{max}(\sqrt{x_{FFT}^2 + y_{FFT}^2})$$

.

For the B&R method, approach has been similar to the one applied in the case of evaluation of maximum values of modal amplitudes, that is

$$\max_{d_i,BR} = \overline{d_i} + g\,\sigma_{d_i} \tag{4.47}$$

where

$$\overline{d_i} = \mathbf{\Phi}\,\overline{q_i} \tag{4.48}$$

$\overline{q_i}$ defined by Eq 4.45, σ_{d_i} is the standard deviation of the ith absolute displacement, g is the peak factor previously defined.

To compute standard deviation of absolute displacement σ_{d_i}, at first variance matrix of modal responses has been constructed as

$$\mathbf{\Sigma}_{q_{BR}} = \begin{pmatrix} \sigma^2_{q_{1,BR}} & 0 & 0 \\ 0 & \sigma^2_{q_{2,BR}} & 0 \\ 0 & 0 & \sigma^2_{q_{3,BR}} \end{pmatrix} \tag{4.49}$$

from which

$$\mathbf{\Sigma}_{d_{BR}} = \begin{pmatrix} \sigma^2_{x_{BR}} & 0 \\ 0 & \sigma^2_{y_{BR}} \end{pmatrix} = \mathbf{\Phi}\ \mathbf{\Sigma}_{q_{BR}}\ \mathbf{\Phi^T} \tag{4.50}$$

in which $\sigma^2_{x_{BR}}$ and $\sigma^2_{y_{BR}}$ are variance of x and y displacements of selected element respectively.

Important to note that off diagonal elements in Eq 4.49, which refer to *covariances*, equal to zero means that there is no correlation between two different modal responses, as it is the case in this Work as they have been assumed independent modal shapes.

Then

$$\max_{d_{BR}} = \mathbf{\Phi}\ \overline{q} + g\ \sqrt{\mathbf{\Sigma}_{d_{BR}}} \tag{4.51}$$

Figures 4.38 and 4.39 show an example of this application for the maximum absolute displacements of Up-Left on Windward and Up-Right element on Right-Sideward surface respectively.

From them we can notice some important features:

1. As expected, maximum absolute displacement increases with decreasing of natural modal frequencies, which means higher probabilities of resonance effects;

2. Additionally, remembering that these graphs are related to the sample T115 at 0° attack angle, we notice that there is a higher sensibility along the first mode. This makes sense since 0° attack angle means wind flow perpendicular to Windward surface, i.e. exciting mostly mode 1 (that causes displacements along y axis);

3. From both graphs, it can be noticed that maximum absolute displacements computed with FFT method are higher than the ones computed with B&R decomposition of the response. This is mathematically due to the fact that with FFT method, maximum value is given by the very maximum value registered in the time history; this means that even if average value is very small, if at a given point in time something would have caused a sharp peak in the recording, that would then represent the maximum value. On the other hand, the max values computed with B&R decomposition are based on the two main statistical properties, that are mean value and standard deviation. This approach clearly cuts off any possible local perturbation, since the average would not be that highly affected by some local peaks in a long time series of a random signal. However this is no more valid accordingly to Figures 4.38 and 4.39 for very low natural modal frequencies: this could be caused by the resonant component of the B&R decomposition, precisely by the local approximation error in its computation (which in almost all cases tends to overestimate it) discussed in Section 4.2.1, Fig 4.16.

4.4 Parametric analysis

Once Background and Resonant decomposition method has been validated, it is then possible to build response spectra by means of a parametric analysis, that is letting structural parameters changing, such as natural modal frequencies, damping ratio etc.

Of course, under a Structural Engineering point of view, the most significant quantity is the maximum displacement that the structure undergoes under a given loading, specially in a pre-design phase. Thus, in the following they will be shown response spectra regarding maximum absolute displacement of some significant reference points[13] for the most relevant configurations.

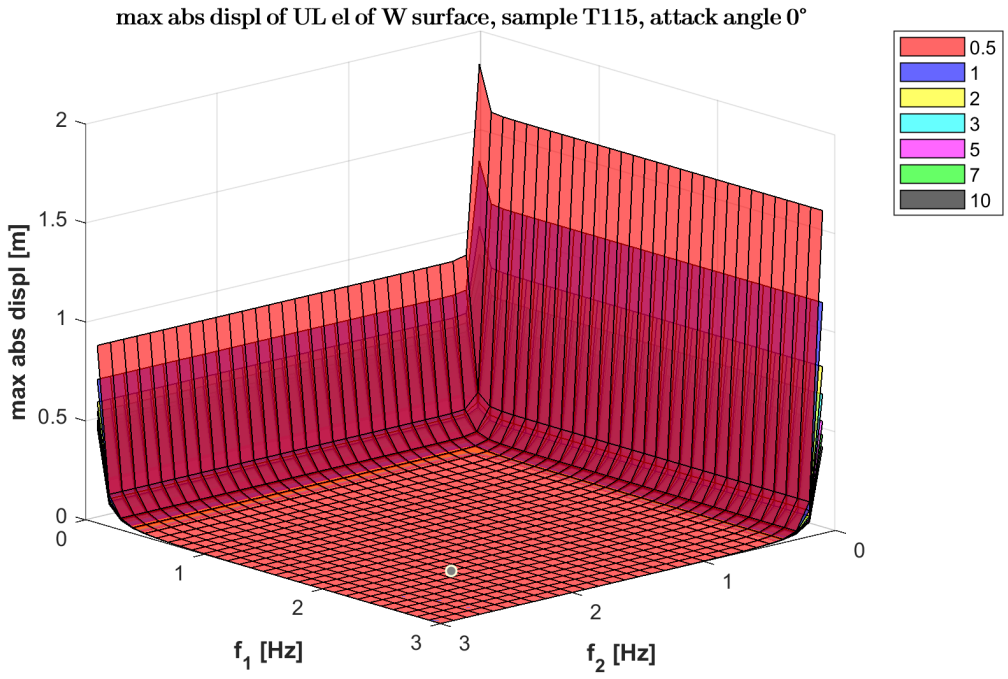

Figure 4.40: Response spectra of absolute displacement of UL element on W surface, sample T115, 0° attack angle.

[13] The ones at the top of the structure.

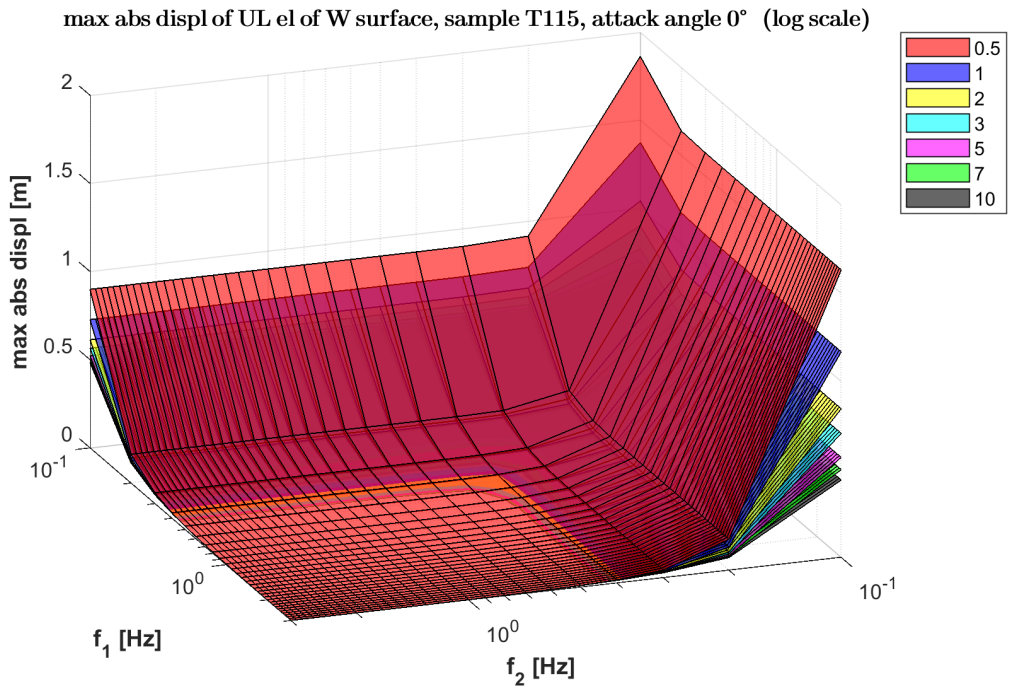

Figure 4.41: Response spectra of absolute displacement of UL element on W surface (log scale), sample T115, 0° attack angle.

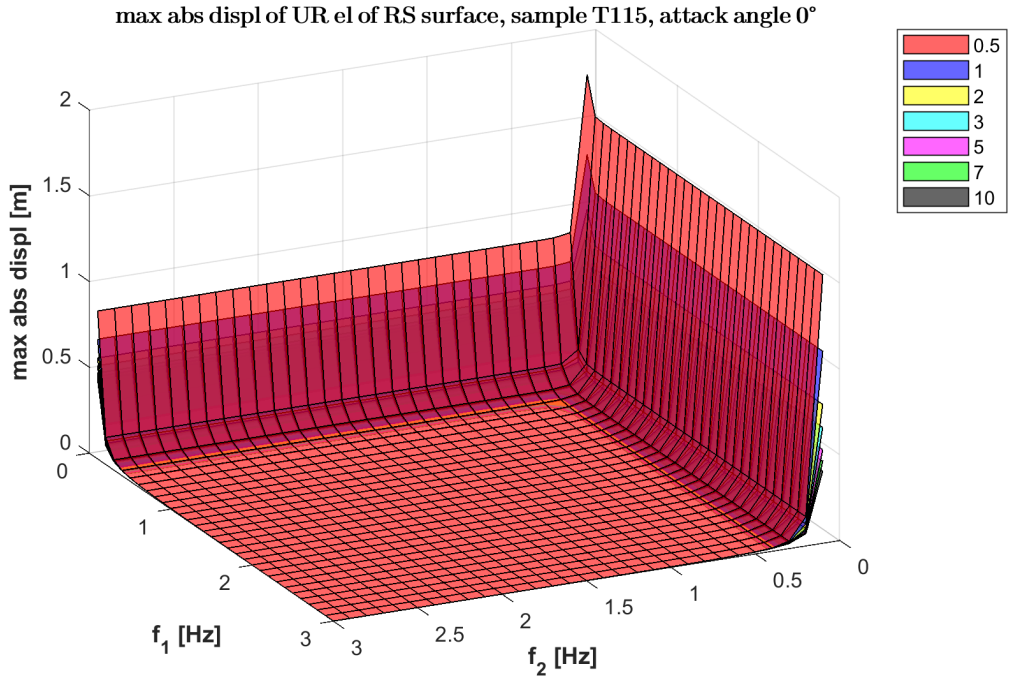

Figure 4.42: Response spectra of absolute displacement of UR element on RS surface, sample T115, 0° attack angle.

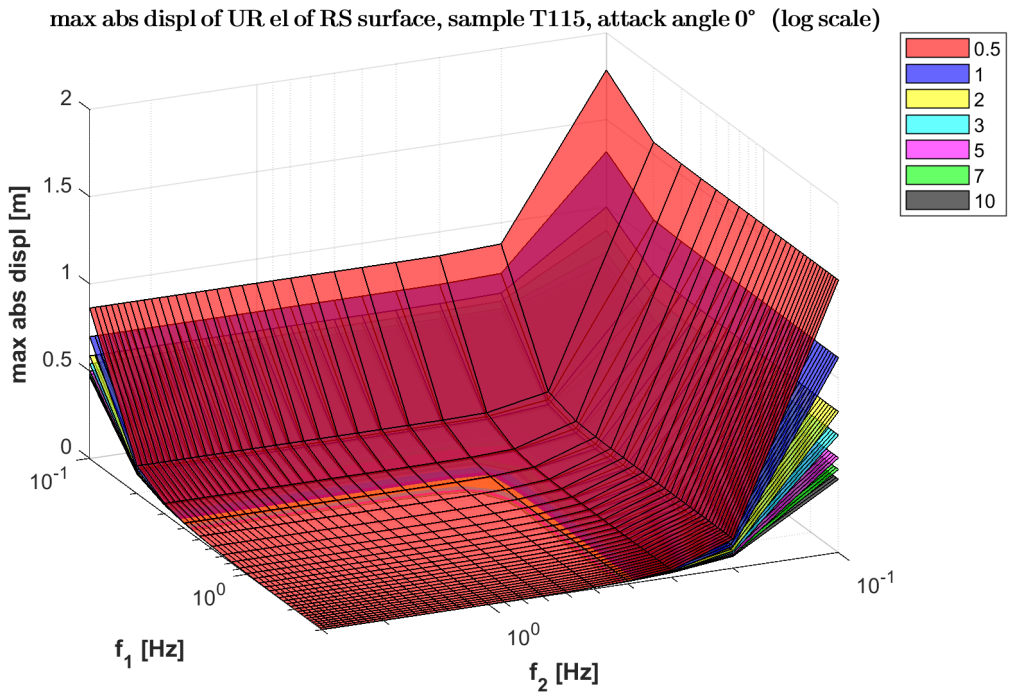

Figure 4.43: Response spectra of absolute displacement of UR element on RS surface (log scale), sample T115, 0° attack angle.

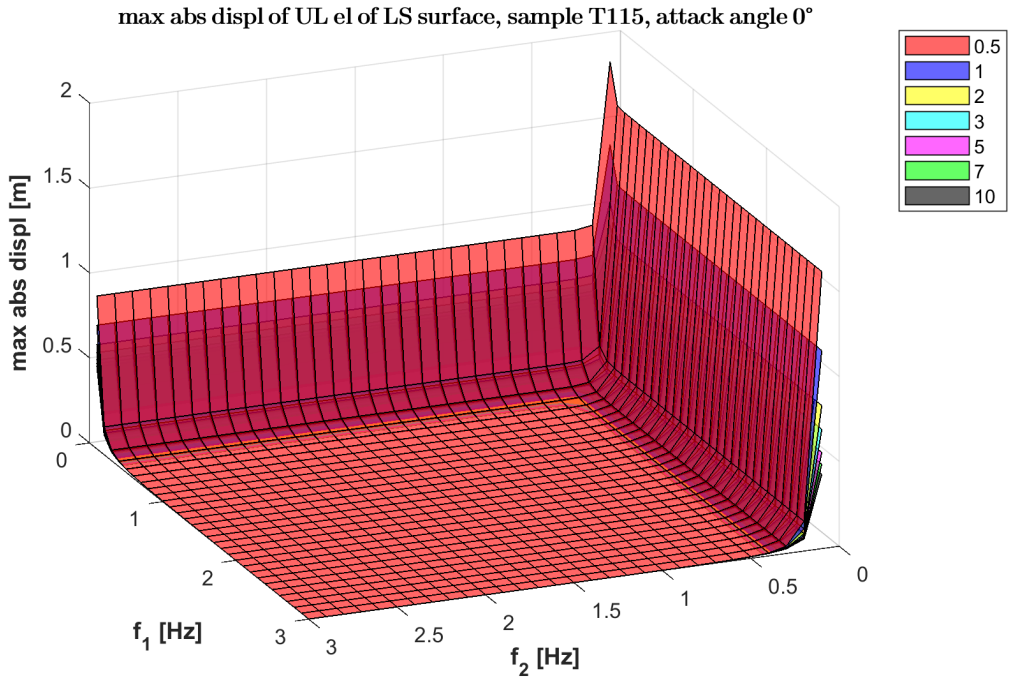

Figure 4.44: Response spectra of absolute displacement of UL element on LS surface, sample T115, 0° attack angle.

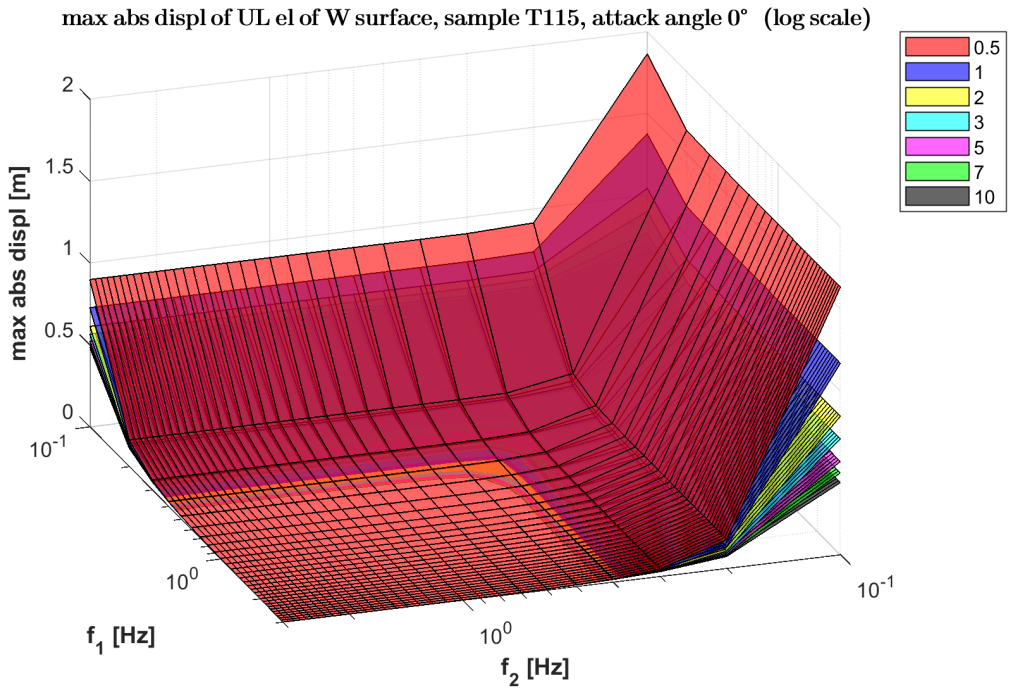

Figure 4.45: Response spectra of absolute displacement of UL element on LS surface (log scale), sample T115, 0° attack angle.

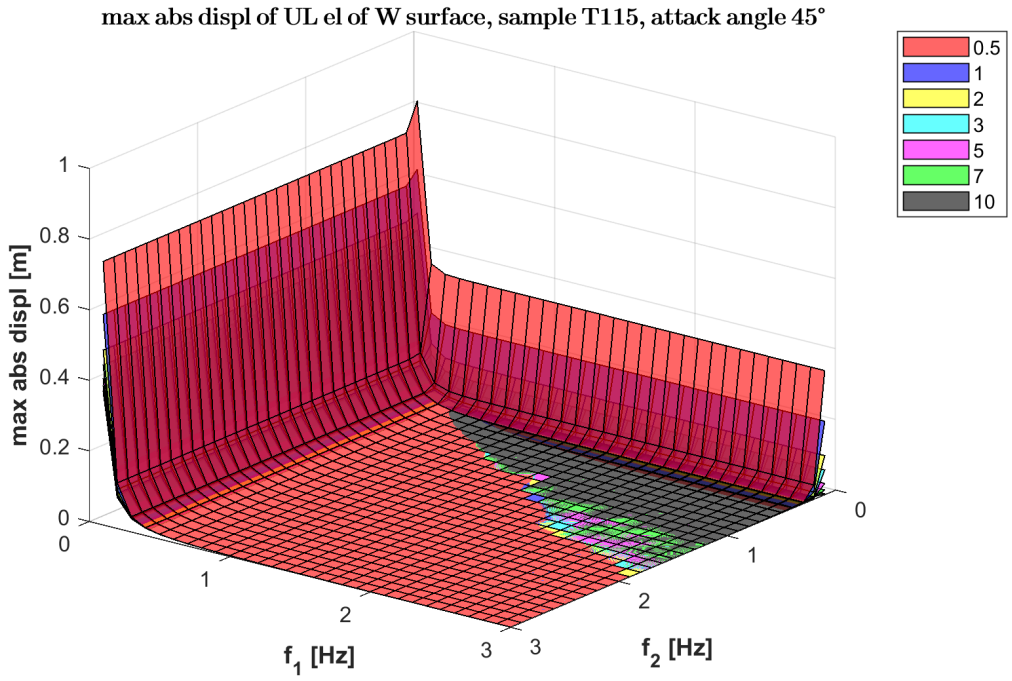

Figure 4.46: Response spectra of absolute displacement of UL element on W surface, sample T115, 45° attack angle.

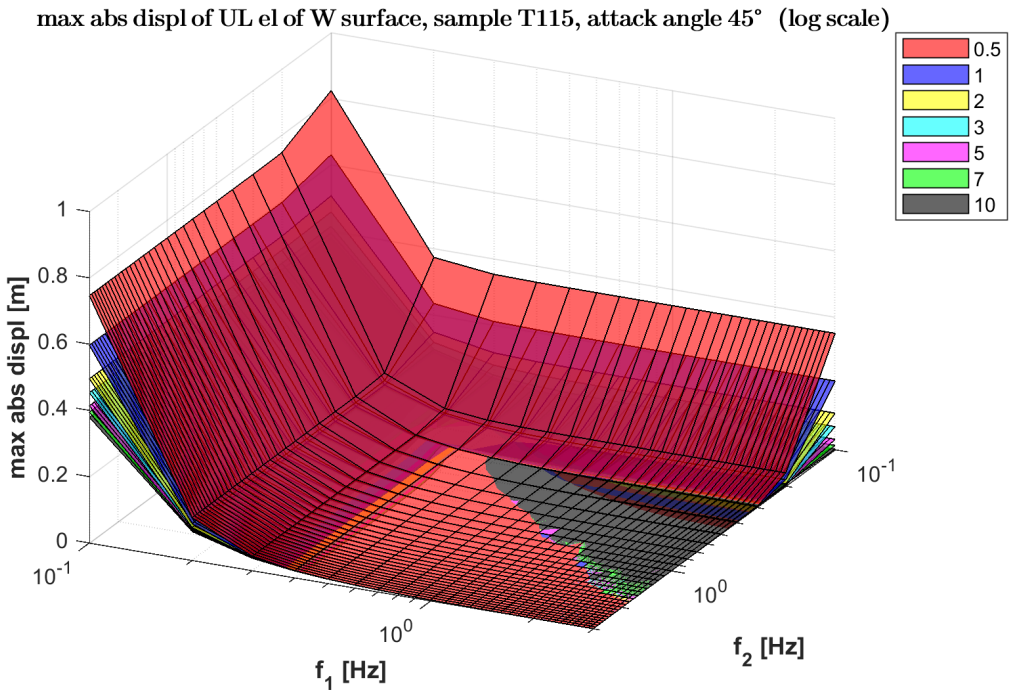

Figure 4.47: Response spectra of absolute displacement of UL element on W surface (log scale), sample T115, 45° attack angle.

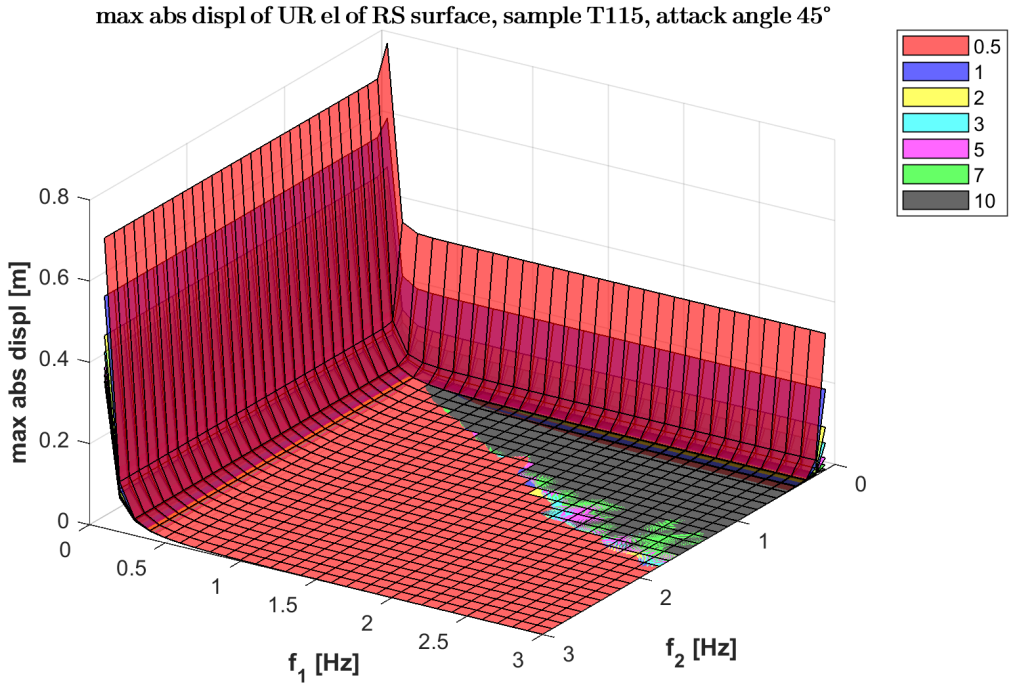

Figure 4.48: Response spectra of absolute displacement of UR element on RS surface, sample T115, 45° attack angle.

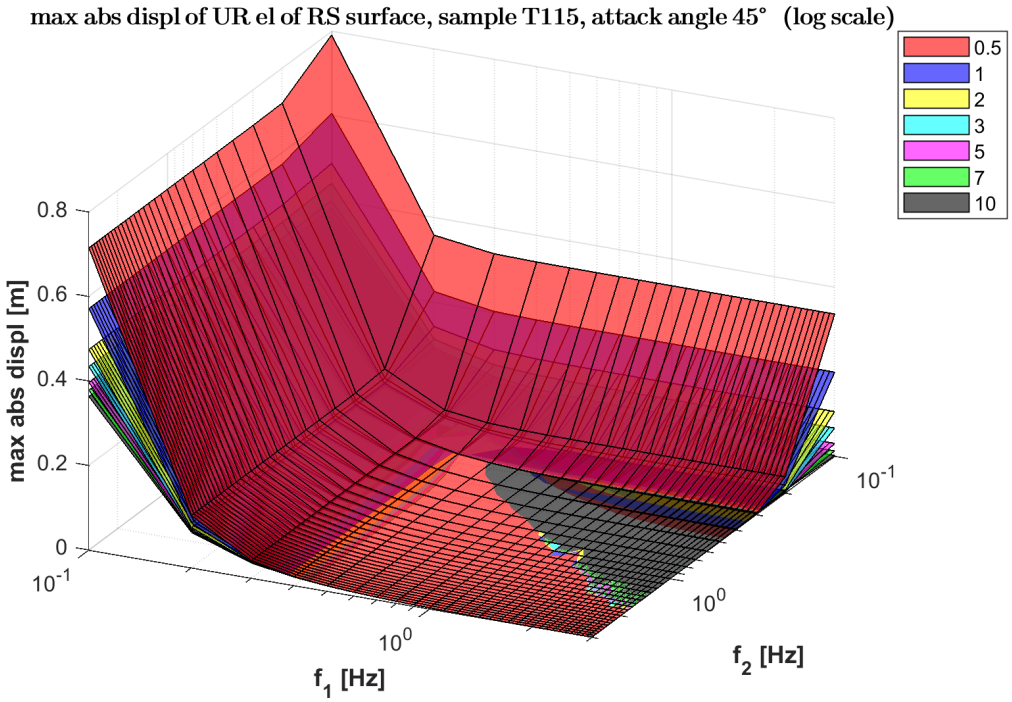

Figure 4.49: Response spectra of absolute displacement of UR element on RS surface (log scale), sample T115, 45° attack angle.

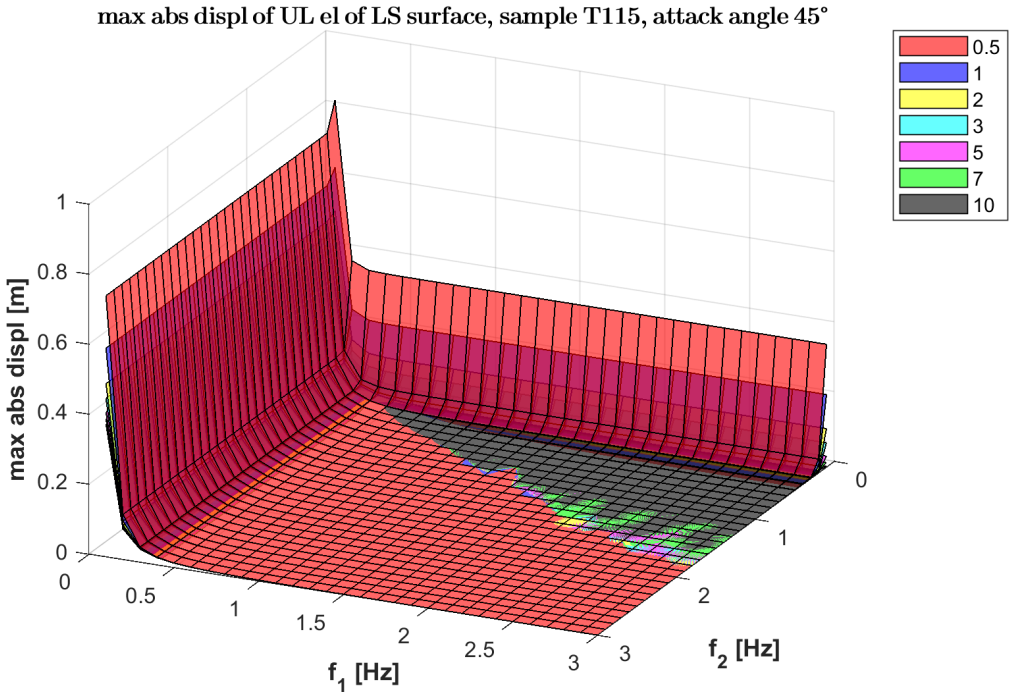

Figure 4.50: Response spectra of absolute displacement of UL element on LS surface, sample T115, 45° attack angle.

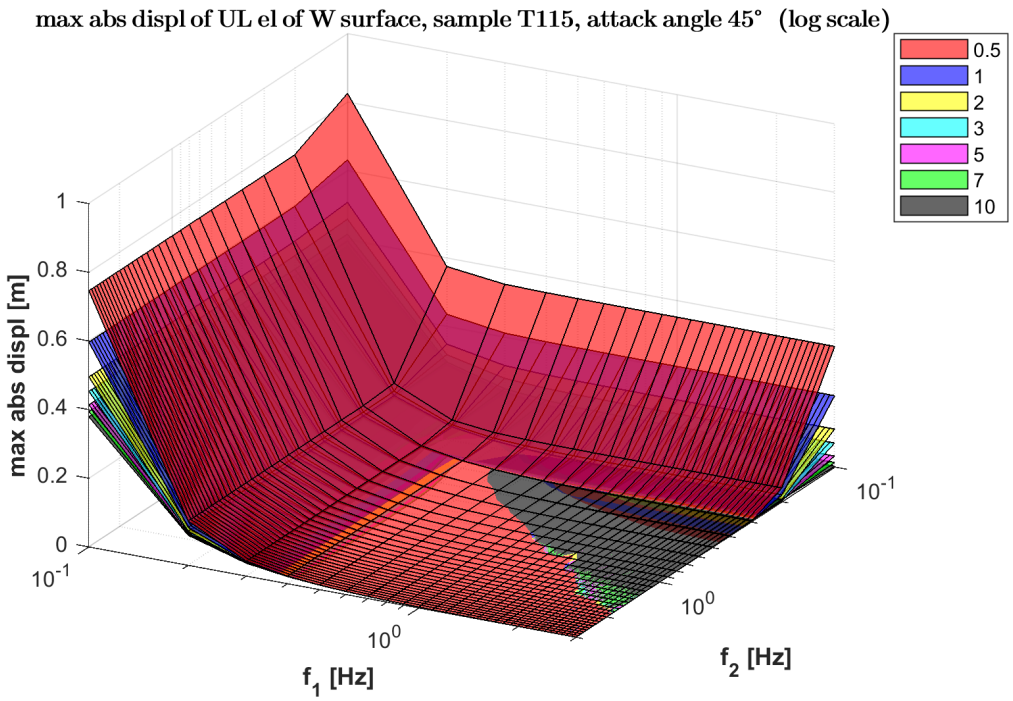

Figure 4.51: Response spectra of absolute displacement of UL element on LS surface (log scale), sample T115, 45° attack angle.

At this point we can do some considerations:

- Response, in terms of maximum absolute displacement, increases with the decreasing of both natural modal frequencies;
- Also, with same natural modal frequencies, response is higher with decreasing values of damping ratio;
- In configuration T115, 0° attack angle, response is more sensible to high decreasing of the second natural modal frequency ω_2 with respect to first mode. This is somehow the contrary of what someone would expect (considering that this specific configuration excites directly the first mode, being the wind flow perpendicularly to Windward — *along-wind* — surface). However, this is explained by the fact that vortex shedding effects are much higher on across-wind surfaces (Right and Left-Sideward surfaces) with respect to Leeward surfaces (back along-wind surface). Additionally to these minor vortex shedding effects on Leeward surface there is the fact that along-wind motion is somehow stabilised (in terms of variability of displacements) by the constant and perpendicular flow blowing on Windward surface, while it is not the case in across-wind motion. Therefore, letting the natural modal frequencies approaching zero (i.e. making the structure very slender), instability occurs in higher amplitude in the second mode.

  On the other hand, when it comes to the configuration T115 45° angle of attack, one would expect perfect symmetry of the response (following the symmetry of the geometry of the problem). However, clearly response is more sensible with respect to first natural modal frequency. This is simply due to randomness of measurements (of adimensionalised pressure coefficients), which by their side are not

perfectly symmetric (e.g. if, during test, for a very little time window, angle of the rotating plate was not exactly at 45°);

- Response (maximum absolute displacements) exhibits very high values (order of some meters in real scale) for natural modal frequencies approaching 0, specially for values lower than 0.5 Hz. However, in reality 0.5 Hz is already a very low natural frequency, which for most civil engineering structures is quite never reached (first mode has generally natural modal frequency of 1 Hz or above; than higher modes have increasing natural modal frequencies). Therefore, following representations will space in a more reasonable range of natural modal frequencies, such to represent more realistic values of structural response.

In Appendix B response spectra for other relevant configurations are reported.

5 Bispectrum and Bicorrelation

It has been said in previous chapters that when loading has Gaussian distribution[1] of the probability density function, mean value and Power Spectral Density Function (or equally variance) fully characterise a random process. Also, if loading is Gaussian, then also response is Gaussian.

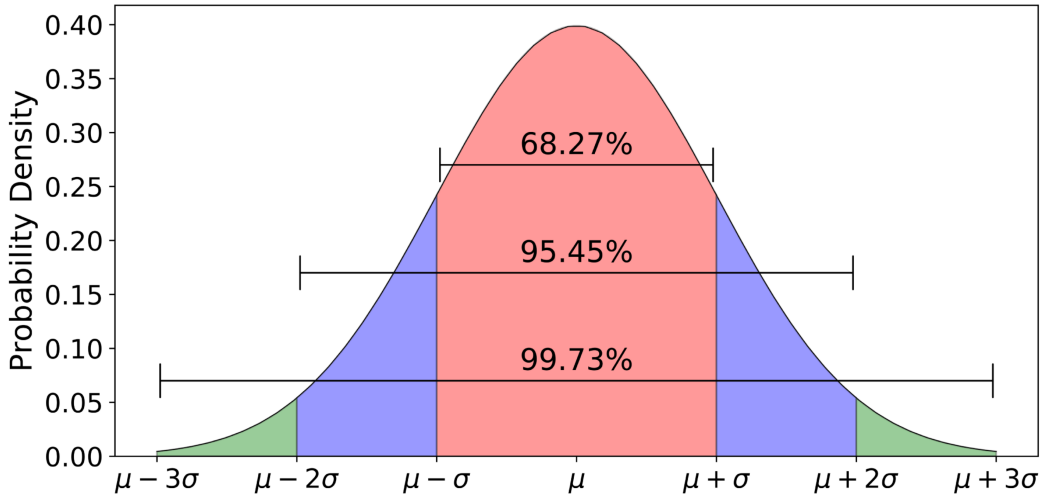

Figure 5.1: Example of Gaussian Distribution of the probability density function. (source: https://towardsdatascience.com)

In Chapter 4 we then showed, based on this concept, as dynamic response can be decomposed into its two basic components: a *background* component, which accounts for the quasi-static response (i.e. mean response, when loading has very low frequencies, hence high periods), and a *resonant* component, which happens when frequency of the excitation is well close to the natural frequency of the structure (in a specific mode) (see Eqs 4.44 and 4.47).

However, when a random process (i.e. loading or response) is no more Gaussian, mean value and PSD are no more sufficient to fully characterise the random process. This is because the loss of the Gaussianity property (i.e. symmetry of the probability density function with respect to y axis in correspondence of the mean value μ_x along the x axis) causes the needing of an additional info regarding the asymmetry of the process.

In this context, there exist quantities, similar to the PSD, that are correlated to statistical moments higher than two[2] in the frequency space. In particular, the *bispectrum* $B_{p^*}(\omega_1, \omega_2)$ "represents the distribution of the third central moment of the modal force p^* in a 2-D frequency space" [**?**]. The Bicorrelation is obtained by means of Inverse Fourier

[1] $p(x) = \frac{1}{\sqrt{2\pi\sigma_x^2}} \exp(-\frac{(x-\mu_x)^2}{2\sigma_x^2})$

[2] The statistical moment of order 2 is the *variance*, which has been seen coming from the integration of the PSD in the frequency domain.

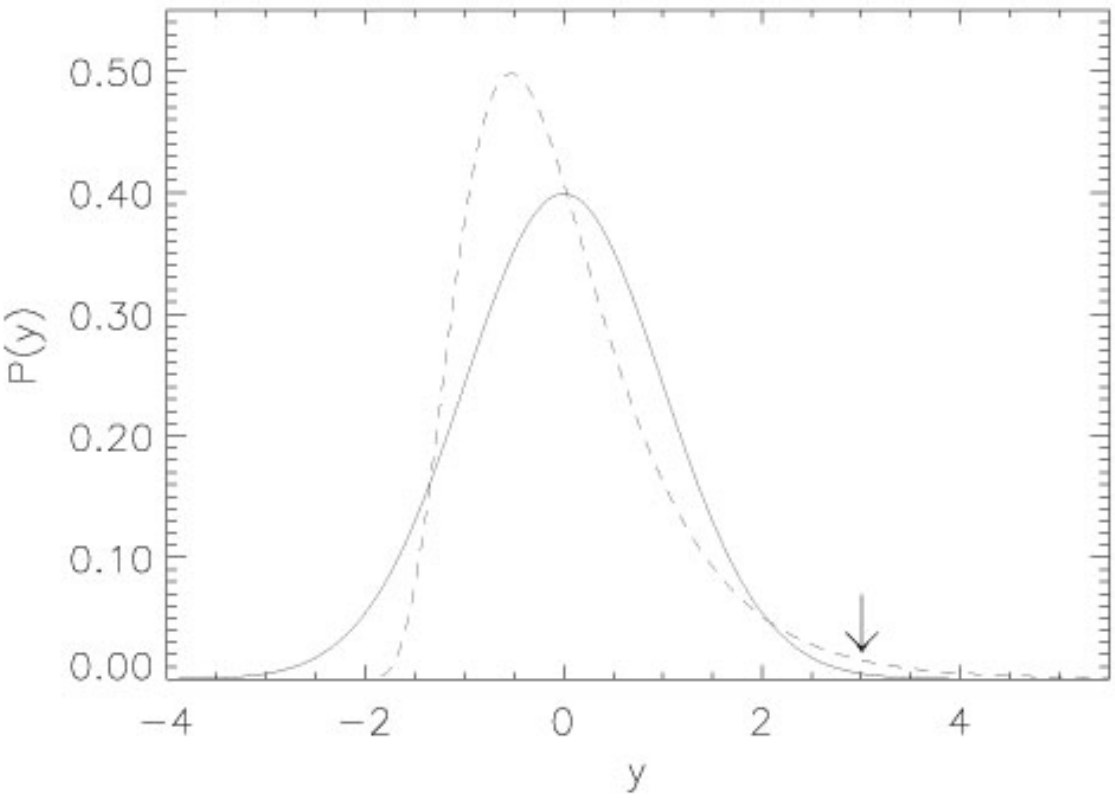

Figure 5.2: Comparison of non-Gaussian p.d.f. (dashed line) with respect to a Gaussian one (continuous line). (source: https://ned.ipac.caltech.edu)

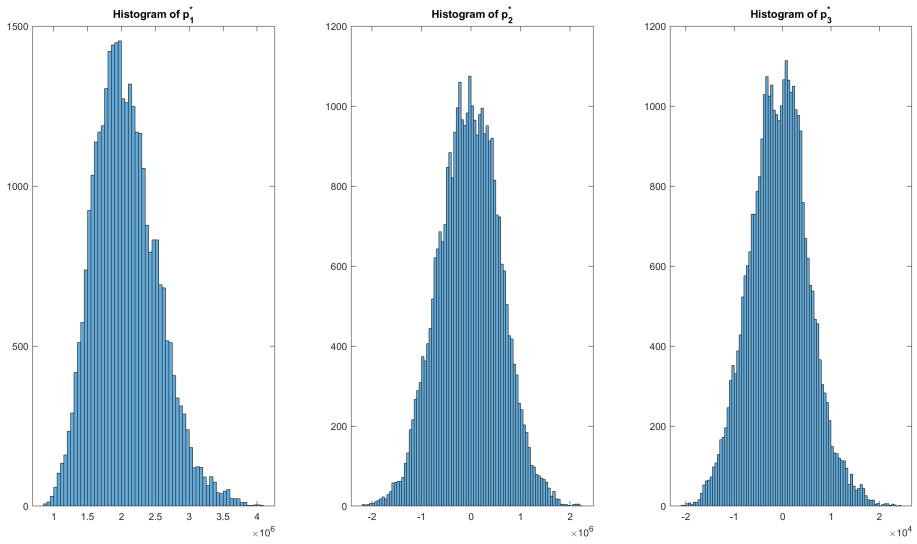

Figure 5.3: Histograms of modal forces, sample T115, 0° attack angle.

Transform (in the frequency space) of the bispectrum.

In other words, B&R and B&bR decompositions go together. The first is related to the variance of the random process, linked to the "dispersion" in the p.d.f., while B&bR which refer to the third statistical central moment gives information about the asymmetry of the p.d.f. (i.e. non-Gaussianity).

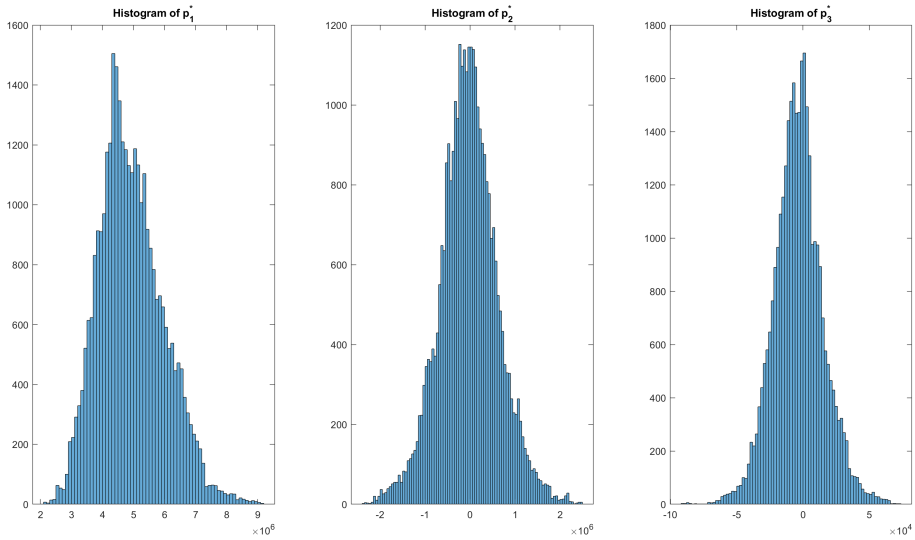

Figure 5.4: Histograms of modal forces, sample T215, 0° attack angle.

Moreover, in the framework of non-Gaussian random input process, previous Eqs 4.44 and 4.47 are no more valid because of the assumed value given to the peak factor g (whose range is based on Gaussian processes). This because , if input process is strongly non-Gaussian, previous assumption on conventional peak factor leads to non-conservative estimates estimates due to failure to include long tail regions inherent to non-Gaussian processes (Kwon DK et al. 2010). Therefore, when loading is non-Gaussian, it is needed to better investigate on the peak factor g in order to be able to compute more realistic extreme values of the response, because in this case

$$g = g(\gamma_3, \gamma_4) \tag{5.1}$$

γ_3 and γ_4 being *skewness* and *excess kurtosis* of the non-Gaussian input random signal.

However, that being said, this Work will not further exploit its application in determining its effect in the computation of extreme value of the response, even if it would have been of interest then the comparison with extreme values obtained by B&R decomposition. Still, this could be topic of further studies on this topic.

Nonetheless, everything here is based on the computation of the third statistical central moment of the response $m_{3,q}$. In the following they will be compared analytical and numerical solutions of the latter entity, in order to validate a cost-effective method that can be applied in early stages of a structural analysis.

Accordingly, the third central moment of the response is obtained as

$$m_{3,q} = \int \int_{-\infty}^{\infty} B_q(\omega_1, \omega_2)\, d\omega_1 d\omega_2 \tag{5.2}$$

in which $B_q(\omega_1, \omega_2)$ is the Bispectrum of the modal response given by

$$B_q(\omega_1, \omega_2) = K_2(\omega_1, \omega_2)\ B_{p^*}(\omega_1, \omega_2). \tag{5.3}$$

$B_{p^*}(\omega_1, \omega_2)$ is the Bispectrum of the modal force, $K_2(\omega_1, \omega_2)$ is the second Volterra Kernel expressed as

$$K_2(\omega_1, \omega_2) = H(\omega_1)\ H(\omega_2)\ \overline{H}(\omega_1 + \omega_2) \tag{5.4}$$

where the overbar denotes the complex conjugate. Nonetheless, only the real part of $K_2(\omega_1, \omega_2)$ is of interest.

However, it can be soon realised that higher order statistical analysis would not be applied if the double integral in Eq 5.2 has to be performed numerically, since, for huge structures finite element models (as it is quite always the case), computational costs (i.e. time) would be out of reason.

Then, the objective of this chapter, as well as This Work, is to provide an approximate numerical solution of the computation of the third central moments of the response based on the one of the loading, as an extension of the Background and Resonant (B&R) response (with respect to second central moments, i.e. variance).

The basic concept is identical to the previous one: splitting the total response in two components, that is

$$B_{q,BbR} = B_{q,B} + B_{q,bR} \tag{5.5}$$

where

$$B_{q,B}(\omega_1, \omega_2) = \frac{B_{p^*}}{k^{*3}} \tag{5.6}$$

is the bispectrum of the *background* component referring to the quasi-static behavior, and $B_{q,bR}$ is the bispectrum of the *biresonant* one.

Computation of the third statistical moment of the background component is straightforward: by integrating Eq 5.6

$$\begin{aligned} m_{3,q,B} &= \int\int_{-\infty}^{\infty} B_{q,B}(\omega_1, \omega_2)\ d\omega_1 d\omega_2 = \int\int_{-\infty}^{\infty} \frac{B_{p^*}(\omega_1, \omega_2)}{k^{*3}}\ d\omega_1 d\omega_2 \\ &= \frac{1}{k^{*3}} \int\int_{-\infty}^{\infty} B_{p^*}(\omega_1, \omega_2)\ d\omega_1 d\omega_2 = \frac{m_{3,p^*}}{k^{*3}} \end{aligned} \tag{5.7}$$

On the other hand, it is not that simple when it comes to the third statistical moment associated with the biresonant component, since it would require the double integration of the second Volterra Kernel:

$$
\begin{aligned}
m_{3,q,bR} &= \int\int_{-\infty}^{\infty} B_{q,bR}(\omega_1,\omega_2)\, d\omega_1 d\omega_2 = \int\int_{-\infty}^{\infty} (B_q - B_{q,B})(\omega_1,\omega_2)\, d\omega_1 d\omega_2 \\
&= \int\int_{-\infty}^{\infty} \left[K_2(\omega_1,\omega_2) - \frac{1}{k^{*3}}\right] B_{p^*}(\omega_1,\omega_2)\, d\omega_1 d\omega_2
\end{aligned}
\tag{5.8}
$$

In this perspective, Denoël has studied ([6]) the problem in order to be able to compute an approximate value of the third statistical moment of the biresonant component avoiding the double integration in the frequency space.

More specifically, noticing that biresonant component is characterised by six peaks, he focused on the peak located at $(\omega_1,\omega_2) = (\omega_0, 0)$, for which the approximate bispectrum is given by

$$
\hat{B}_{q,bR_1}(\omega_0\,(1+\xi\eta_1), \omega_0\xi\eta_2) = \frac{1}{4k^{*3}\xi^2}\,\frac{\eta_1^2+\eta_1\eta_2+1}{\left(\eta_1^2+\eta_1\eta_2+1\right)^2+\eta_2^2}\, B_{p^*}(\omega_0, \xi\eta_2\omega_0) \tag{5.9}
$$

in which η_1 and η_2 are stretched coordinates defined such that

$$
\omega_1 = \omega_0\,(1+\xi\eta_1) \tag{5.10}
$$

$$
\omega_2 = \omega_0\xi\eta_2 \tag{5.11}
$$

Thus

$$
\hat{m}_{3,q,bR_1} = \int\int_{-\infty}^{\infty} \hat{B}_{q,bR_1}(\omega_0\,(1+\xi\eta_1), \omega_0\xi\eta_2)\,\omega_0^2\,\xi^2\, d\eta_1 d\eta_2 \tag{5.12}
$$

or, in a more simplified way which avoids the double integration

$$
\begin{aligned}
\hat{m}_{3,q,bR_1} &= \frac{\omega_0^2}{4k^{*3}} \int_{-\infty}^{\infty} B_{p^*}(\omega_0, \xi\eta_2\omega_0) \int_{-\infty}^{\infty} \frac{\eta_1^2+\eta_1\eta_2+1}{\left(\eta_1^2+\eta_1\eta_2+1\right)^2+\eta_2^2}\, d\eta_1 d\eta_2 \\
&= \pi\frac{\xi\omega_0^3}{k^{*3}} \int_{-\infty}^{\infty} \frac{B_{p^*}(\omega_0,\omega_2)}{(2\xi\omega_0)^2+\omega_2^2}\, d\omega_2
\end{aligned}
\tag{5.13}
$$

We are now ready to step to the numerical analysis, in which the above explanation will be applied to the specific case.

The two only needed quantities to perform such computation are the time histories of input (modal forces) and output signal (modal responses, from FFT analysis), as well as all the structural parameters. Yet, it has been underlined many times that the objective of these decomposition is that of being able to predict with high accuracy extreme values of response by only analysing statistically the input random process: to do so of course it is needed to compare numerical approximations with analytical ones (FFT).

Sample T115, 0° attack angle

Firstly, the bispectrum[3] of the input signal is built.

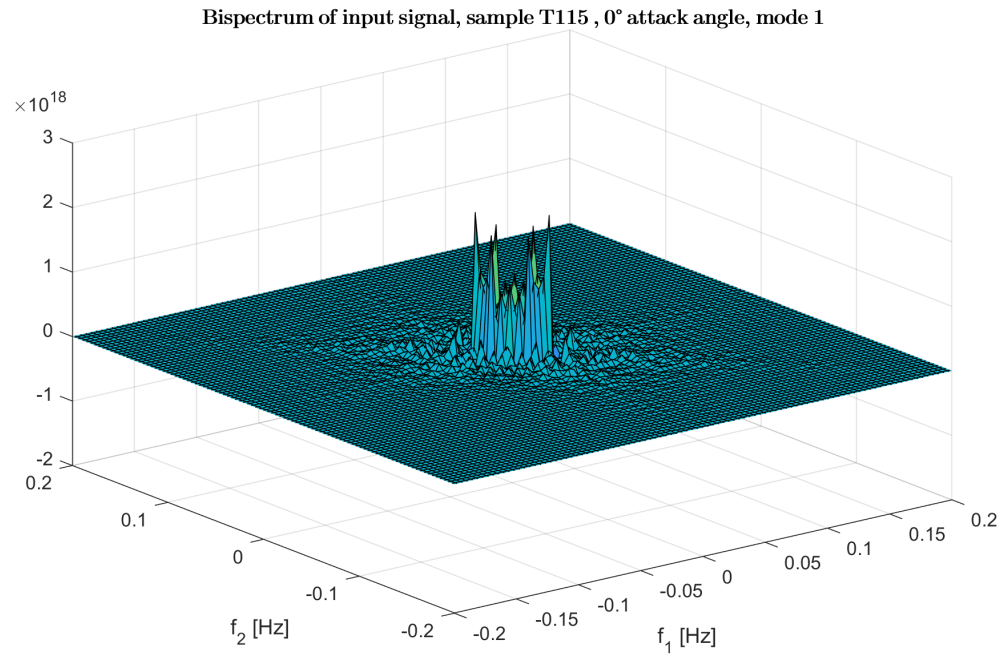

Figure 5.5: Bispectrum of first modal force, sample T115, 0° attack angle.

[3]For the computation of the various bispectrum, a function from the MATLAB File Exchange Database has been used.

As it can be seen, it shows a sharp (almost) circular peaks at the centre of the frequency space, when two modal frequencies approaches zero. This is simply an extension of the previous PSD of the input in Fig 4.4, which we hereby report for sake of clarity and easiness in seeing the likeness.

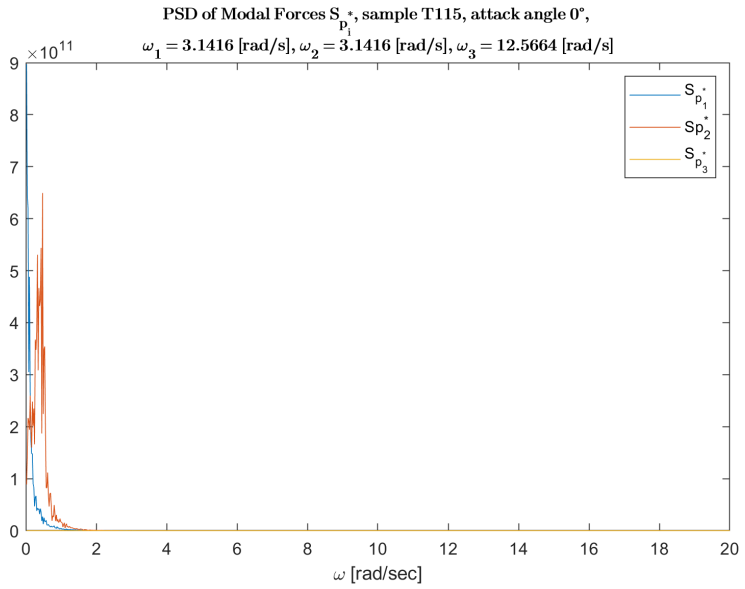

Figure 5.6: Plot of PSD of first modal force (blue), sample T115, 0° attack angle.

Then, having the time history of the respective modal amplitude coming from FFT analysis, we can build its bispectrum.

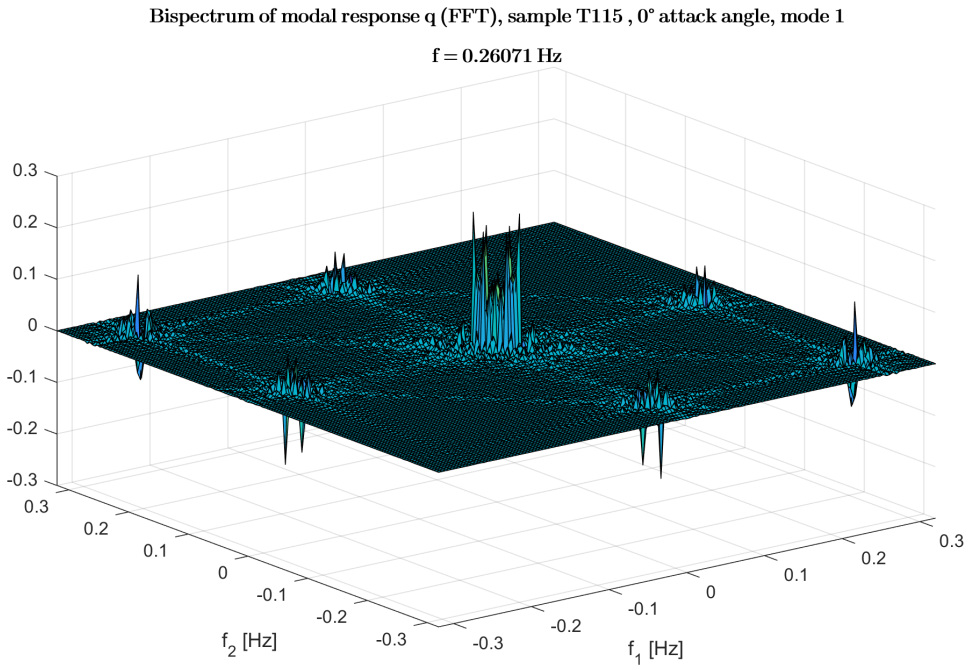

Figure 5.7: Bispectrum of first modal amplitude (FFT), sample T115, 0° attack angle, $f_1 = 0.26$ Hz.

Having a first look at it, it can be clearly noticed how it has 6 peaks located at $(0, \pm\omega_0)$, $(\pm\omega_0, 0)$ and $\pm(\omega_0, -\omega_0)$ being ω_0 the natural frequency of the considered mode.

This is the one that should be compared with the numeric approximation which we discussed earlier.

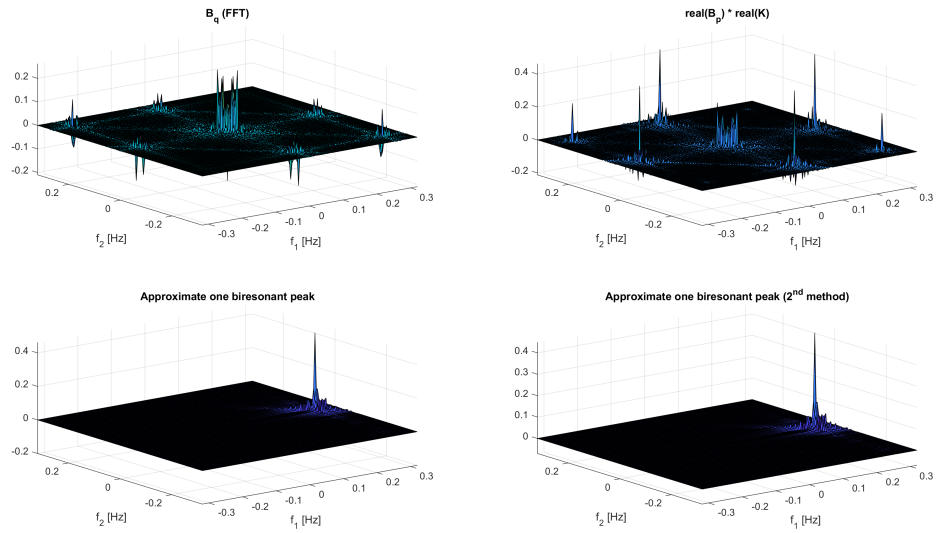

Figure 5.8: Comparison of numerical approximation with analytical and FFT bispectrum of modal response, sample T115, 0° attack angle, mode 1, $f_1 = 0.26$ Hz.

In latter figure, at the top-right corner the bispectrum of the modal amplitude computed with FFT is reported (previous Fig 5.7). On the top-left corner is the approximate bispectrum computed by means of the analytical solution, give by Eqs 5.2 and 5.3. The bottom two are represent the approximation of the peak (among the six) located at $(\omega_1, \omega_2) = (\omega_0, 0)$. They both refer to the local approximation as given in Eq 5.9, however with a slight difference in the computation of the local behaviour of the bispectrum of the modal force $B_{p^*}(\omega_0, \xi\eta_2\omega_0$ in correspondence of the considered peak.

For the bottom-left, latter quantity (which for clarity of the reader, we underline that represent a cut of bispectrum of the modal force at $\omega_1 = \omega_0$, i.e. a 2-D line) has been obtained by finding the index in the vector of frequencies at which the difference, in absolute value

$$|\overline{\omega_1} - \omega_0|$$

was minimum, that is in other words, a cut of the bispectrum of the modal force at

$$\omega_1 = \hat{\omega_0}$$

where $\hat{\omega_0}$ is the closest value in the frequency vector ω_1 (defined automatically by the desired refinement with which getting the results) with respect to the natural modal frequency ω_0. Of course, this is clearly an approximation because depending on the value of the absolute difference, the position index might lead to take a slice cut which could be either at a lower or higher frequency with respect to the natural one: and we are now able to understand that, considering also the high variability in amplitudes of the bispectrum at low frequencies, this could lead in over or underestimation of the

approximated ones of the modal amplitude which rely on it (which is the final objective of the B&bR decomposition).

On the other hand, for the bottom-right, it has been tried to exact the slice cut of the bispectrum of the modal force at the exact natural modal frequency ω_0 by using the **interp2** function in MATLAB. However, it has to be said that even if this method tries to get the info at the right value, is still an approximation as the previous one, which comes purely by the fact that interpolation method is not of the same order of the analytical expression of the bispectrum locally (which would be very tough, if not impossible, to know it exactly). For sake of clarity, a linear method of interpolation[4] has been used. Figures 5.9 and 5.10 show an example of the slice cut of the bispectrum of the modal force for both aforementioned methods.

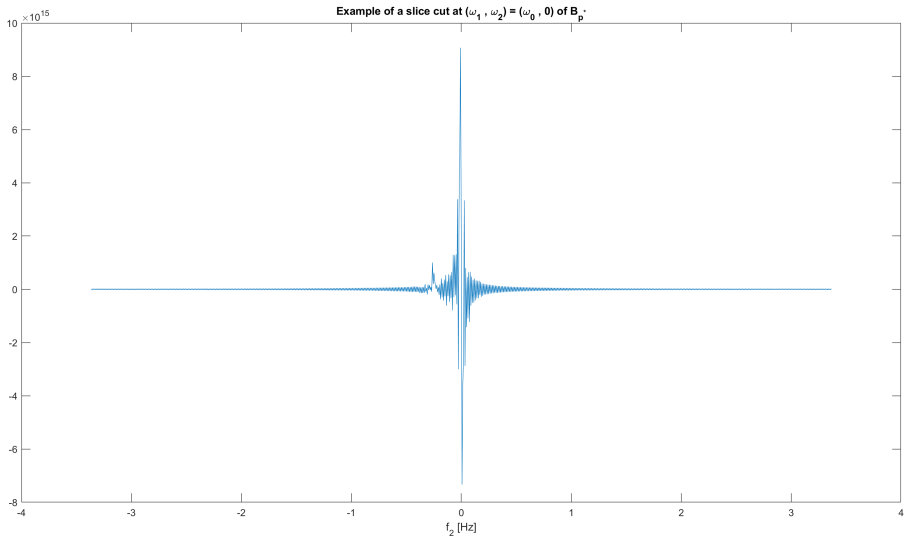

Figure 5.9: Example a slice cut of B_p bispectrum of modal force, first approximation.

Figure 5.8 also shows how analytical computation (see Eq 5.3) of the bispectrum of the modal response (up-right surface) well capture the background and biresonant response, having the same six peaks at the right locations. Also, background component matches quite perfectly. However, a slight difference in height of the biresonant peaks occurs between analytical and the one built from the time history of the modal amplitude (FFT). This can be related to the non-negligible contribution that gives the imaginary part of both the bispectrum of the modal force and the second Volterra Kernel. In fact, in figure 5.11 we can clearly notice the difference in amplitude between real and imaginary parts of the analytical solution of the bispectrum of the modal response.

The bottom two graphs show the numerical approximation of the biresonant peak located at $(\omega_0, 0)$: noticeably, the match quite well with the corresponding peak of the analytical solution, yet, having a slight difference in amplitude with the one coming from the FFT analysis. This could be also caused by the fact that these two approximated solution are based on the slice cut we introduced above: the precision in reproducing the

[4]To note that choice was arbitrary. Even a cubic method of interpolation, although more precise, would have led to same approximation errors as for the linear one.

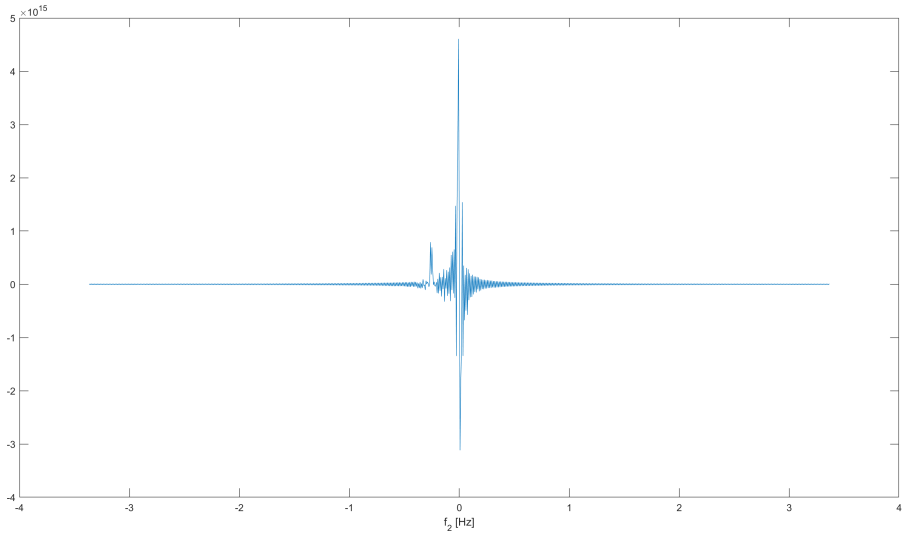

Figure 5.10: Example a slice cut of B_p bispectrum of modal force, second approximation.

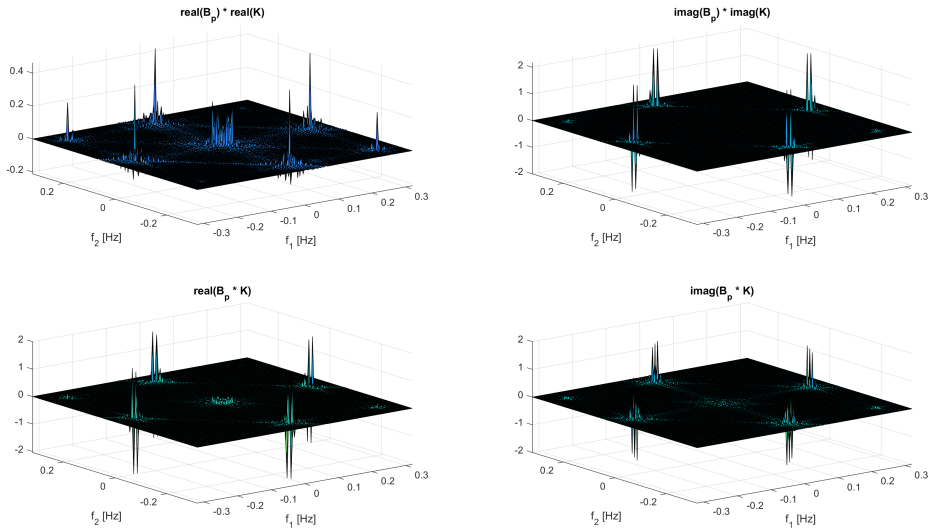

Figure 5.11: Imaginary and real parts of Bq computed analytically, sample T115, 0° attack angle, mode 1, $f_1 = 0.26$ Hz.

actual shape of the cut line depends on how refined the mesh of the bispectrum of the modal force is.

In fact, we can notice form Figures **??** **??** how results are sensible to a decreasing (either an increasing) in the refinement of the mesh of B_p:

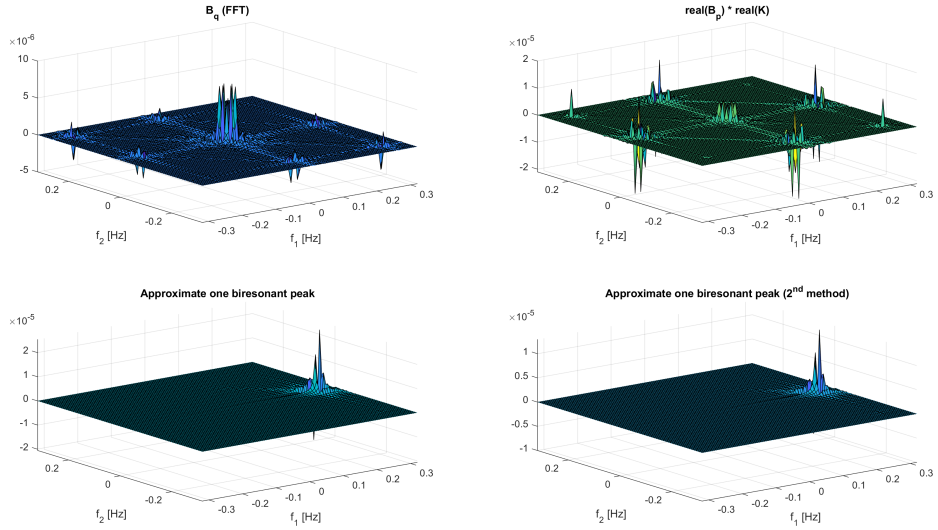

Figure 5.12: Comparison of numerical approximation with analytical and FFT bispectrum of modal response, sample T115, 0° attack angle, mode 1, $f_1 = 0.26$ Hz, decreased mesh refinement.

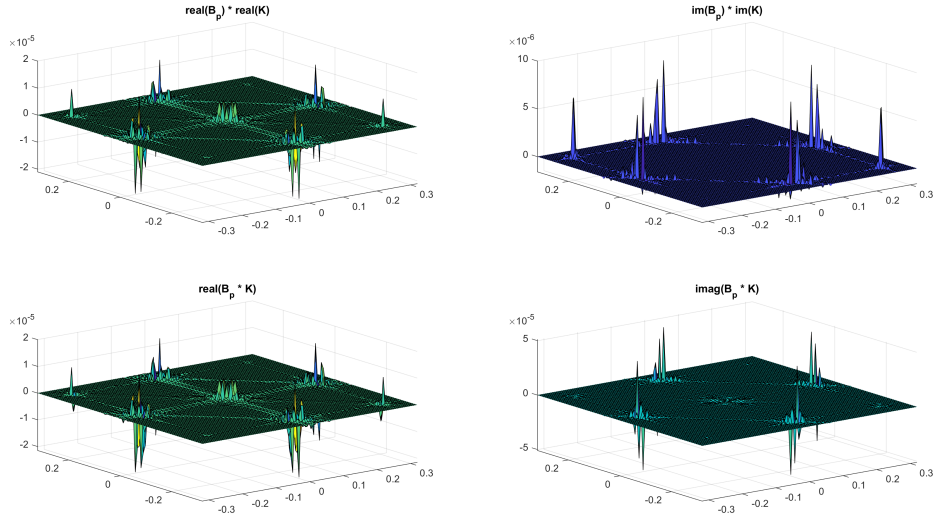

Figure 5.13: Imaginary and real parts of Bq computed analytically, sample T115, 0° attack angle, mode 1, $f_1 = 0.26$ Hz, decreased mesh refinement.

Interesting is to monitor what happens further decreasing the natural modal frequency, that is more in the resonance domain. Decreasing the modal frequency down to 0.05 Hz we observe:

It can be seen how in this case, the six peaks, which are now at lower frequencies as expected, are much higher in amplitude with respect to previous case, sign that, as it was also the case for the PSD (see Figs 4.30 and 4.31), resonant effects are more likely to happen. In fact, recalling the Bispectrum of the modal force in Fig 5.5 in which it was shown how it exhibits a very sharp peak at low frequencies, it can be clearly understood

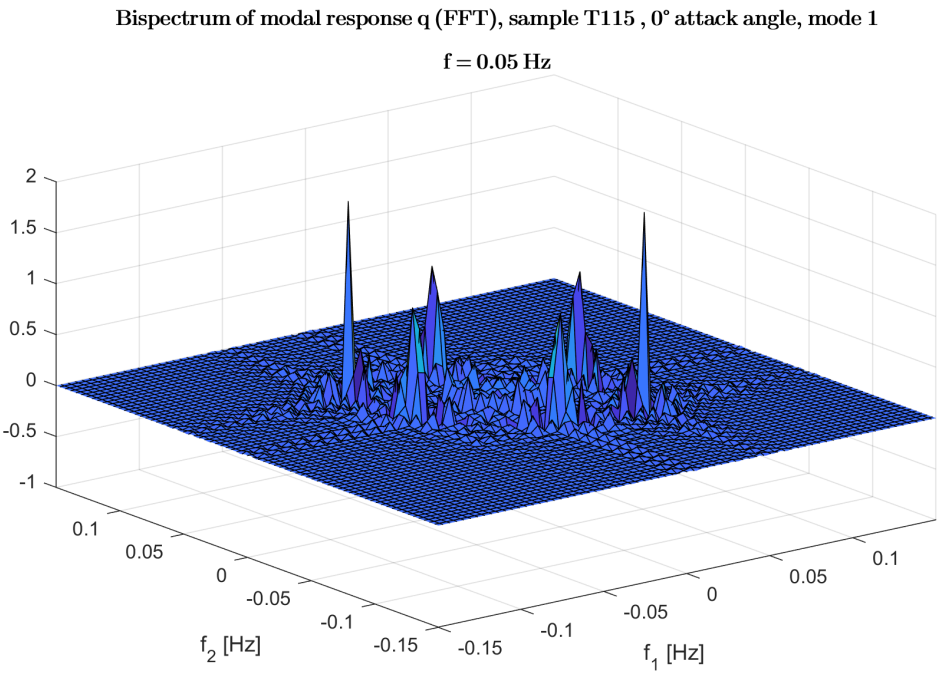

Figure 5.14: Bispectrum of first modal amplitude, sample T115, 0° attack angle, $f_1 = 0.05$ Hz.

that as soon as the natural modal frequency gets low enough such to ”fall” inside that region, response will be then for sure affected by resonant effects.

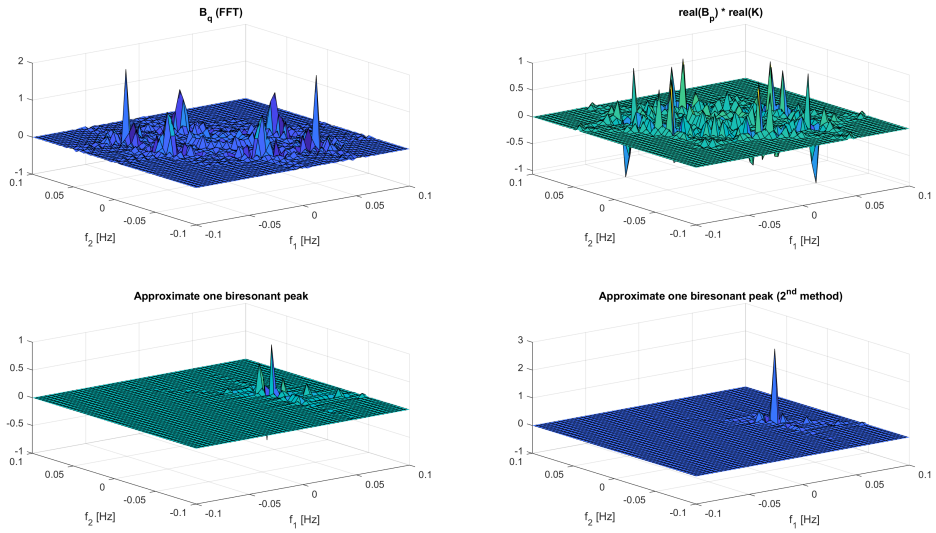

Figure 5.15: Comparison of numerical approximations of Bispectrum of modal response with analytical one, sample T115, 0° attack angle, mode 1, $f_1 = 0.05$ Hz.

Finally reported a parametric analysis in which the computation of the third statistical central moment of the modal response $m_{3,q}$ has been computed for varying natural modal frequencies, in order to better capture the behaviour of each of the approximate solutions here discussed.

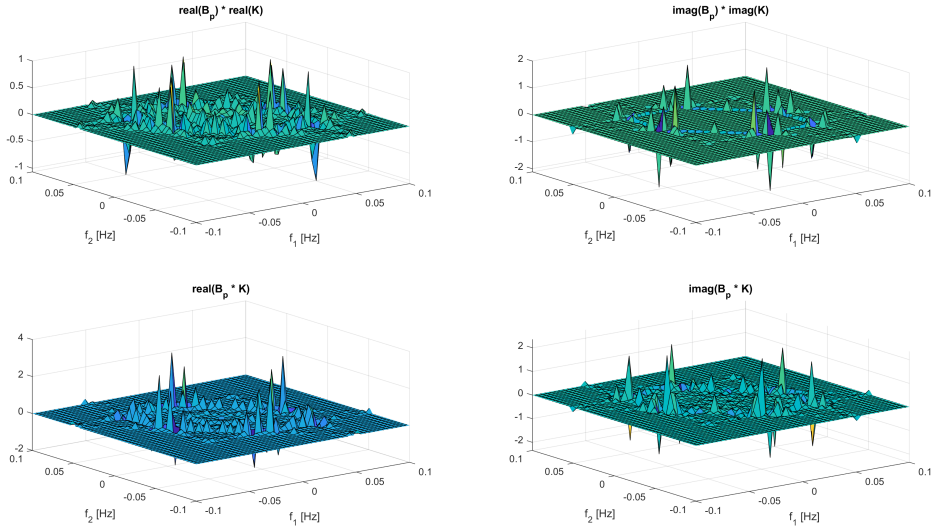

Figure 5.16: Imaginary and real parts of Bq computed analytically, sample T115, 0° attack angle, mode 1, $f_1 = 0.05$ Hz.

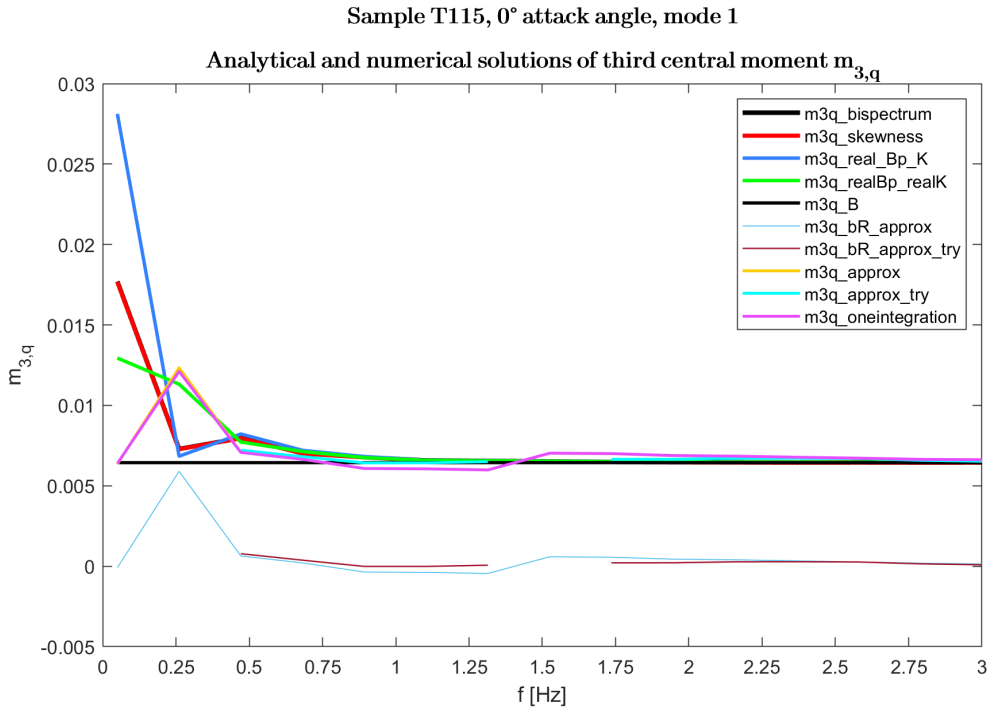

Figure 5.17: Parametric analysis of $m_{3,q}$, mode 1, sample T115, 0° attack angle.

in which:

$m3q\_bispectrum$ comes from the integration in the frequency space of the bispectrum of q coming from FFT analysis;

$m3q\_skewness$ is obtained, following the definition of the third statistical central moment, as

$$m3q\_skewness = \gamma_{3,q} \ * \ \sigma_q^3 \tag{5.14}$$

where $\gamma_{3,q}$ is the skewness and σ_q^3 the third power of the standard deviation of $q(t)$;

$m3q\_real\_Bp\_K$ comes from the integration in the frequency space of the bispectrum of q computed analytically as

$$m3q\_real\_Bp\_K = \int \int_{-\infty}^{\infty} \text{real}(B_{p^*} \ * \ K) \, d\omega_1 d\omega_2 \tag{5.15}$$

$m3q\_realBp\_realK$ comes from the integration in the frequency space of the bispectrum of q computed analytically as

$$m3q\_real\_Bp\_K = \int \int_{-\infty}^{\infty} (\text{real}(B_{p^*}) \ * \ \text{real}(K)) \, d\omega_1 d\omega_2 \tag{5.16}$$

$m3q\_B$ is the background component of the response, as in Eq 5.7 (constant as expected);

$m3q\_bR\_approx$ and $m3q\_bR\_approx\_try$ are the biresonant component coming from first and second approximation (in the slicing of B_p) respectively;

$m3q\_approx$ and $m3q\_approx\_try$ are the correspondent values to which the background component has been added, such to get the final approximated value of the third central moment;

$m3q\_oneintegration$ is the same as $m3q\_approx$ but based on Eq 5.13 instead of Eq 5.12.

We can evidently see how behaviour tends to quasi-static (i.e. only background component participates to total response) for increasing natural frequencies, starting from around 0.75 Hz.

Under this value, resonance is not negligible. Red and black (which is not visible since it is right behind the red one, meaning that there is perfect matching) lines refer to the target solution. All the others are obtained through numerical analysis. Clearly, behaviour is not stable for decreasing natural frequencies. Still, we have earlier mentioned some of the possible reasons of this instability, however further investigation is needed to better understand the real source and reason of it.

Still, all this was referring to the first mode only. Analysing second mode, we will notice some differences. To mention that following graphs will refer to second modal frequency of 0.05 Hz.

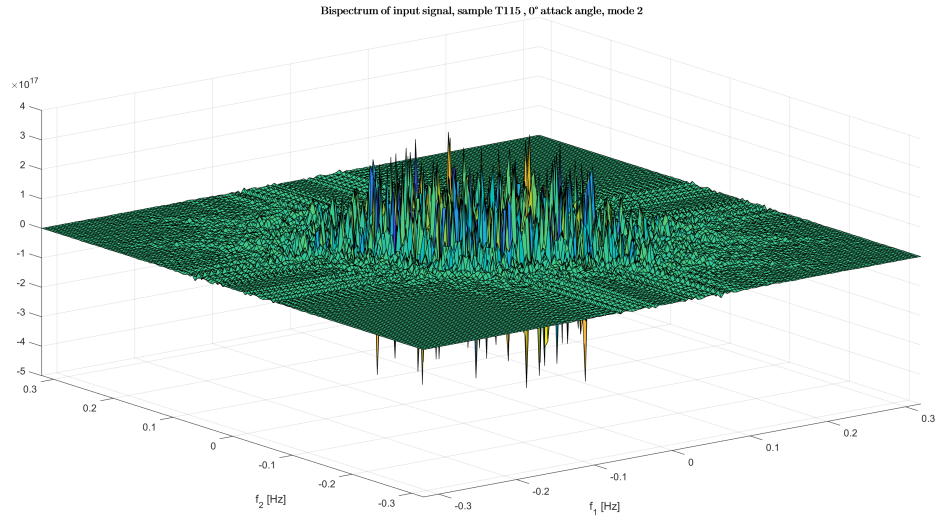

Figure 5.18: Bispectrum of second modal force, sample T115, 0° attack angle.

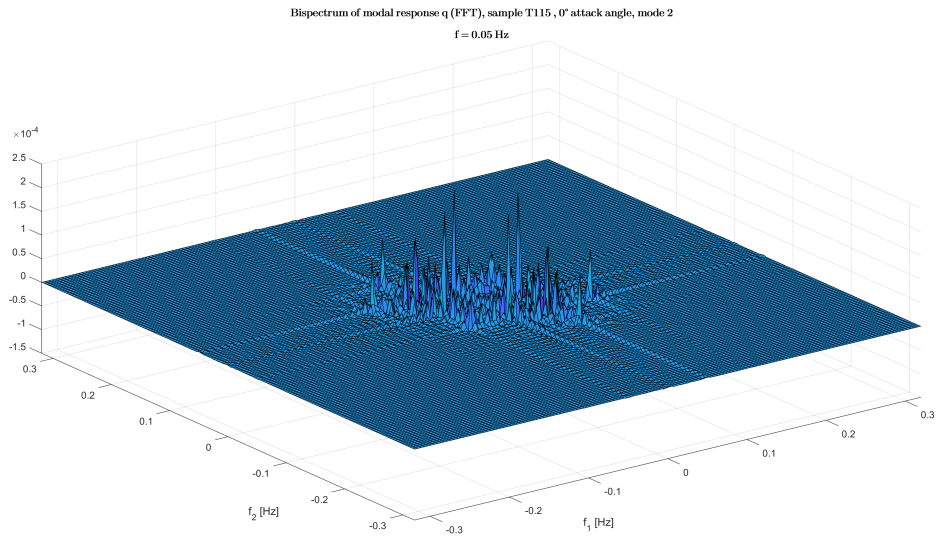

Figure 5.19: Bispectrum of second modal amplitude (FFT), sample T115, 0° attack angle, $f_2 = 0.05$ Hz.

Differently to previous case, bispectrum of modal amplitude has more than the previous six peaks. Still, we can observe the main six peaks (signed by the red arrows in Figs **??** and **??**) together with other six minor peaks located at $\pm(\omega_0, \omega_0)$, $\pm(-2\omega_0, \omega_0)$ and $\pm(-\omega_0, 2\omega_0)$.

This could be consequence of the fact that, with respect to mode 1, in mode two the bispectrum of the modal force has a wider extension of its energy content in the frequency space (see Fig 5.5 compared with Fig 5.18), even if smaller in amplitude.

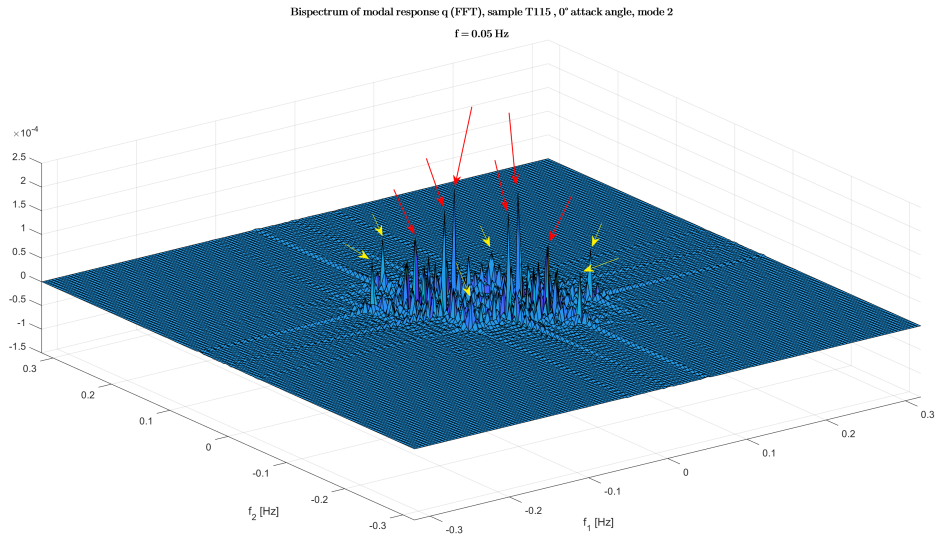

Figure 5.20: Identification of six major and minor peaks, mode 2, sample T115, 0° attack angle, $f_2 = 0.05$ Hz.

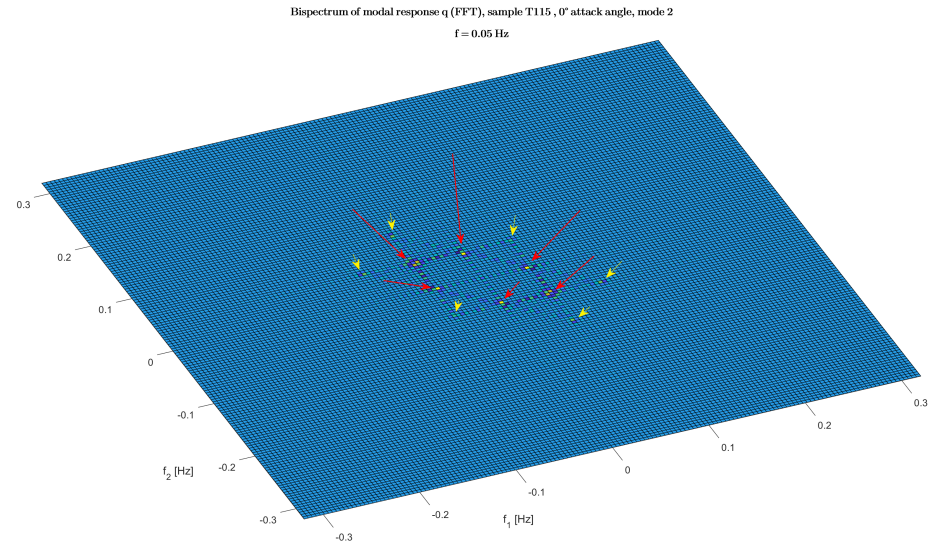

Figure 5.21: Above view of the six major and minor peaks, mode 2, sample T115, 0° attack angle, $f_2 = 0.05$ Hz.

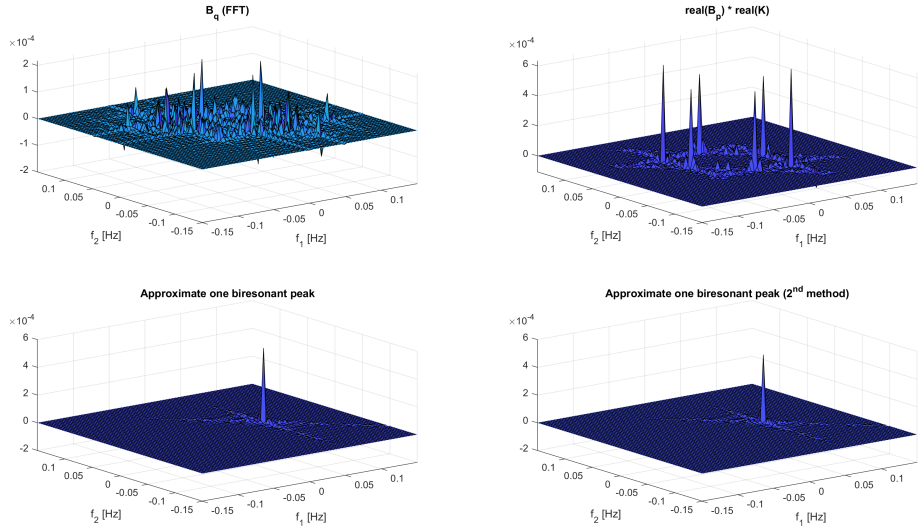

Figure 5.22: Comparison of numerical approximations of Bispectrum of modal response with analytical one, sample T115, 0° attack angle, mode 2, $f_2 = 0.05$ Hz.

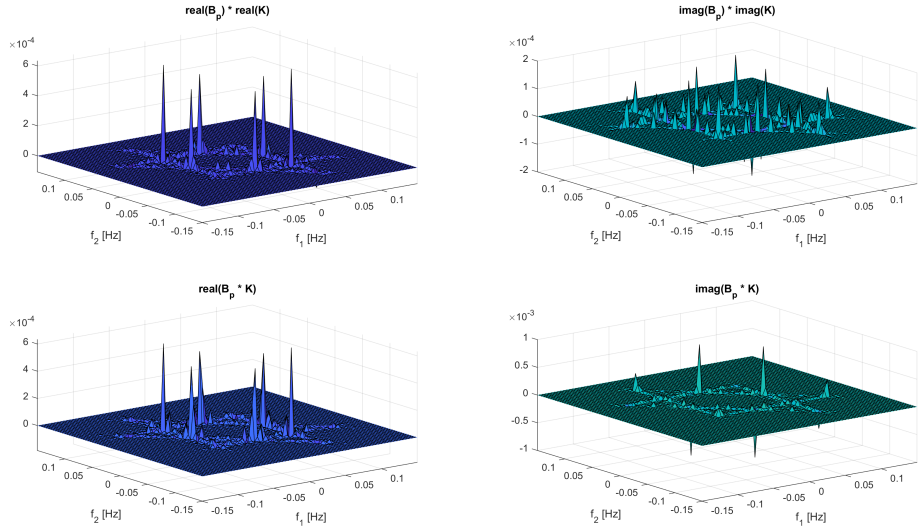

Figure 5.23: Imaginary and real parts of Bq computed analytically, sample T115, 0° attack angle, mode 2, $f_2 = 0.05$ Hz.

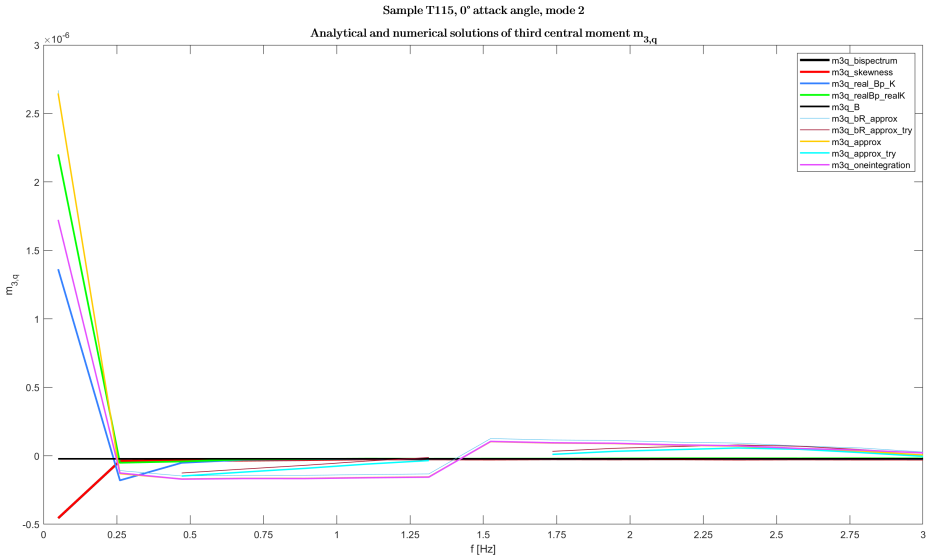

Figure 5.24: Parametric analysis of $m_{3,q}$, mode 2, sample T115, 0° attack angle.

Yet, although instability starts to occur at a lower value of the natural frequency (around 0.25 Hz), precision in numerical approximation of $m_{3,q}$ is not reached. One arrow in our favour could be that in this case amplitudes are considerably lower than in mode 1 (factor of 10^{-4}), but still does not justify the fact that trend is not even close to the one of the target one (red and black lines).

Increasing the natural modal frequency up to 0.26 Hz, we can notice a much better matching between analytical and FFT bispectrum of modal response, as well as the biresonant peak got from the two approximated numerical methods.

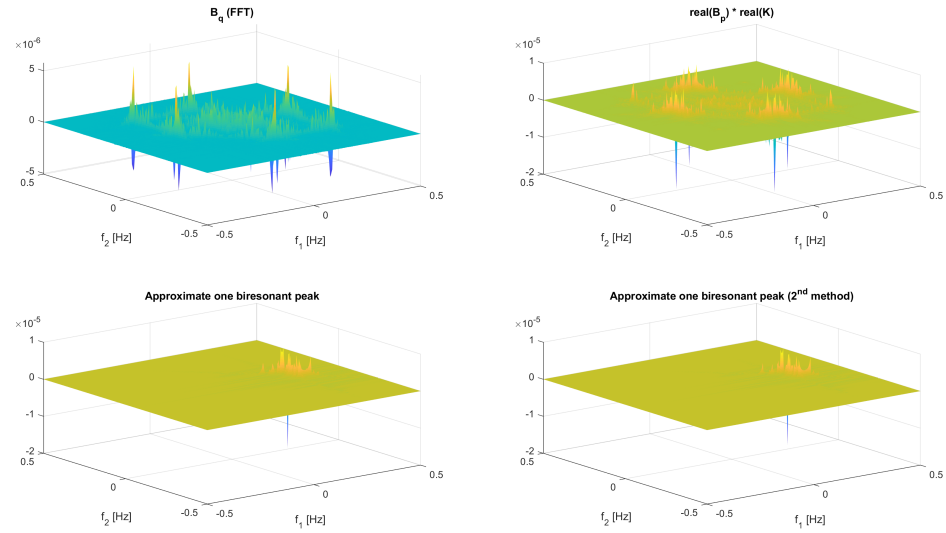

Figure 5.25: Comparison of numerical approximations of Bispectrum of modal response with analytical one, sample T115, 0° attack angle, mode 2, $f_2 = 0.26$ Hz.

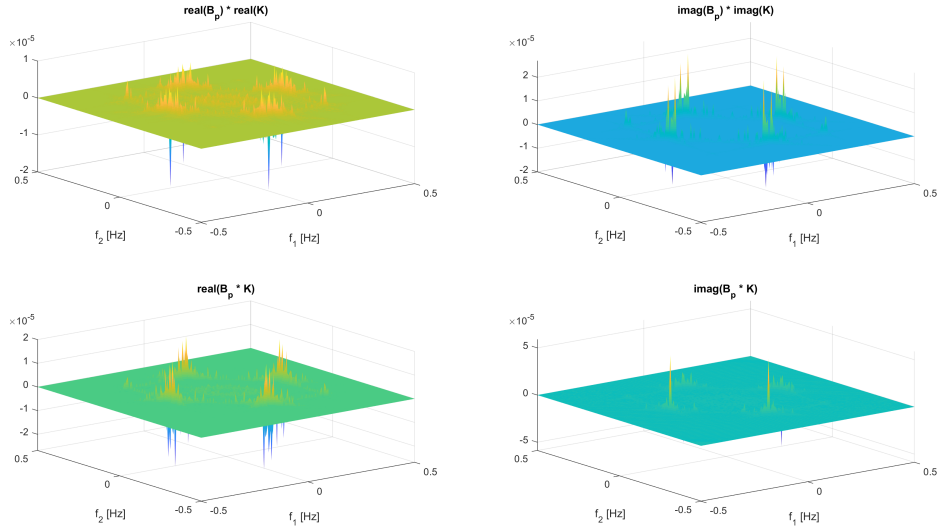

Figure 5.26: Imaginary and real parts of Bq computed analytically, sample T115, 0° attack angle, mode 2, $f_2 = 0.26$ Hz.

Sample T215, 0° attack angle

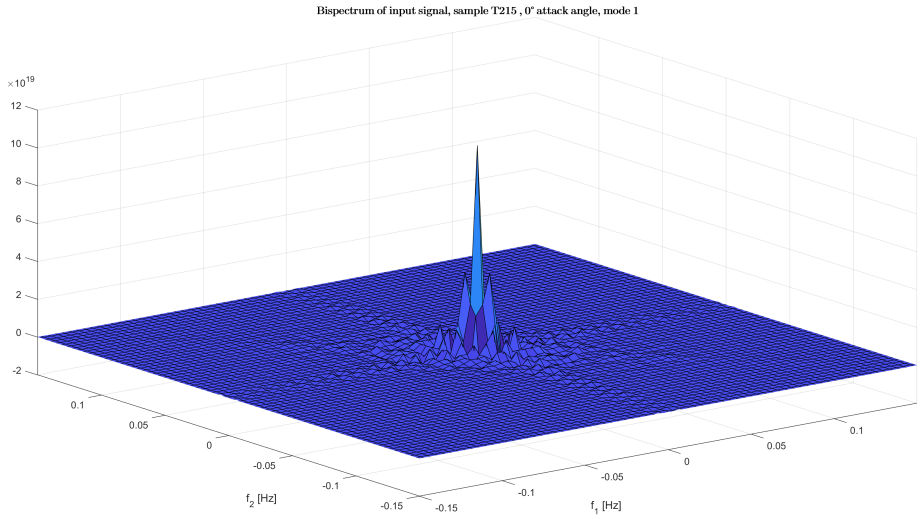

Figure 5.27: Bispectrum of first modal force, sample T215, 0° attack angle.

From figure 5.29 we can see how the analytical and numerical solutions match quite well. Yet, the bispectrum coming from FFT analysis of modal response seems to show slightly higher biresonant peaks.

Increasing the natural modal frequency up to 0.26 Hz, we notice an inversion in the behaviour: the bispectrum coming from the FFT analysis of the modal response shows this time lower biresonant peaks than the ones of both analytical and numerical solutions.

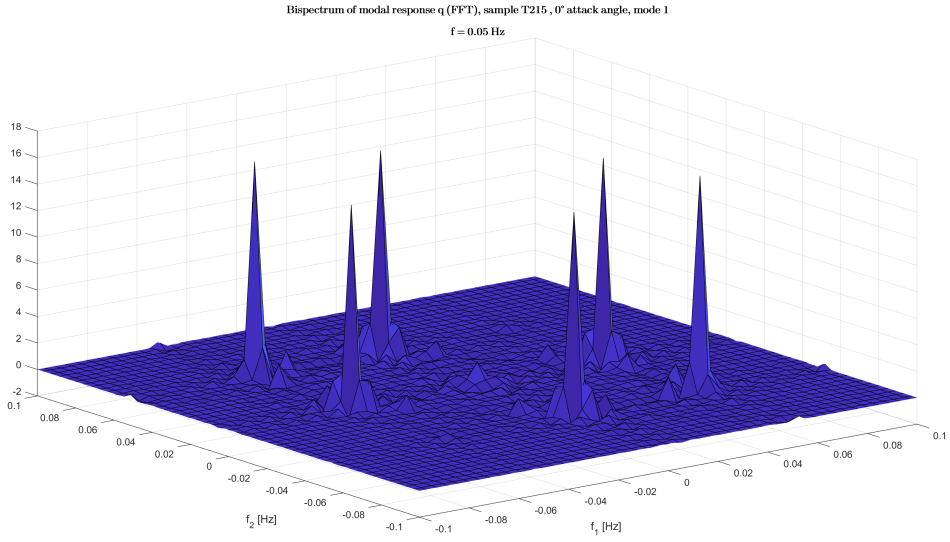

Figure 5.28: Bispectrum of first modal amplitude (FFT), sample T215, 0° attack angle, $f_1 = 0.05$ Hz.

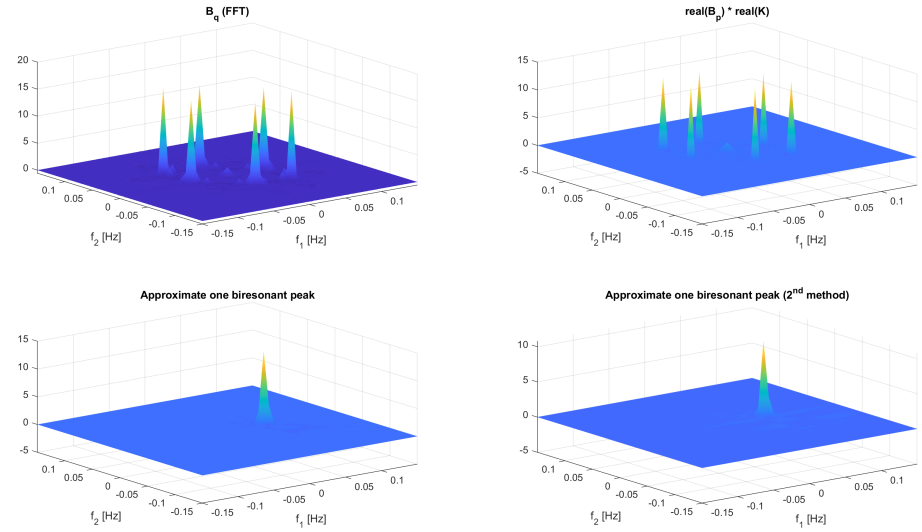

Figure 5.29: Comparison of numerical approximations of Bispectrum of modal response with analytical one, sample T215, 0° attack angle, mode 1, $f_1 = 0.05$ Hz.

Analysing second mode[5], we can notice how both analytical and numerical solutions overestimate the biresonant peaks.

[5]For which we remember Eq B.1, for which we have considered modal frequencies proportional to depth and breadth respectively, in order to better reproduce actual structural behaviour.

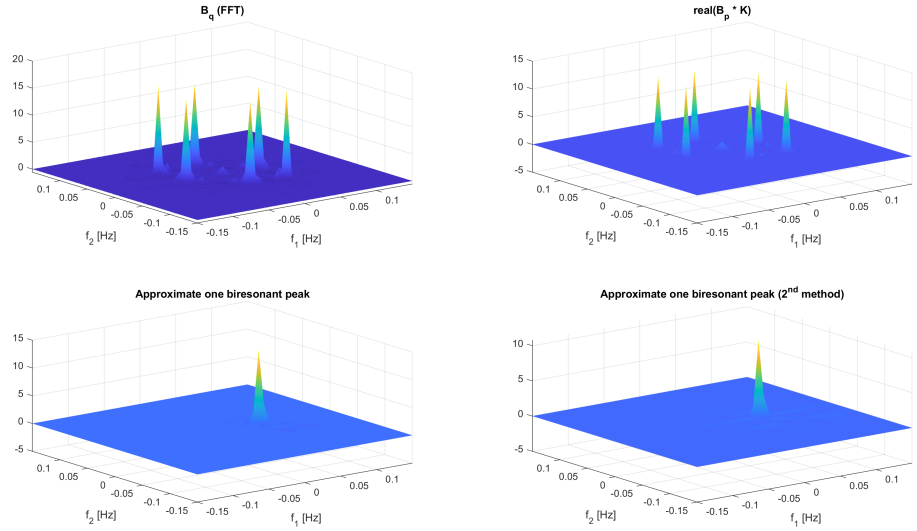

Figure 5.30: Comparison of numerical approximations of Bispectrum of modal response with analytical one (2), sample T215, 0° attack angle, mode 1, $f_1 = 0.05$ Hz.

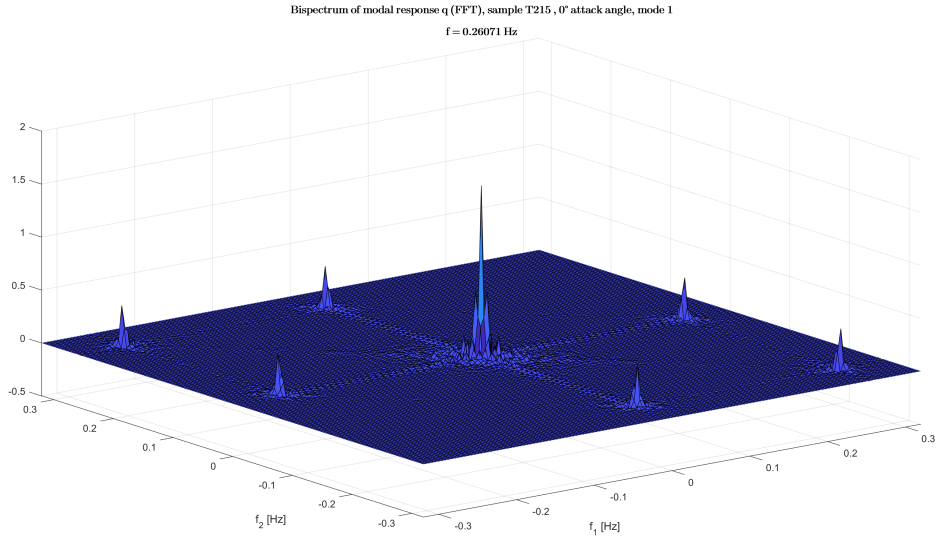

Figure 5.31: Bispectrum of first modal amplitude (FFT), sample T215, 0° attack angle, $f_1 = 0.26$ Hz.

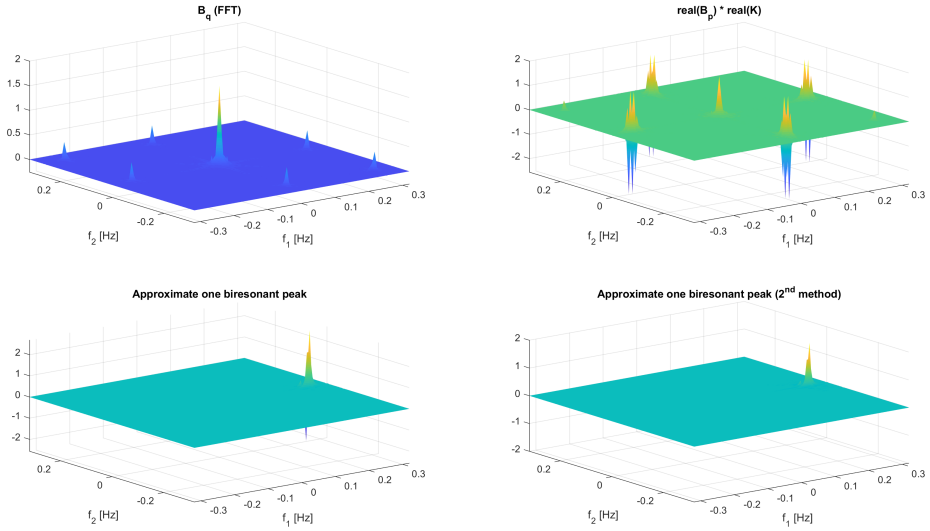

Figure 5.32: Comparison of numerical approximations of Bispectrum of modal response with analytical one, sample T215, 0° attack angle, mode 1, $f_1 = 0.26$ Hz.

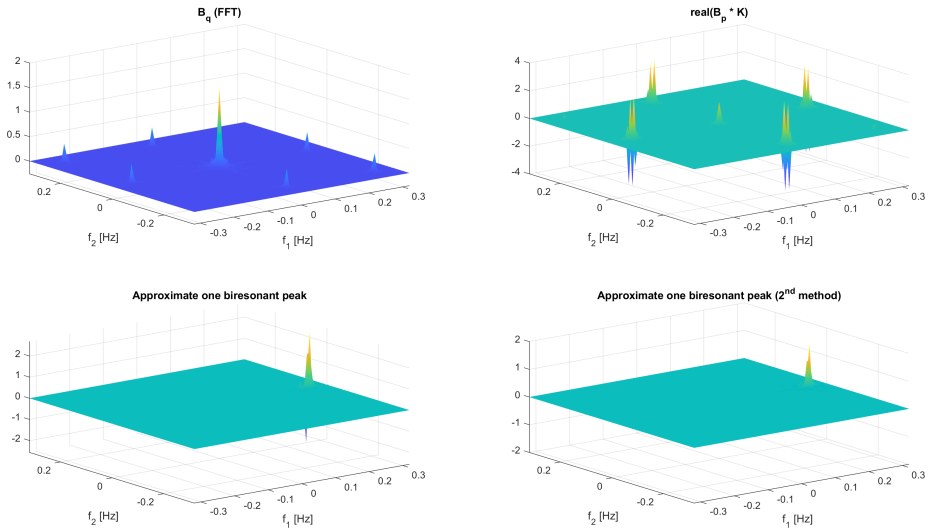

Figure 5.33: Comparison of numerical approximations of Bispectrum of modal response with analytical one (2), sample T215, 0° attack angle, mode 1, $f_1 = 0.26$ Hz.

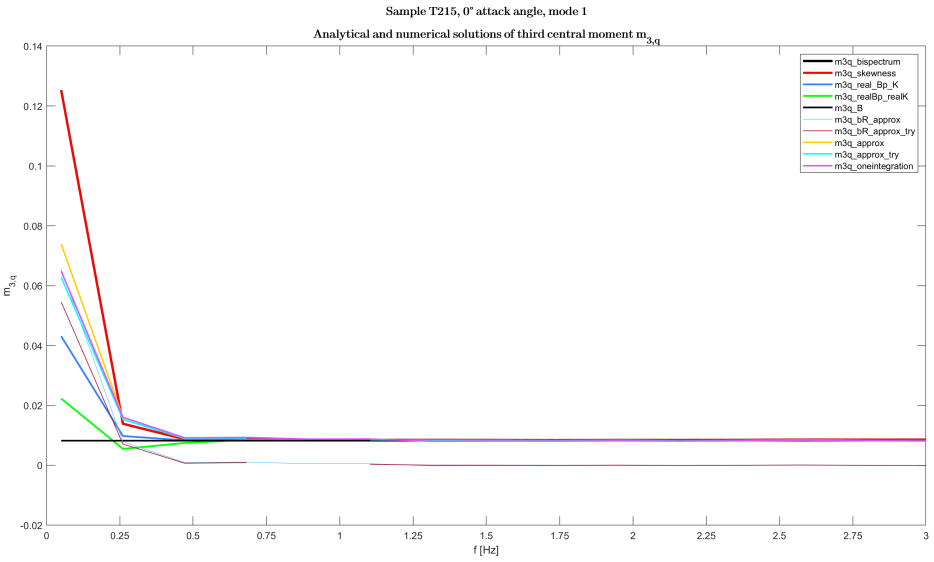

Figure 5.34: Parametric analysis of $m_{3,q}$, mode 1, sample T215, 0° attack angle.

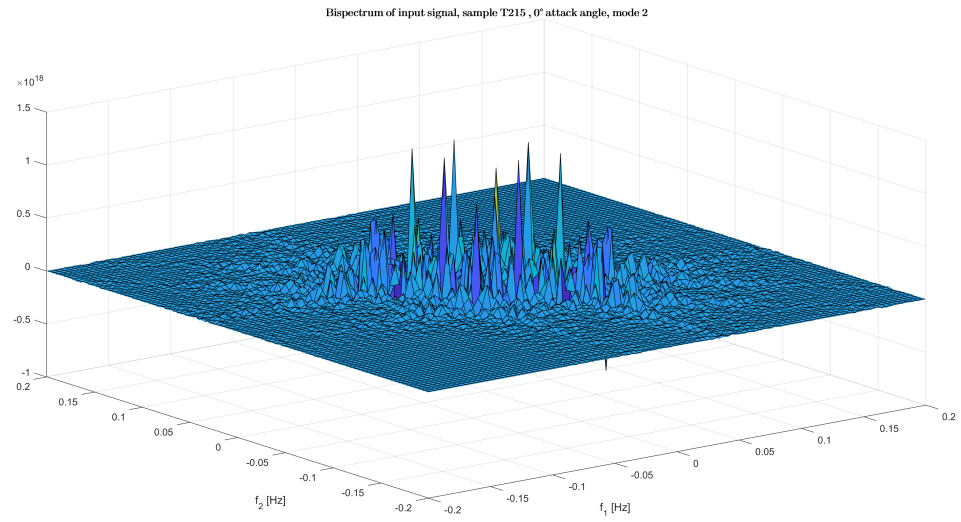

Figure 5.35: Bispectrum of second modal force, sample T215, 0° attack angle.

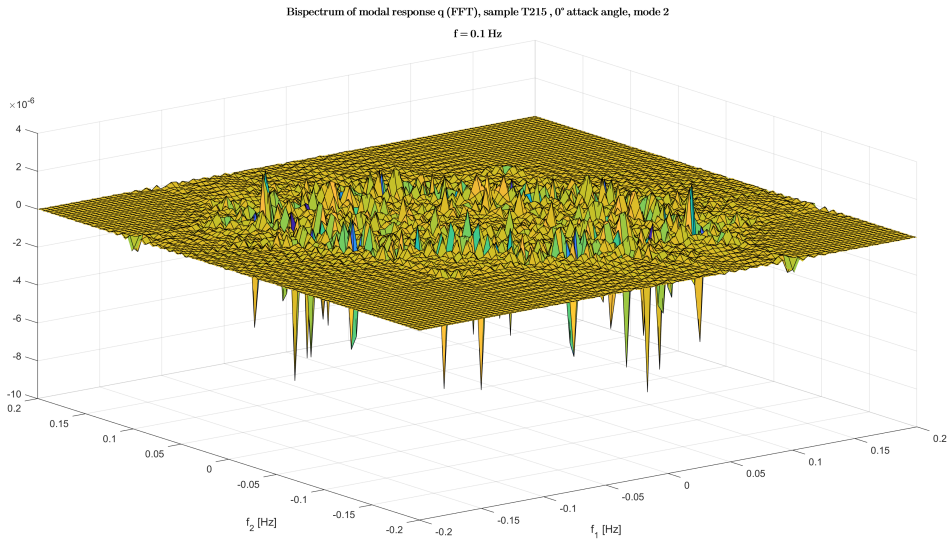

Figure 5.36: Bispectrum of second modal amplitude (FFT), sample T215, 0° attack angle, $f_1 = 0.1$ Hz.

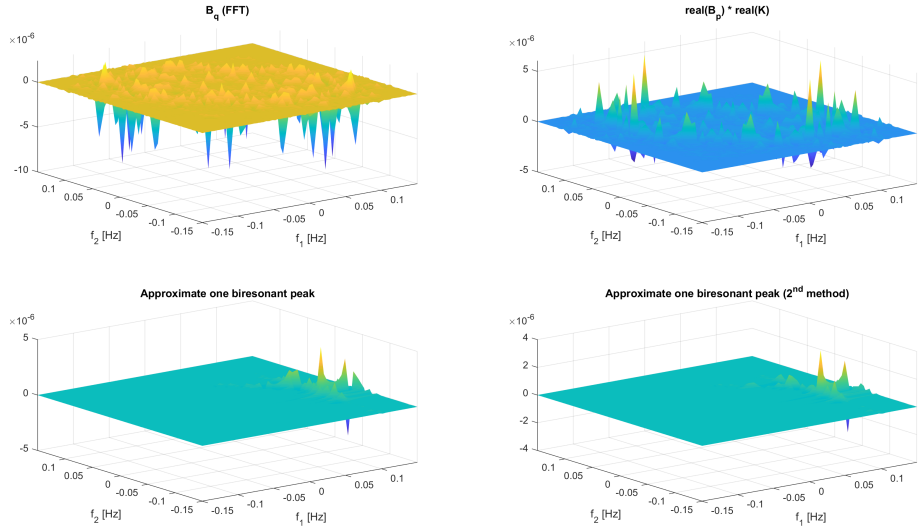

Figure 5.37: Comparison of numerical approximations of Bispectrum of modal response with analytical one, sample T215, 0° attack angle, mode 2, $f_1 = 0.1$ Hz.

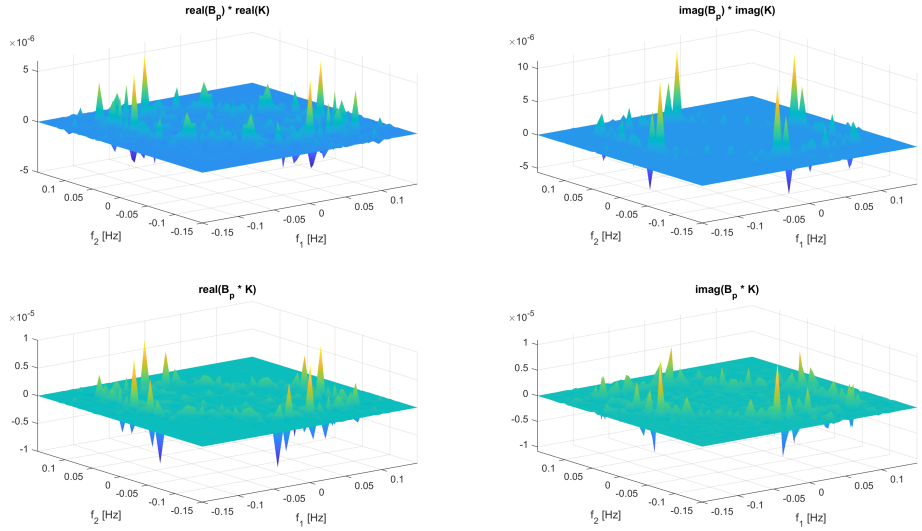

Figure 5.38: Imaginary and real parts of Bq computed analytically, sample T215, 0° attack angle, mode 2, $f_2 = 0.1$ Hz.

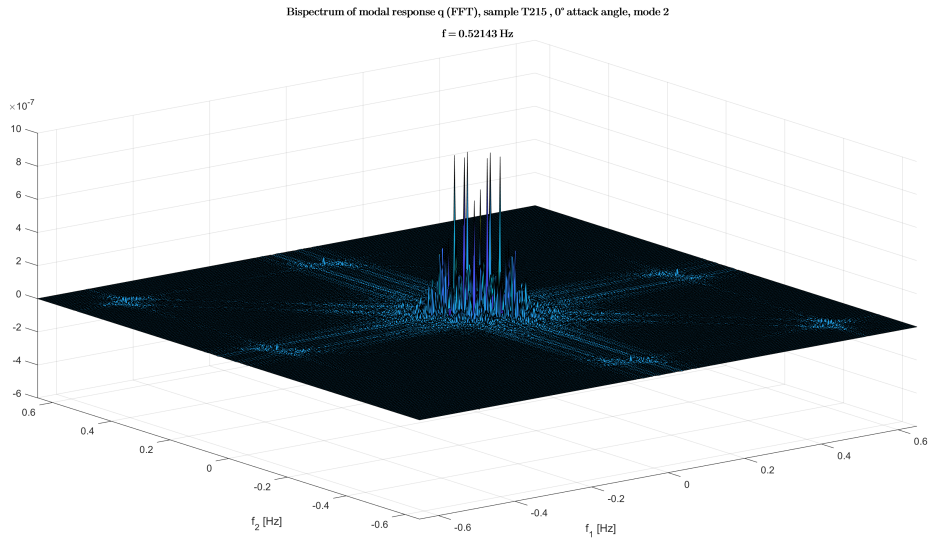

Figure 5.39: Bispectrum of second modal amplitude (FFT), sample T215, 0° attack angle, $f_1 = 0.52$ Hz.

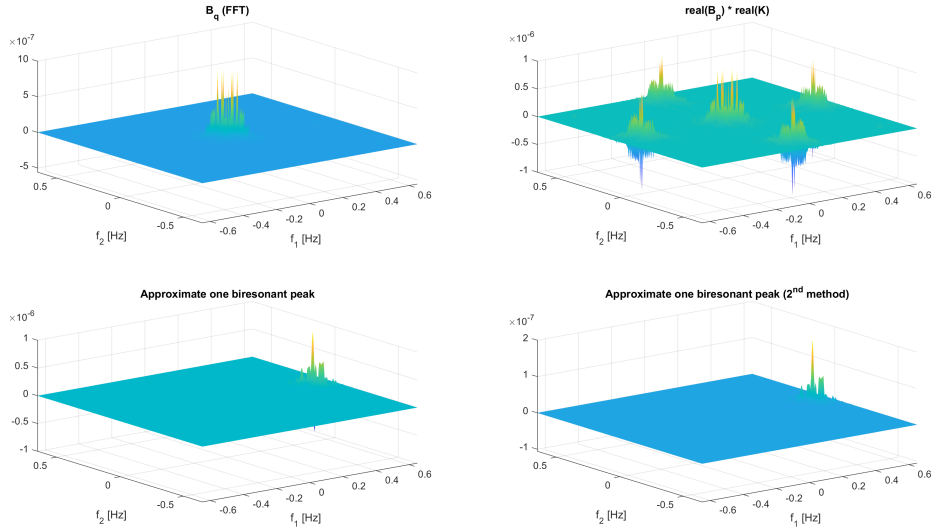

Figure 5.40: Comparison of numerical approximations of Bispectrum of modal response with analytical one, sample T215, 0° attack angle, mode 2, $f_1 = 0.52$ Hz.

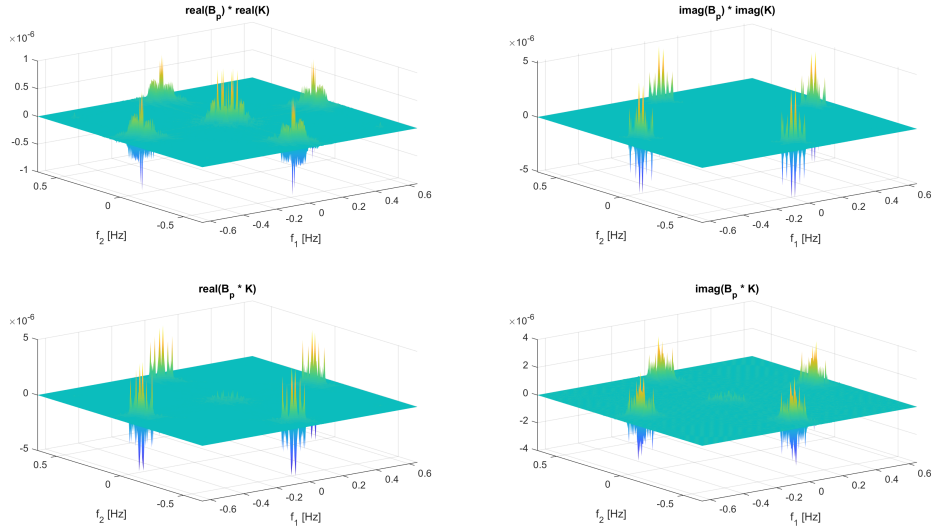

Figure 5.41: Imaginary and real parts of Bq computed analytically, sample T215, 0° attack angle, mode 2, $f_2 = 0.52$ Hz.

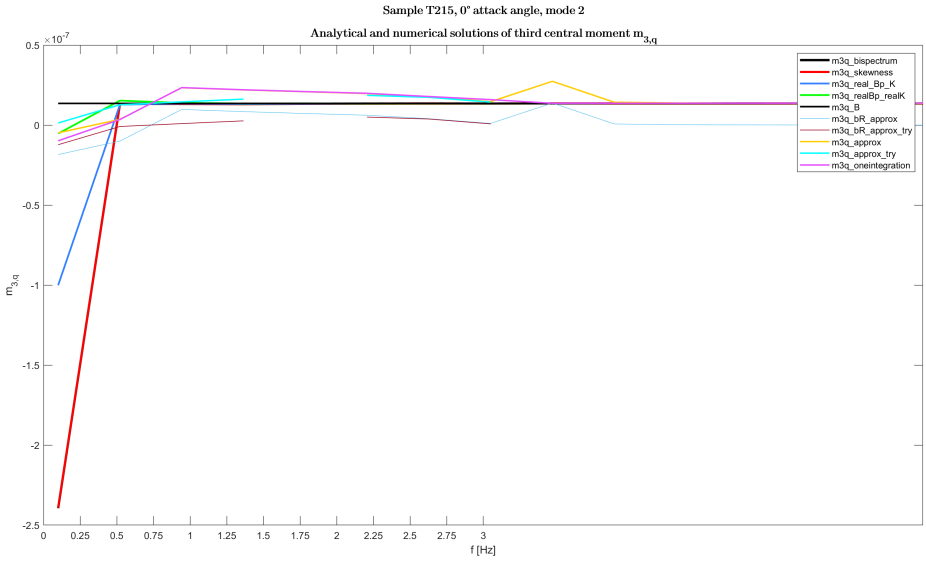

Figure 5.42: Parametric analysis of $m_{3,q}$, mode 2, sample T215, 0° attack angle.

6 Conclusions

The main objective of this Work was to provide a faster as accurate method to evaluate dynamic response of a structural system. Classic approach is based on Fourier Analysis, which consist in analysing time history of loading by computing its frequency content (Direct Fourier Transform), applying complex transfer function (which depends on structural parameters only) obtaining the response in the frequency domain, then time history of response is recovered by means of Inverse Fourier Transform. However, this is highly costly when it comes to structural systems with many degrees of freedom. In this framework, specially when it comes to early stages of a civil engineering project, a more efficient analysis would be preferred.

That is what this Thesis is aim at. We tried to prove that structural response can be quite well reproduced even avoiding that time expensive procedure of the Fourier Analysis, by just relating it to statistical quantities of the loading. Yet, at the costs of something: in fact, with this approach it not possible to recover time histories of the response. However, this can be considered as a minor downside since specially for design purposes the most important and significant quantities are represented by extreme values (max displacement, velocity, acceleration, deflection etc.).

Therefore, in a first instance we showed how response can be very well reproduced by its Background and Resonant decomposition. Once validation was proved, we were then able to build response spectra by means of parametric analysis, in which we made structural parameters (i.e. natural modal frequencies, damping etc.) varying such to evaluate how response was affected by a changing of them. To make it clear the advantage in cost efficiency with respect to conventional method, B&R decomposition is of order 2×10^2 faster than FFT. This means for example, that if B&R computes response in 1 hour, FFT would need 200 hours for computing the response of the same configuration (that is more than one week!).

However, the background and resonant decomposition of the response can be applied only under the assumption that loading has a Gaussian distribution of the probability density function. Once gaussianity is lost, this decomposition causes underestimation of the response (non-conservative), in terms of the peak factor g used to recover the response.

Therefore, we finally tried to extend this approach to a higher order, such to better characterise the loading considering its non-gaussianity. The idea was anyway based on the same principle: decomposing the response in its two major components, a background accounting for the quasi-static behaviour, and a biresonant. Everything has been brought into the frequency space, building 3-D surfaces, namely the bispectrum.

However, contrarily as verified for the case in which loading was Gaussian, increasing the order of analysis has brought some more instability in the accuracy of the approximation of the response. Yet, it has to be noted that in this case actual response was

not recovered explicitly: we just focused on its application to the evaluation of the third statistical moment of the response (which is then used in the computation of the peak factor g, by its own then used to compute response). Still, it has been shown that actual outcome is influenced by many factors, as for instance the refinement of the mesh of the modal forces, used by their side to compute analytical and numerical solutions.

Finally we can conclude saying that overall the approach is physically admissible, since it shows the expected behaviour in terms of both background and biresonant peaks, which occur at the right points in the frequency space. However, it needs to be further exploited in order to better understand and consequently reproduce local behaviour, specially at low frequency for which resonance effects play an important role.

Acknowledgements

This step represent the end of a tough but joyful path which its ending is the result of the work in which many people have flanked me in different ways and times that I would like to thank, among whom Vincent Denoël that has distinguished for its professionalism and humanity with which he has contributed at the writing of this Paper.

A B&R responses: numerical comparison

Sample T215, 0° attack angle

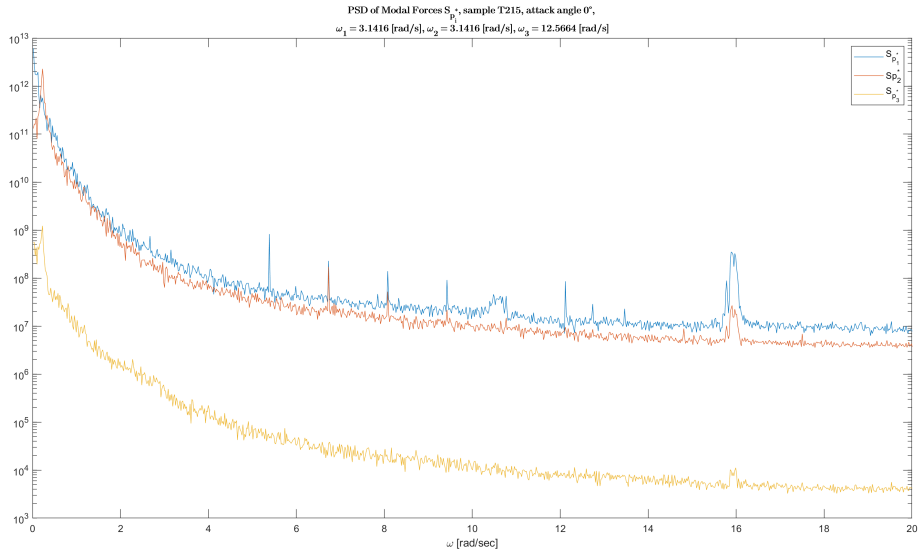

Figure A.1: Plot of PSDs of Modal Forces, sample T215, 0° attack angle (log scale).

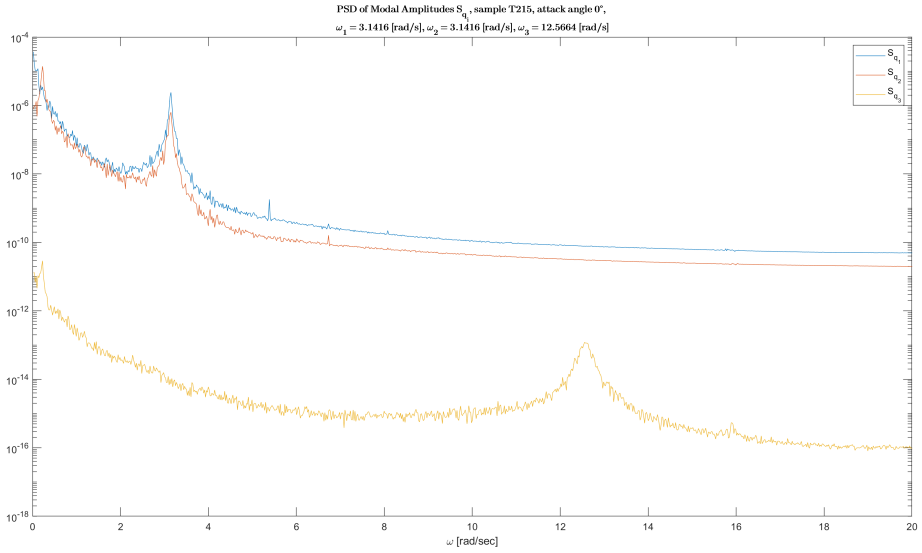

Figure A.2: Plot of PSDs of Modal Amplitudes, sample T215, 0° attack angle (log scale).

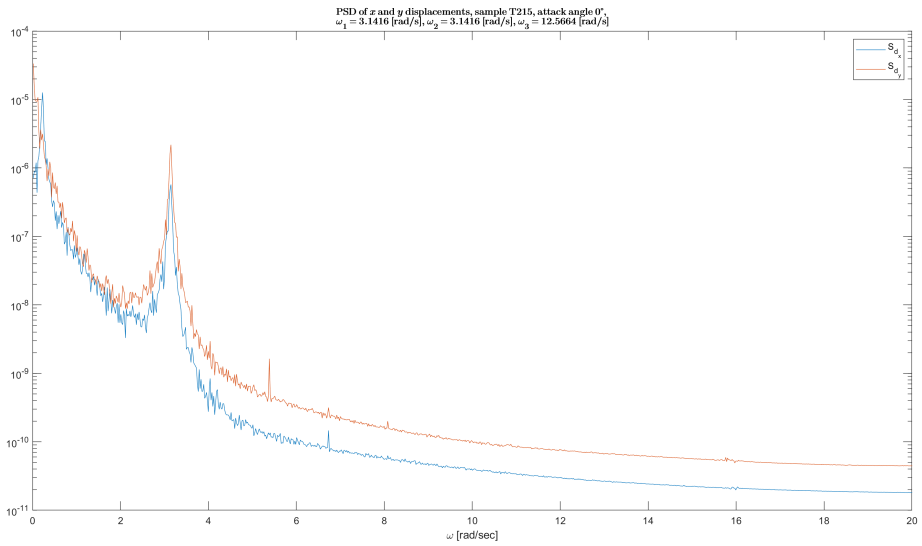

Figure A.3: Plot of PSDs of$x$ and y displacements of UL element on W surface, sample T215, 0° attack angle (log scale).

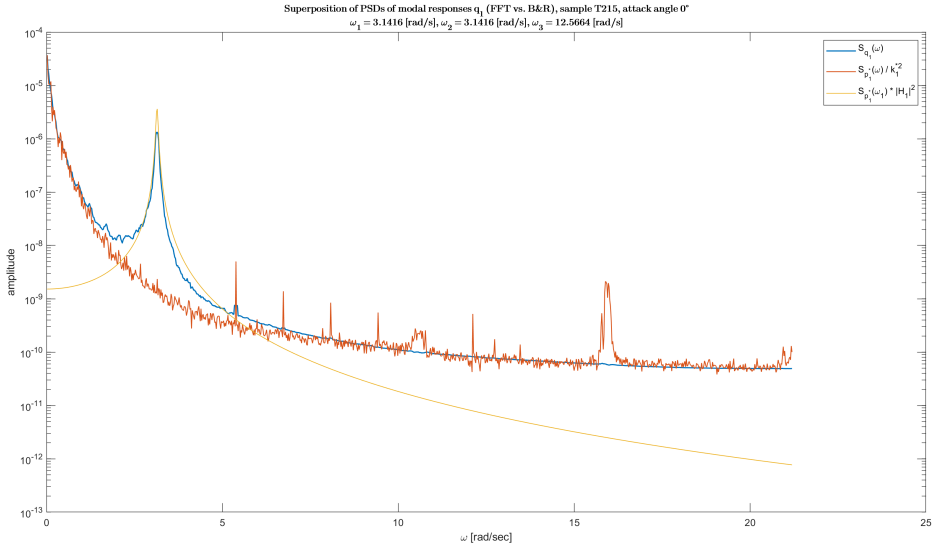

Figure A.4: Superposition of FFT and B&R modal responses for Mode 1, sample T215, 0° attack angle (log scale).

Sample T315, 0° attack angle

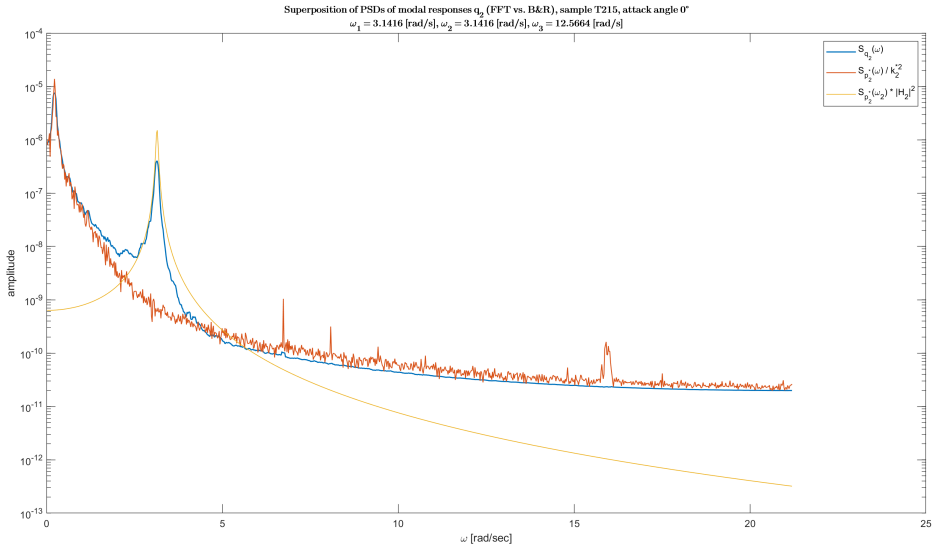

Figure A.5: Superposition of FFT and B&R modal responses for Mode 2, sample T215, 0° attack angle (log scale).

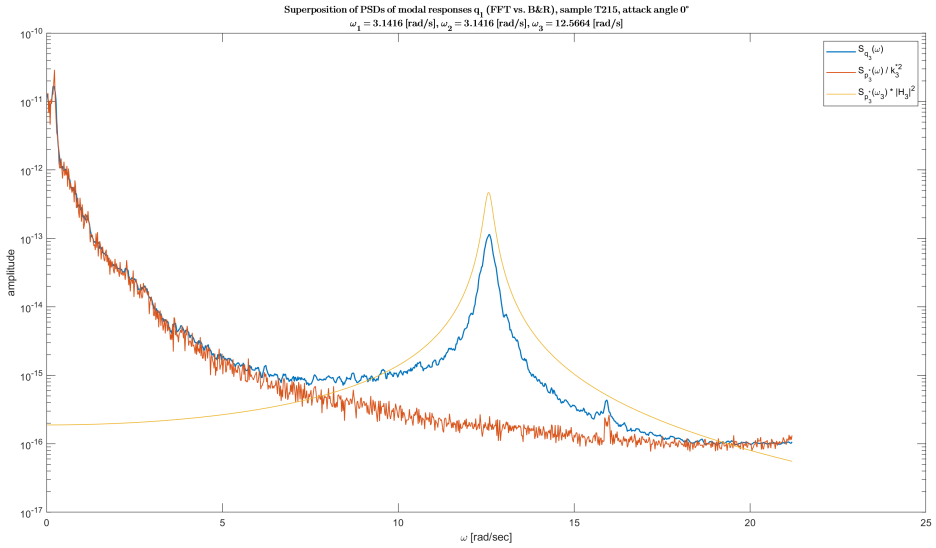

Figure A.6: Superposition of FFT and B&R modal responses for Mode 3, sample T215, 0° attack angle (log scale).

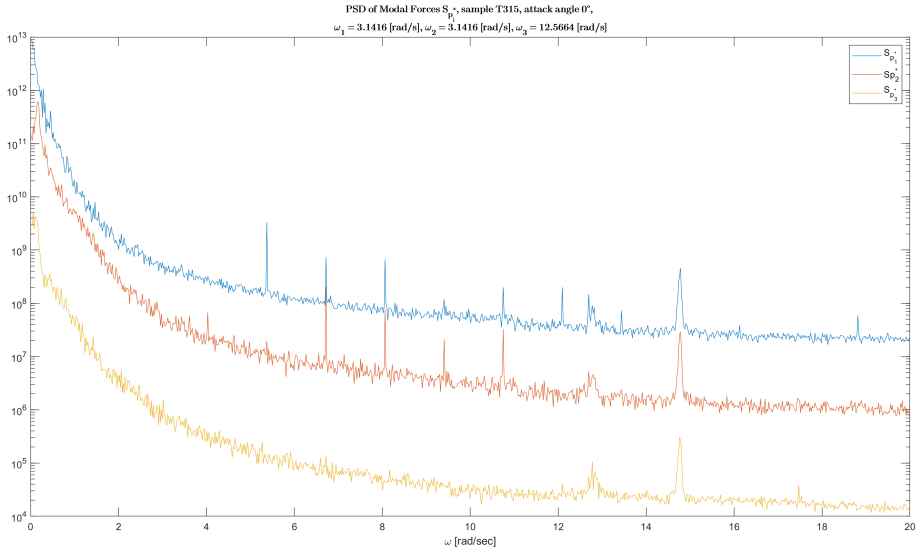

Figure A.7: Plot of PSDs of Modal Forces, sample T315, 0° attack angle (log scale).

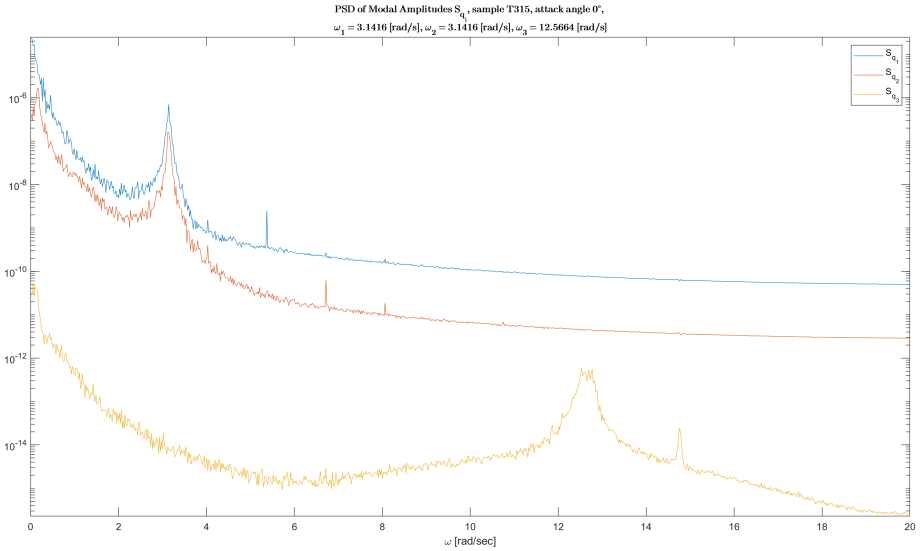

Figure A.8: Plot of PSDs of Modal Amplitudes, sample T315, 0° attack angle (log scale).

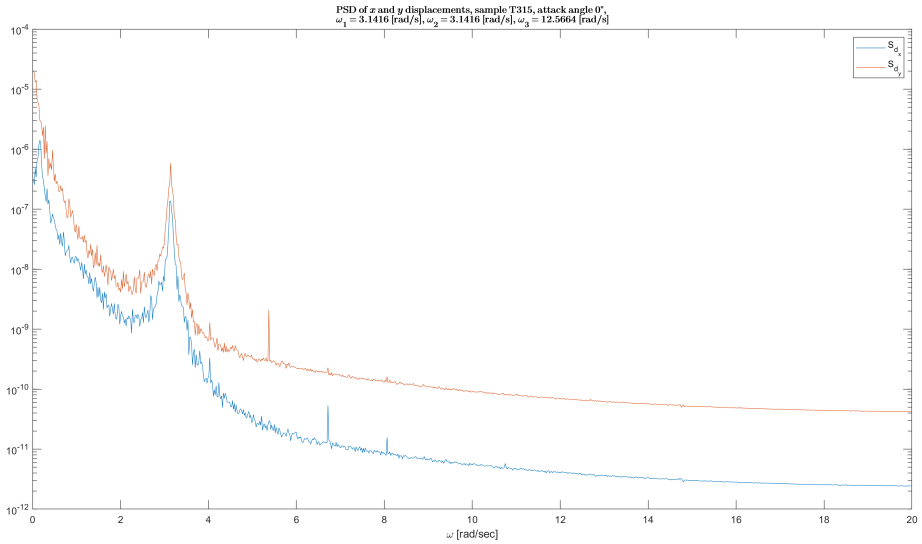

Figure A.9: Plot of PSDs of$x$ and y displacements of UL element on W surface, sample T315, 0° attack angle (log scale).

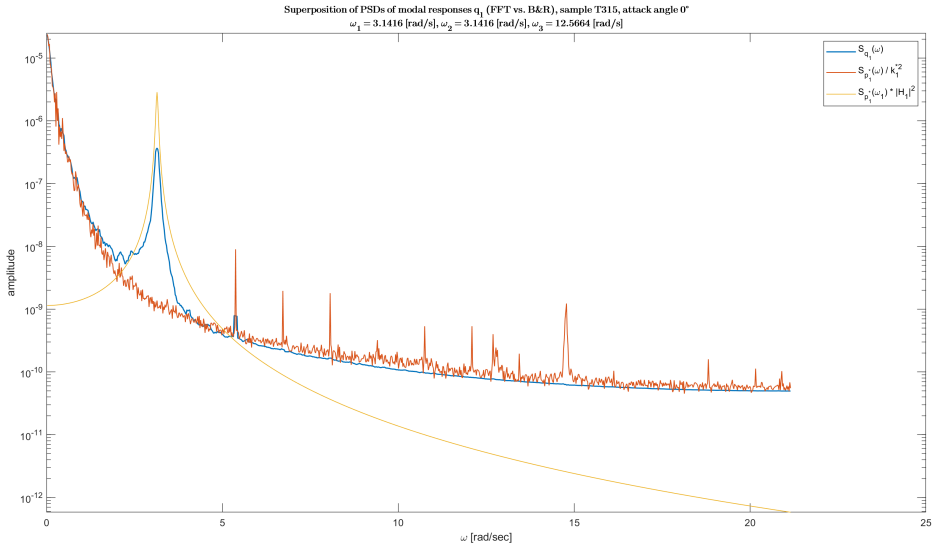

Figure A.10: Superposition of FFT and B&R modal responses for Mode 1, sample T315, 0° attack angle (log scale).

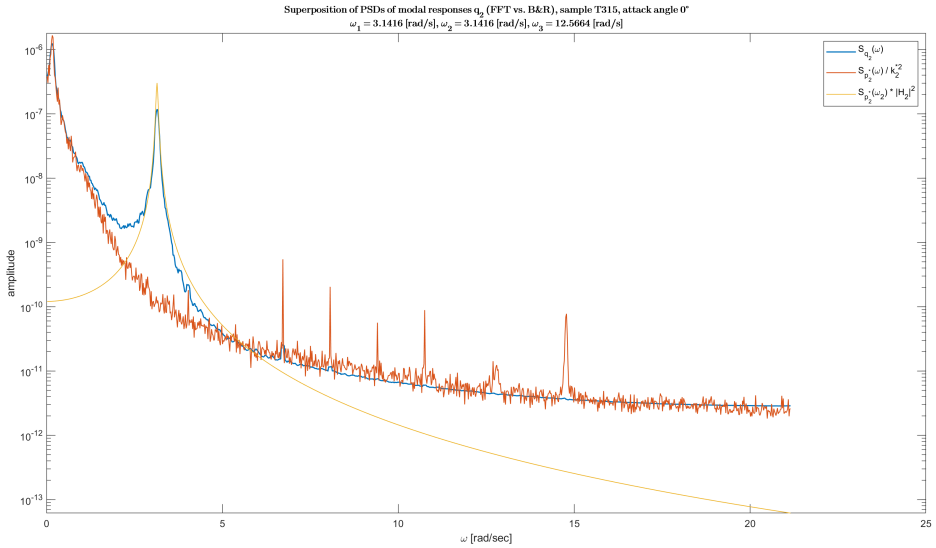

Figure A.11: Superposition of FFT and B&R modal responses for Mode 2, sample T315, 0° attack angle (log scale).

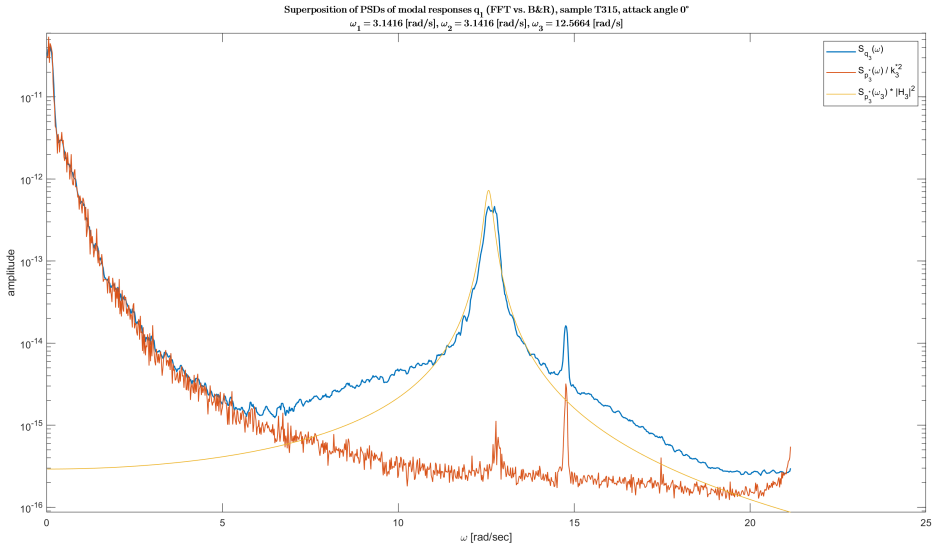

Figure A.12: Superposition of FFT and B&R modal responses for Mode 3, sample T315, 0° attack angle (log scale).

B B&R decomposition: response spectra

Following spectra coming from B&R decomposition of the response are reported.

NOTE: in the unsymmetrical samples (i.e. T21x and T31x), natural modal frequencies of the second mode (hence, displacements along x direction, which is parallel to the breadth b of the structure) have been taken as

$$\overline{\omega_2} = b * \overline{\omega_1} \tag{B.1}$$

where b is the breadth (in model scale), in order to better model the fact that in second mode structure is displaced along its longest dimension (i.e. having higher stiffness).

Sample T215, 0° attack angle

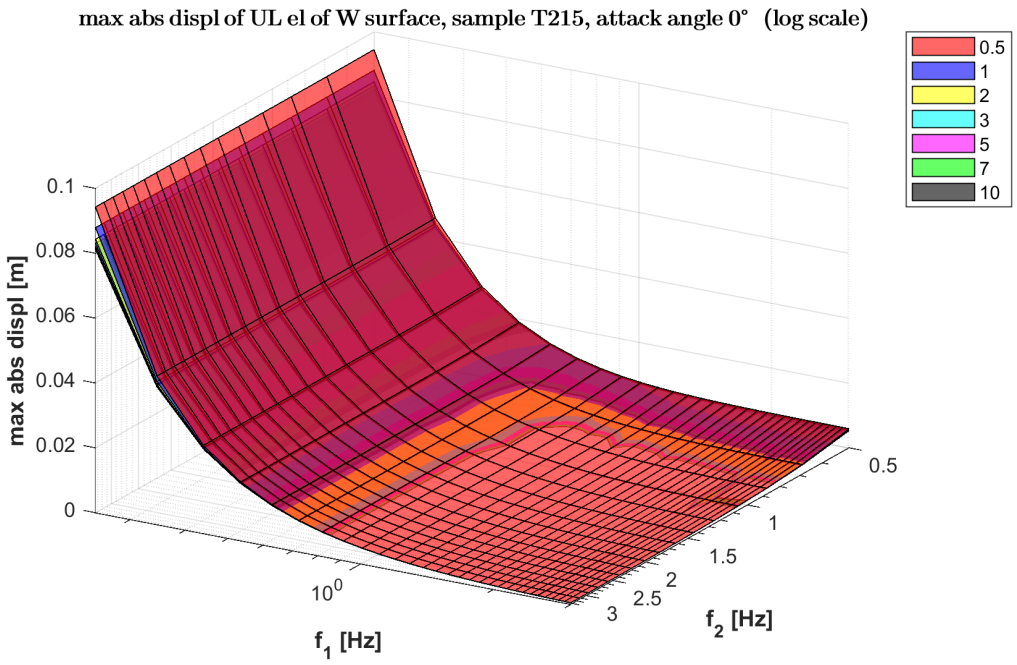

Figure B.1: Response spectra of absolute displacement of UL element on W surface (log scale), sample T215, 0° attack angle.

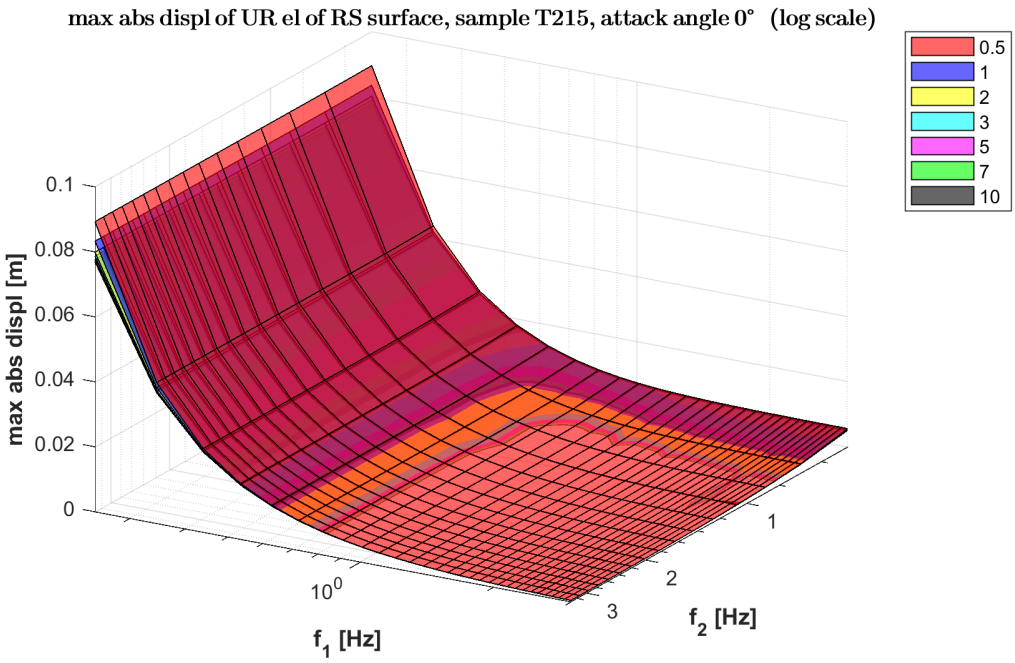

Figure B.2: Response spectra of absolute displacement of UR element on RS surface (log scale), sample T215, 0° attack angle.

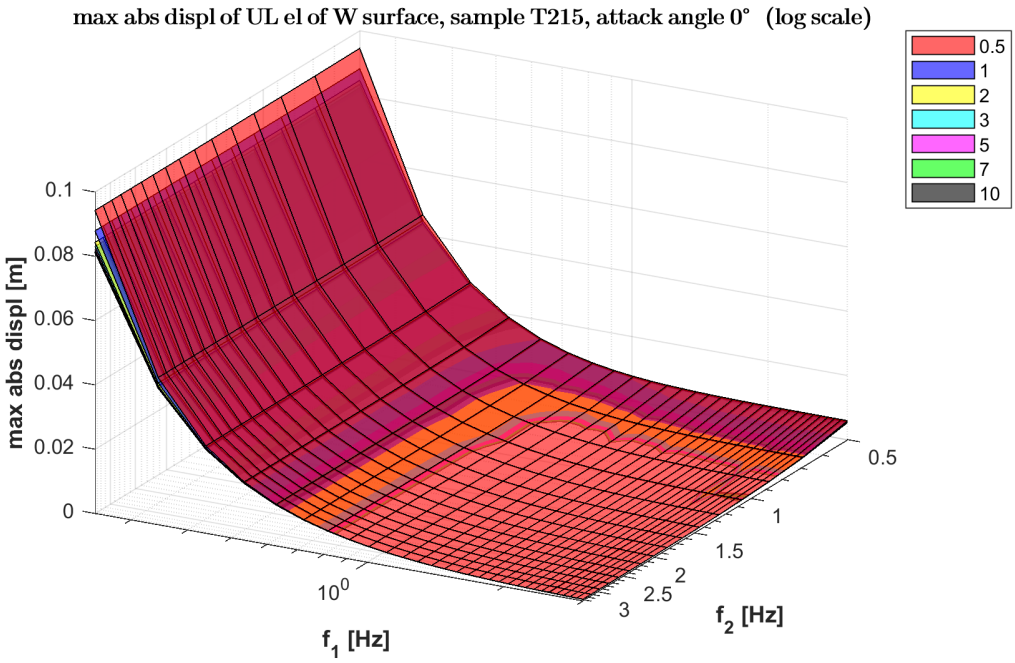

Figure B.3: Response spectra of absolute displacement of UL element on LS surface (log scale), sample T215, 0° attack angle.

Sample T215, 45° attack angle

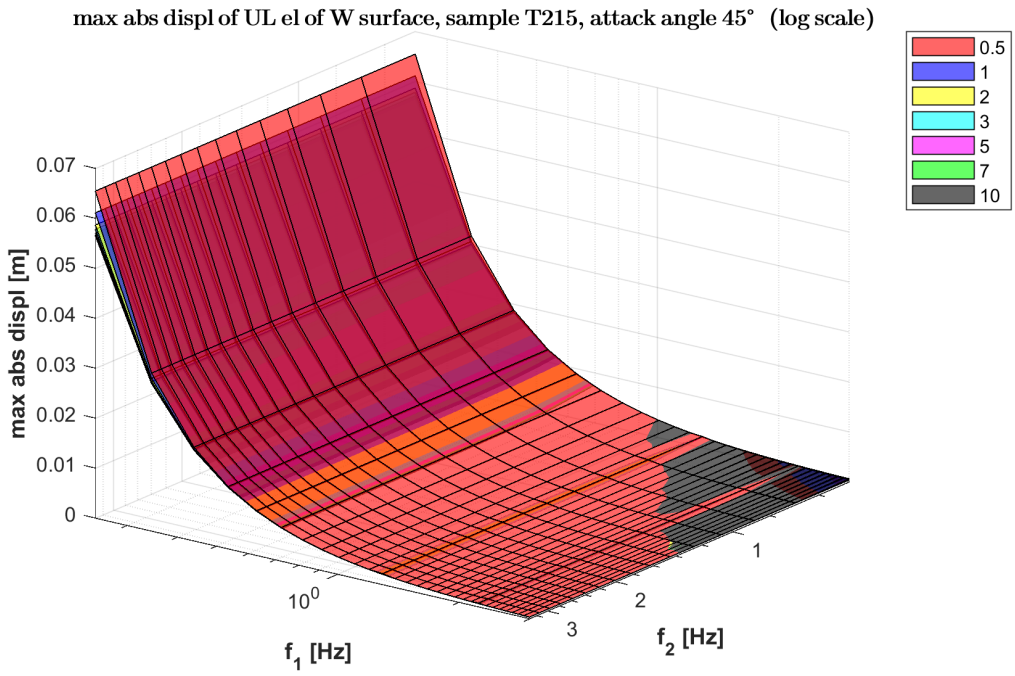

Figure B.4: Response spectra of absolute displacement of UL element on W surface (log scale), sample T215, 45° attack angle.

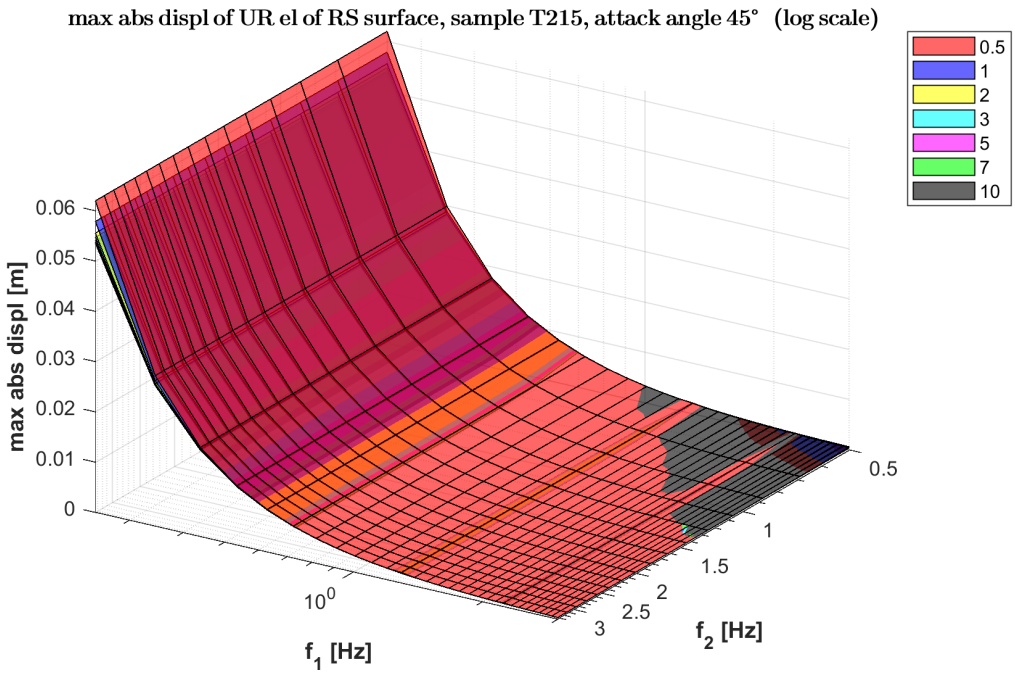

Figure B.5: Response spectra of absolute displacement of UR element on RS surface (log scale), sample T215, 45° attack angle.

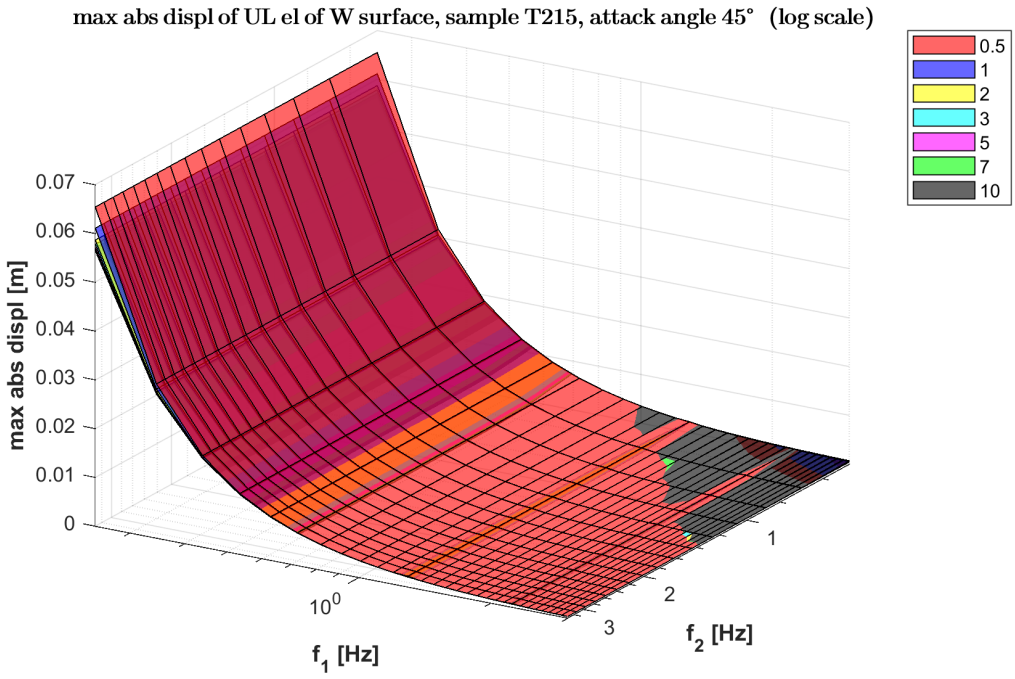

Figure B.6: Response spectra of absolute displacement of UL element on LS surface (log scale), sample T215, 45° attack angle.

Sample T215, 90° attack angle

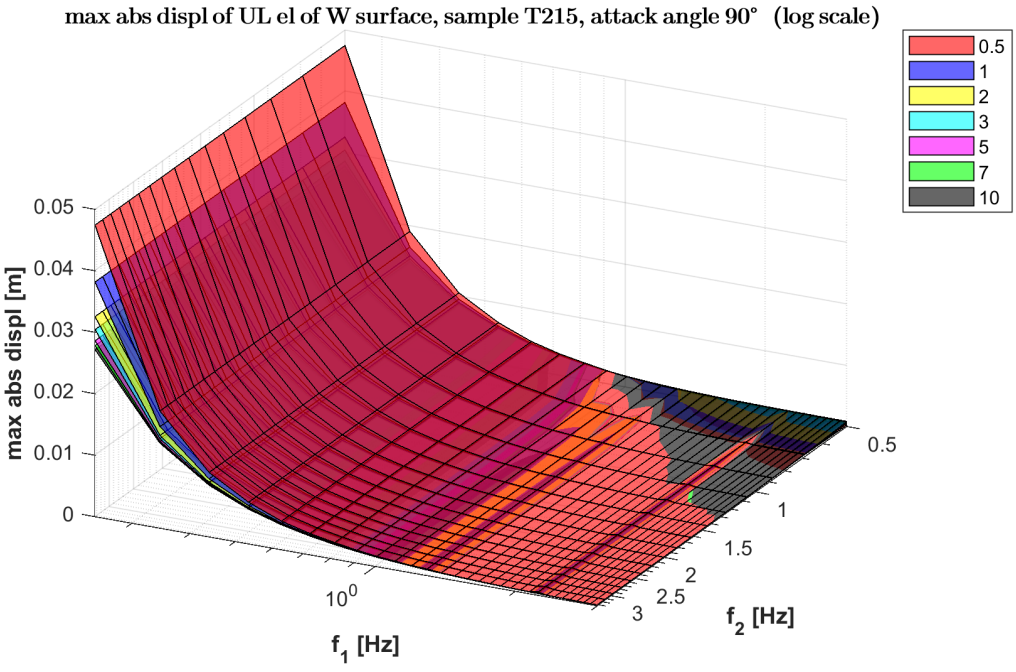

Figure B.7: Response spectra of absolute displacement of UL element on W surface (log scale), sample T215, 90° attack angle.

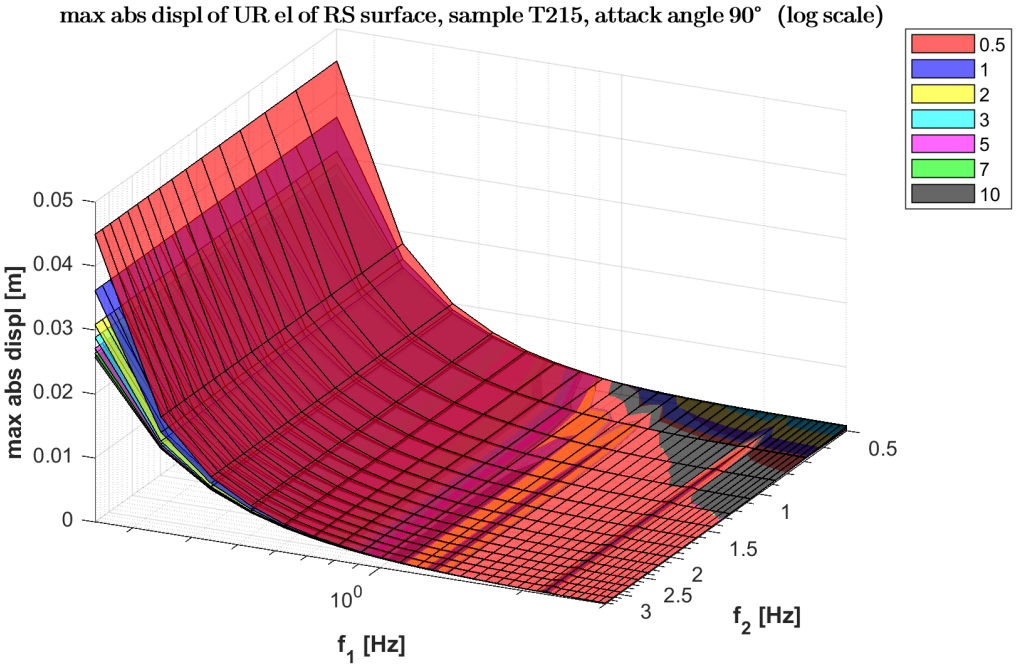

Figure B.8: Response spectra of absolute displacement of UR element on RS surface (log scale), sample T215, 90° attack angle.

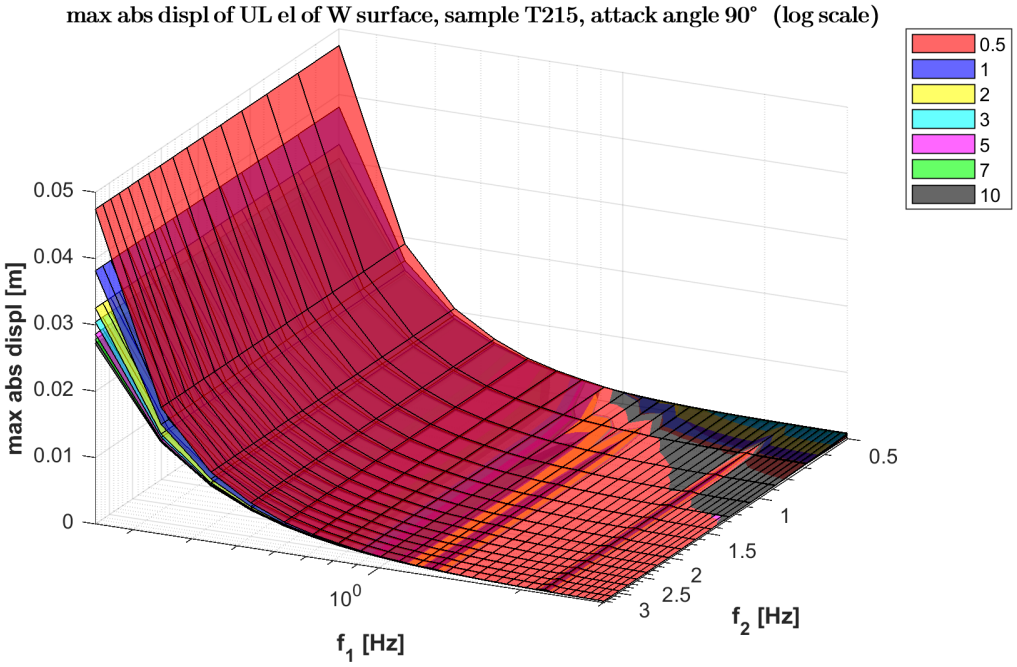

Figure B.9: Response spectra of absolute displacement of UL element on LS surface (log scale), sample T215, 90° attack angle.

Sample T315, 0° attack angle

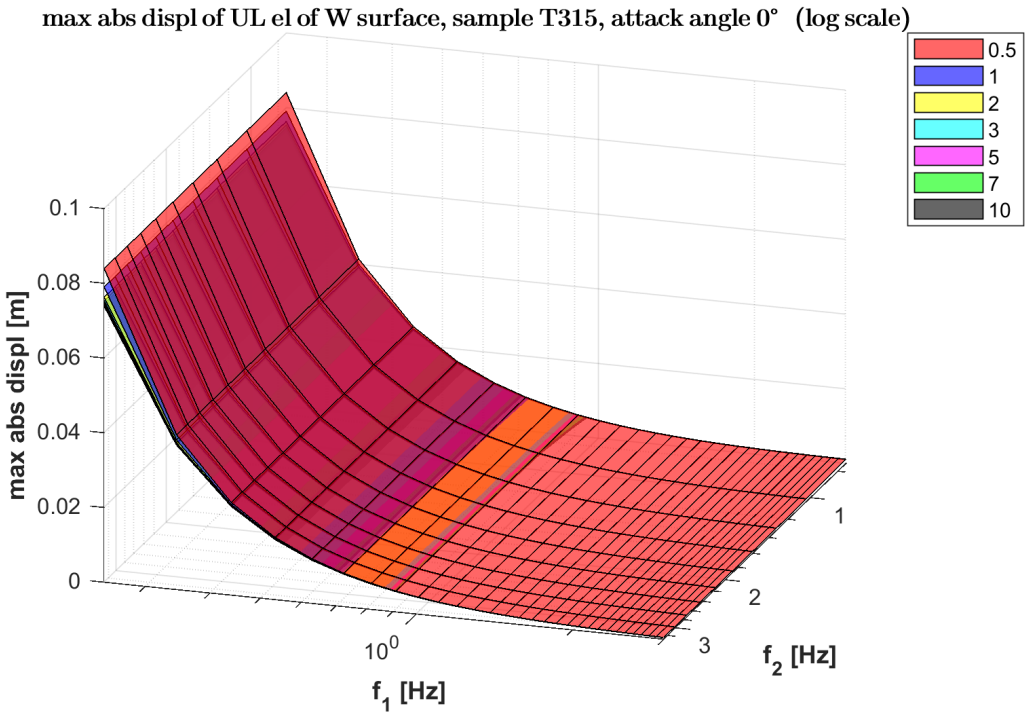

Figure B.10: Response spectra of absolute displacement of UL element on W surface (log scale), sample T315, 0° attack angle.

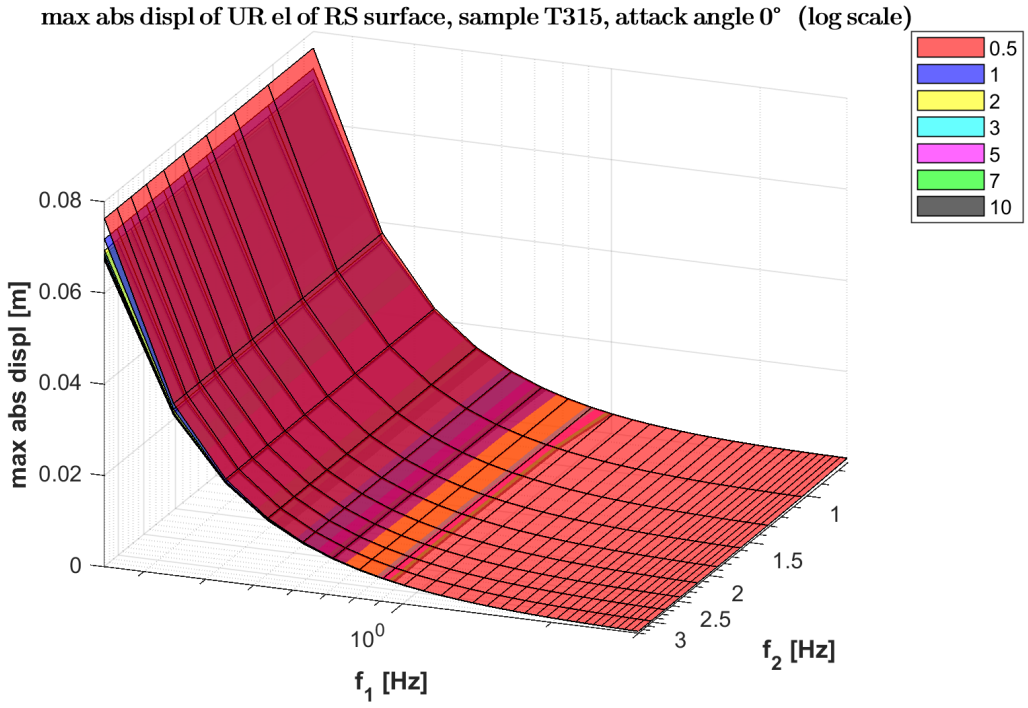

Figure B.11: Response spectra of absolute displacement of UR element on RS surface (log scale), sample T315, 0° attack angle.

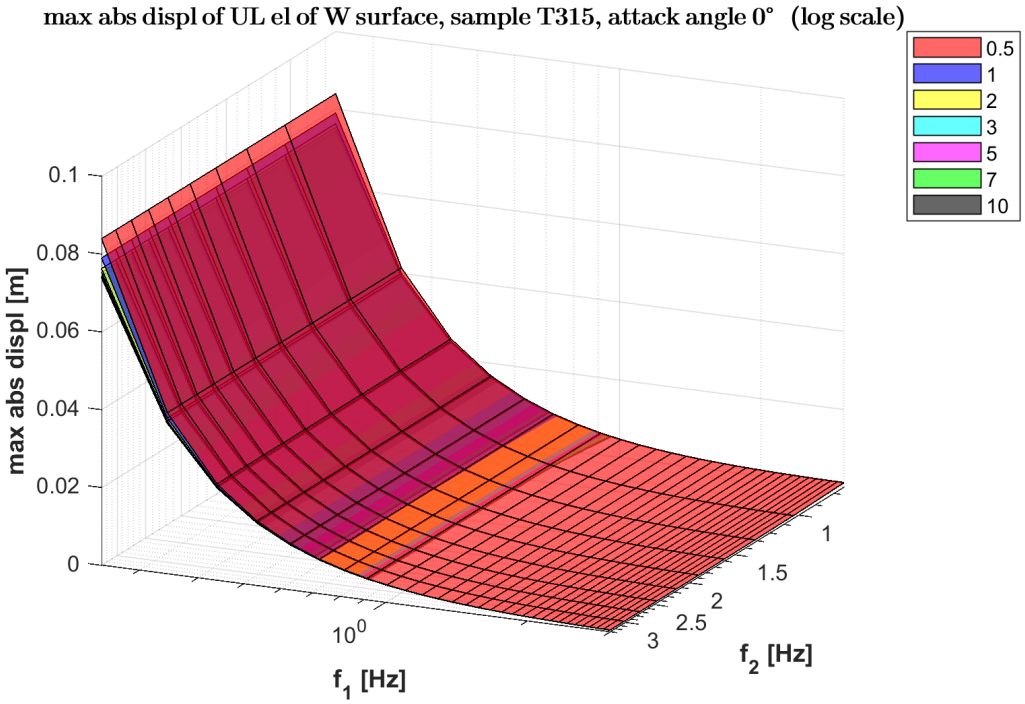

Figure B.12: Response spectra of absolute displacement of UL element on LS surface (log scale), sample T315, 0° attack angle.

C Background and Biresonant decomposition

C.1 Sample T315, 0° attack angle

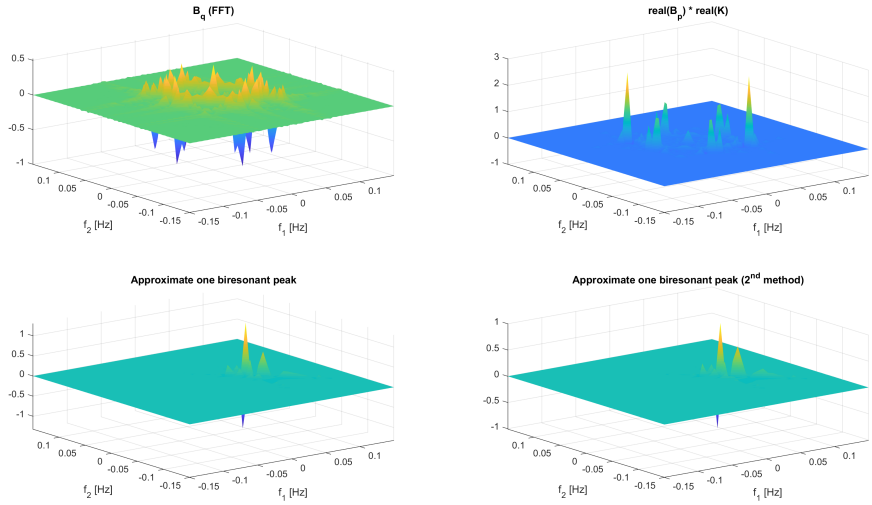

Figure C.1: Comparison of numerical approximations of Bispectrum of modal response with analytical one, sample T315, 0° attack angle, mode 1, $f_1 = 0.05$ Hz.

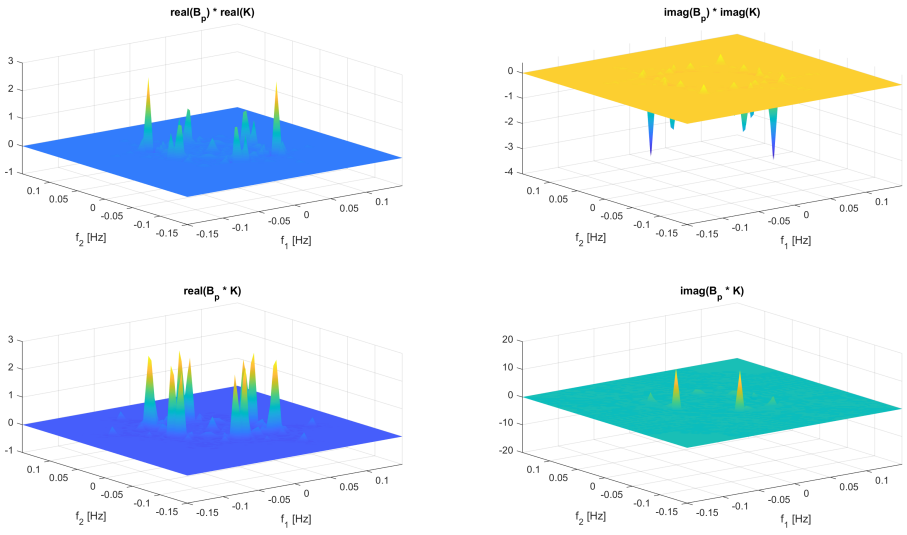

Figure C.2: Imaginary and real parts of Bq computed analytically, sample T315, 0° attack angle, mode 1, $f_2 = 0.05$ Hz.

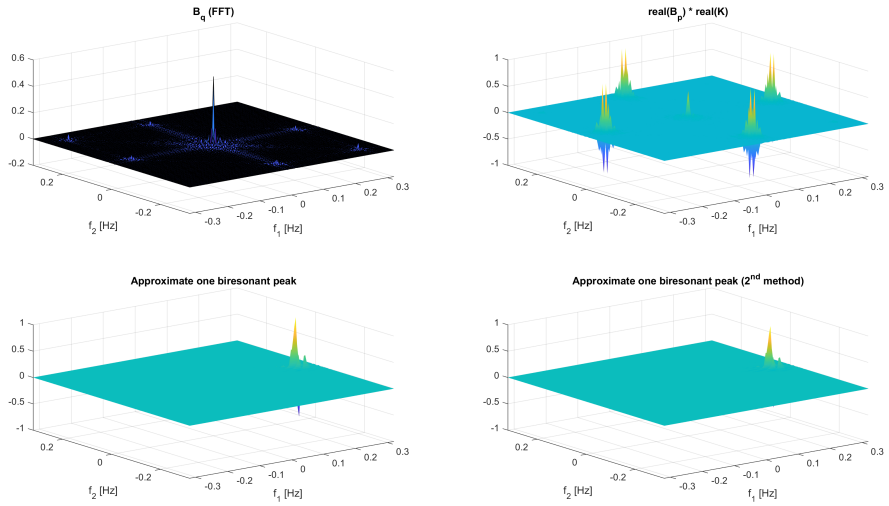

Figure C.3: Comparison of numerical approximations of Bispectrum of modal response with analytical one, sample T315, 0° attack angle, mode 1, $f_1 = 0.26$ Hz.

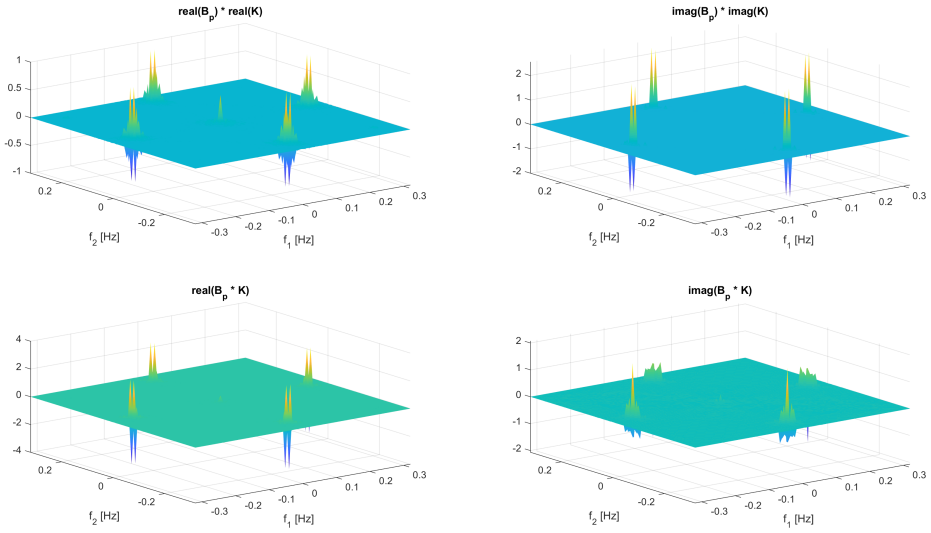

Figure C.4: Imaginary and real parts of Bq computed analytically, sample T315, 0° attack angle, mode 1, $f_2 = 0.26$ Hz.

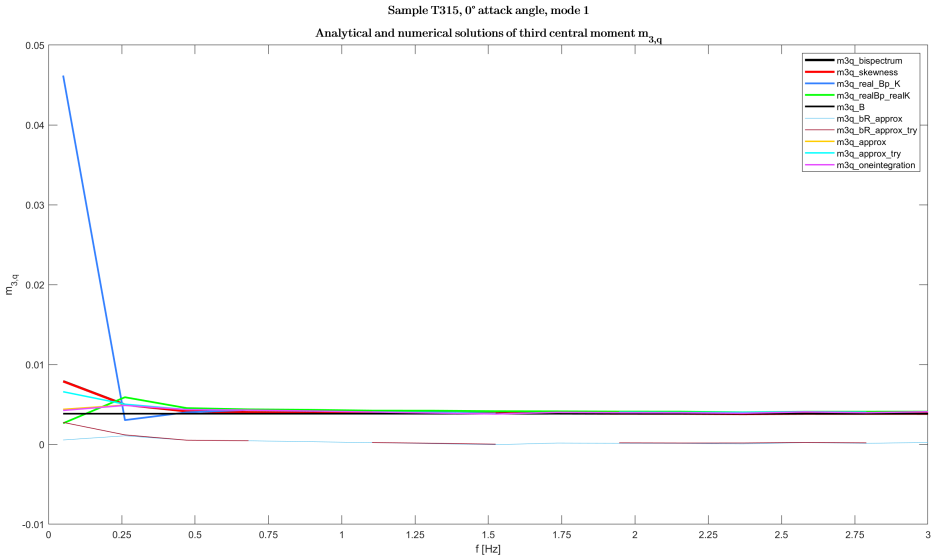

Figure C.5: Parametric analysis of $m_{3,q}$, mode 1, sample T315, 0° attack angle.

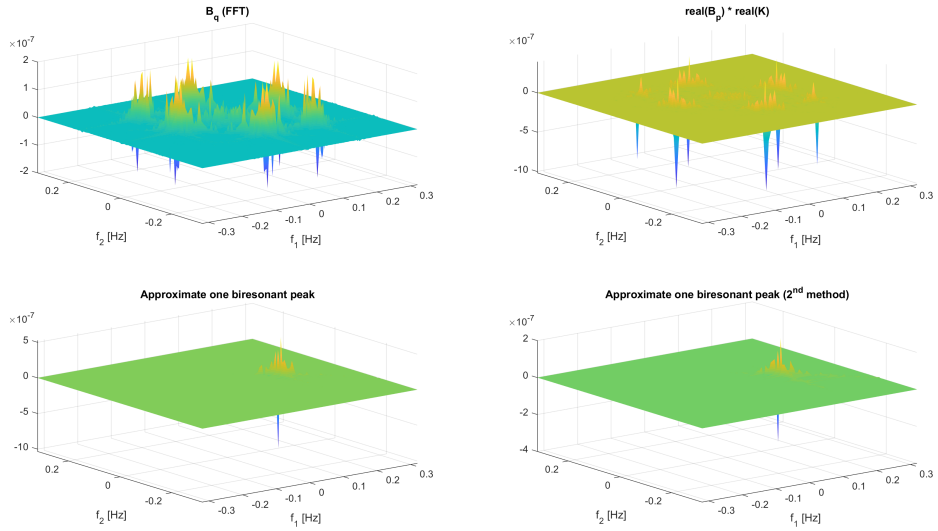

Figure C.6: Comparison of numerical approximations of Bispectrum of modal response with analytical one, sample T315, 0° attack angle, mode 2, $f_1 = 0.15$ Hz.

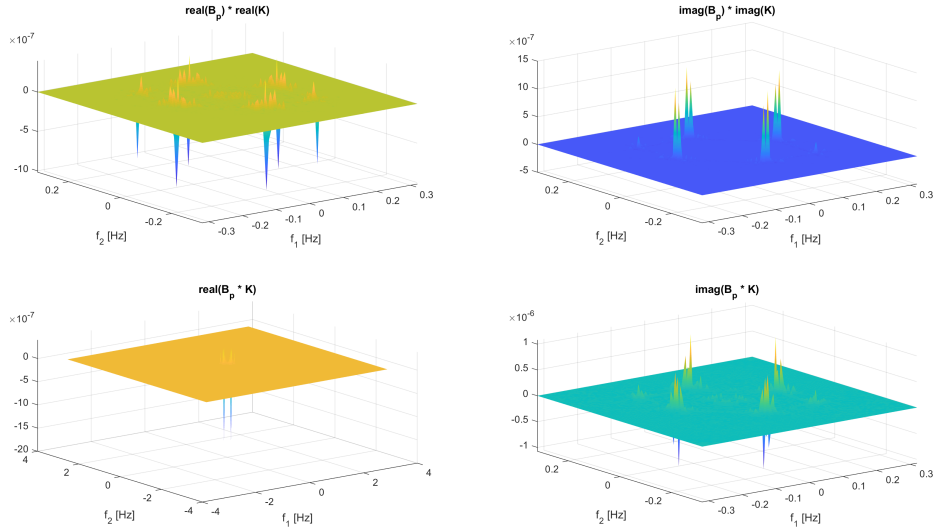

Figure C.7: Imaginary and real parts of Bq computed analytically, sample T315, 0° attack angle, mode 2, $f_2 = 0.15$ Hz.

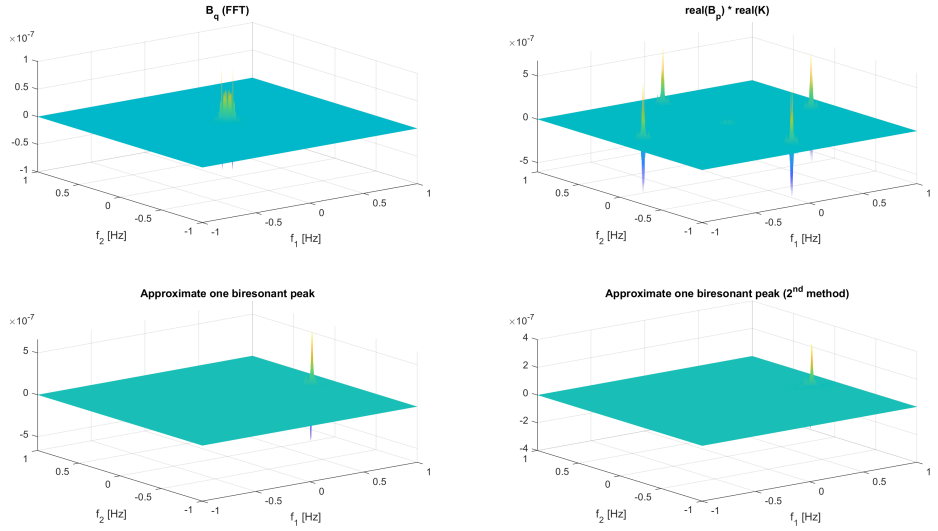

Figure C.8: Comparison of numerical approximations of Bispectrum of modal response with analytical one, sample T315, 0° attack angle, mode 2, $f_1 = 0.78$ Hz.

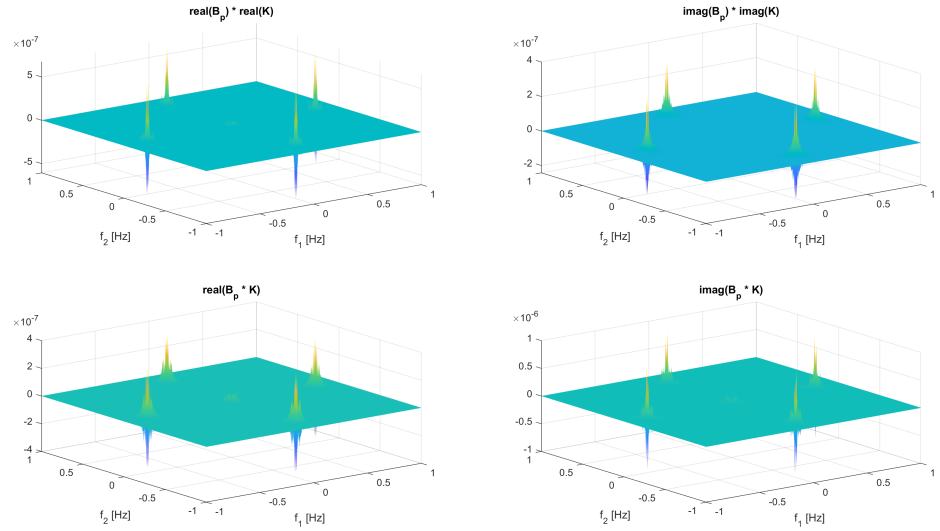

Figure C.9: Imaginary and real parts of Bq computed analytically, sample T315, 0° attack angle, mode 2, $f_2 = 0.78$ Hz.

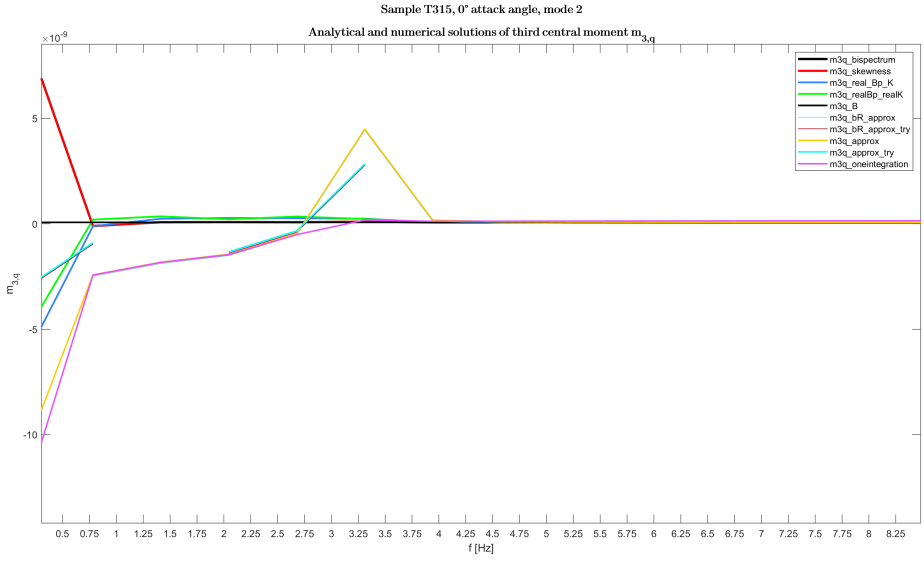

Figure C.10: Parametric analysis of $m_{3,q}$, mode 2, sample T315, 0° attack angle.

Bibliography

[1] Ray W. Penzien and Joshep Clough. *Dynamics of Structures*. Computers & Structures, Inc., 2003.

[2] Emil Simiu and DongHun Yeo. *Wind Effects on Structures: modern structural design for wind*. John Wiley & Sons, 2019.

[3] Vincent Denoël. *Analyse dynamique des structures du génie civil*, 2010.

[4] Patrick Paultre. *Dynamics of Structures*. ISTE Ltd, 2011.

[5] Dae Kun Kwon and Ahsan Kareem. *Peak Factors for Non-Gaussian Load Effects Revisited*. Review, University of Notre Dame, 2018.

[6] Denoël V. *On the background and biresonant components of the random response of single degree-of-freedom systems under non-Gaussian random loading*. Engineering Strutures (2011), doi:10.1016/j.engstruct.2011.04.003.

[7] Simon Lovens. *A response spectrum approach for the calculation of wind effects on structures*. Master Thesis, University of Bologna, 2018.

[8] Tokyo Polytechnic University, The School of Architecture & Wind Engineering, *http://wind.arch.t-kougei.ac.jp/system/eng/contents/code/tpu*.